DIMENSION REDUCTION OF THE GROSS-PITAEVSKII EQUATION FOR BOSE-EINSTEIN CONDENSATES

GE YUNYI

(B.Sc., Nanjing University, P.R.China)

A THESIS SUBMITTED

FOR THE DEGREE OF MASTER OF SCIENCE

DEPARTMENT OF COMPUTATIONAL SCIENCE

NATIONAL UNIVERSITY OF SINGAPORE

2004

Acknowledgments

I would like to thank my supervisor, Dr. Bao Weizhu, who gave me the opportunity to work on such an interesting research project, paid patient guidance to me about my work, encouraged me when I met trouble in my family, gave me invaluable advices on my thesis and help me review it. And I will also thanks my supervisor's wife for her passionate help with my family problem.

It is also my pleasure to express my appreciation and gratitude to A/P Chen kan and A/P Xu Xingwang, from whom I got effective training on programming, good ideas and experience, which helped me in my subsequent research work.

I would also wish to thank the National University of Singapore for her financial support by awarding me the Research Scholarship during the period of my MSc candidature.

My sincere thanks go to my department-mates and my friends who gave me suggestions or helps me during my research work. And special thanks go to Mr. Wang Hanquan, Ms. Zhang Yanzhi, Mr. Yuan Baosheng, Mr. Lu Yunpeng, Mr. Zhao Yibao, Ms. Sunjie for their patient help during my research.

I would also like to dedicate this work to my parents, who love me most in the world, for their unconditional love and support.

Ge Yunyi

Nov 2004

Contents

Summary

In the thesis, we study numerically and asymptotically dimension reduction of three-dimensional (3D) Gross-Pitaevskii equation (GPE) for Bose-Einstein condensates (BEC) in certain limiting trapping frequency regimes. As preparation steps, we take the 3D GPE, scale it to get a three parameters model, and review how to reduce it to 2D GPE in disk-shaped condensation or 1D GPE in cigar-shaped condensation. Then we compute the ground state of 3D GPE numerically by a normalized gradient flow under backward Euler finite difference discretization [9] and verify numerically the formal dimension reduction for ground state. From our numerical results, for relative errors of the interaction parameter, we observe numerically the convergence rate of 3/4 with respect to γ_z for dimension reduction from 3D to 2D, and respectively, of 1/3 with respect to γ_r for reduction from 3D to 1D, when the ratio between trapping frequencies goes to infinity. Furthermore, we obtain Thomas-Fermi and first order approximations for energy and chemical potential of the ground state for d-dimension GPE with $d = 1, 2, 3$.

Then we classify approximations of the ground state of 3D GPE in three cases based on the ratios between the trapping frequencies: i). isotropic condensation; ii). disk-shaped condensation; iii). cigar-shaped condensation. Approximate ground states as well as their energy and chemical potential are provided explicitly in weakly,

intermediate repulsive and strongly repulsive interaction regimes. These results are fully confirmed by our 3D numerical results. Also, convergence rates in relative error for all interacting quantities are observed and reported.

Finally, we study dimension reduction of time-dependent GPE from 3D to 2D numerically by a fourth-order time-splitting sine-spectral method [11]. Our numerical results confirm the formal dimension reduction for time-dependent GPE and also suggest convergence rates in limiting trapping frequency ratios.

Key words: Gross-Pitaevskii equation, Bose-Einstein condensate, Normalized gradient flow, Ground state solution, Backward Euler finite difference, Time-splitting sine-spectral method, Cylindrical symmetry, Radial symmetry, Dynamics, Dimension Reduction, Cigar-shaped condensation, Disk-shaped condensation.

List of Tables

List of Figures

Chapter 1

Introduction

The famous Bose-Einstein condensation (BEC), was theoretically predicted by Bose [20] and Einstein [33] in 1924, and was first observed in 1995 in a remarkable series of experiments on vapors of rubidium by Anderson [6] and of sodium by Davis [27]. In these two experimental realizations of BEC the atoms were confined in magnetic traps and cooled down to extremely low temperatures, of the order of fractions of microkelvins. The first evidence for condensation emerged from time-of-flight measurements. The atoms were left to expand by switching off the confining trap and then imaged with optical methods. A sharp peak in the velocity distribution was then observed below a certain critical temperature, providing a clear signature for BEC. In 1995, first signatures of the occurrence of BEC in vapors of lithium were also reported by Bradley [21].

Though the experiments of 1995 on the alkalis should be considered a milestone in the history of BEC, the experimental and theoretical research on this unique phenomenon predicted by quantum statistical mechanics is much older and has involved different areas of physics (for an interdisciplinary review of BEC see [37]). In particular, from the very beginning, superfluidity in helium was considered by London [45] as a possible manifestation of BEC. Evidence for BEC in helium later emerged from the analysis of the momentum distribution of the atoms measured in neutron-scattering experiments by Sokol [54]. In recent year, BEC has been also

investigated in the gas of paraexcitons in semiconductors (see [55] and references therein), but an unambiguous signature of BEC in this system has proven difficult to find.

In fact, besides internal interactions, the macroscopic behavior of BEC matter is highly sensitive to the shape of the external trapping potential. Theoretical predictions of the properties of a BEC like the density profile [19], collective excitations [32] and the formation of vortices [51] can now be compared with experimental data [6, 41, 47] by adjusting some tunable external parameters, such as the trap frequency and/or aspect ratio. Needless to say, this dramatics progress on the experimental front has stimulated a corresponding wave of activity on both the theoretical and the numerical fronts.

The properties of a BEC at temperatures T very much smaller than the critical temperature T_c [37, 42] are usually described by the nonlinear Schrödinger equation (NLSE) for the macroscopic wave function [37, 42] known as the Gross-Pitaevskii equation (GPE) [38, 48, 31, 19], which incorporates the trap potential as well as the interactions among the atoms. The results obtained by solving the GPE showed excellent agreement with most of the experiments. In fact, up to now there have been very few experiments in ultracold dilute bosonic gases, which could not be described properly by using theoretical methods based on the GPE.

The effect of the interactions is described by a mean field which leads to a nonlinear term in GPE. The cases of repulsive and attractive interactions - which can both be realized in the experiment - correspond to defocusing and focusing nonlinearities in the GPE, respectively. Note that equations very similar to the GPE also appear in nonlinear optics where an index of refraction which depends on the light intensity, leads to a nonlinear term like the one encountered in the GPE.

There has been a series of recent studies which deal with the numerical solution of the time-independent GPE for ground-state and the time-dependent GPE for finding the dynamics of a BEC. For numerical solution of time-dependent GPE, Bao et al. [8, 14] presented a time-splitting spectral method, Ruprecht et al. [52] and Adhikari

et al. [2, 3] used the Crank-Nicolson finite difference method to compute the ground-state solution and dynamics of GPE, Cerimele et al. [22] proposed a particle-inspired scheme. For ground-state solution of GPE, Edwards et al. [31] presented a Runge-Kutta type method and used it to solve 1D and 3D with spherical symmetry time-independent GPE, Adhikari [4, 5] used this approach to get the ground-state solution of GPE in 2D with radial symmetry, Bao el al. [7] presented a general method to compute the ground state solution via directly minimizing the energy functional. Other approaches include an explicit imaginary-time algorithm used by Cerimele et al. [23] and Chiofalo et al. [24], a direct inversion in the iterated subspace (DIIS) used by Schneider et al [53], and a simple analytical type method proposed by Dodd [28].

In many experiments for BEC, the trapping frequencies in different directions are far distinct. Experimentally, either a disk-shaped condensate or a cigar-shaped condensate is observed. In these cases, physicists suggest the original 3D GPE can be reducd to either a 2D GPE or 1D GPE since the energy in some directions are much larger than other directions and the wave function is not easy excited in the directions with larger energy. Therefore, to understand BEC in these cases, we need only to solve either a 2D GPE or a 1D GPE instead of the original 3D GPE. Thus the computational time and memory can be saved significantly. To our knowledge, the formal dimension reduction for 3D GPE is only based on physical intuition. There is no mathematical or numerical justification yet. Of course, this kind of rigorous justification is very important for the formal dimension reduction of 3D GPE. In this thesis, we will study numerically and asymptotically the dimension reduction of 3D GPE for BEC in certain limiting trapping frequencies regimes. Convergence rates for interesting quantities are observed and reported when the ratio between trapping frequencies goes to infinity. Based on these study, we provide approximate ground state, and their energy and chemical potential for 3D GPE in all kinds of different parameter regimes.

The thesis is organized as follows. In Chapter 2, we take the 3D GPE, scale it to get a three parameters model. Then we review the definition of the ground state for 3D GPE and the backward Euler finite difference (BEFD) method to compute ground state.

In Chapter 3, first we show how to reduce 3D GPE to 2D GPE in disk-shaped condensation or 1D GPE in cigar-shaped condensation. Then we compute the ground state of 3D GPE numerically by a normalized gradient flow under backward Euler finite difference discretization [9] and verify numerically the formal dimension reduction for ground state. From our numerical results, for relative errors of the interaction parameter, we observe numerically the convergence rate of 3/4 with respect to γ_z for dimension reduction from 3D to 2D, and respectively, of 1/3 with respect to γ_r for reduction from 3D to 1D, when the ratio between trapping frequencies goes to infinity. Furthermore, we obtain Thomas-Fermi and first order approximations for energy and chemical potential of the ground state for d-dimension GPE with $d = 1, 2, 3$.

In Chapter 4, we classify approximations of the ground state of 3D GPE in three cases based on the ratios between the trapping frequencies: i). isotropic condensation; ii). disk-shaped condensation; iii). cigar-shaped condensation. Approximate ground states as well as their energy and chemical potential are provided explicitly in weakly and strongly repulsive interaction regimes. These results are fully confirmed by our 3D numerical results. Also, convergence rates in relative error for all interacting quantities are observed and reported.

In Chapter 5, we study dimension reduction of time-dependent GPE from 3D to 2D numerically by a four-order time-splitting sine-spectral method [11]. Our numerical results confirm the formal dimension reduction for time-dependent GPE and also suggest convergence rates in limiting trapping frequency ratios.

Finally, some conclusions based on our findings and numerical results are given in Chapter 6.

Chapter 2

The Gross-Pitaevskii Equation

At temperatures T much smaller than the critical temperature T_c [42], the BEC is well described by the macroscopic wave function $\psi = \psi(\mathbf{x}, t)$ whose evolution is governed by a self-consistent, mean field nonlinear Schrödinger equation (NLSE) known as the Gross-Pitaevskii equation [38, 48, 49]. If a harmonic trap potential is considered, the single particle equation becomes:

$$i\hbar\frac{\partial\psi(\mathbf{x},t)}{\partial t} = -\frac{\hbar^2}{2m}\Delta\psi + V(\mathbf{x})\psi + NU_0|\psi|^2\psi, \quad \mathbf{x}\in\mathbb{R}^3, \tag{2.1}$$

where t is time, $\mathbf{x} = (x, y, z)^T$ is the spatial coordinate vector, m is the atomic mass, $\hbar$ is the Plank constant, N is the number of atoms in the condensate. $V(\mathbf{x})$ is a real-valued external trapping potential whose shape is determined by the type of system under investigation. When a harmonic trap potential is considered, $V(\mathbf{x}) = \frac{m}{2}(\omega_x^2x^2 + \omega_y y^2 + \omega_z z^2)$ with ω_x, ω_y, ω_z the trap frequencies in x, y and z-direction, respectively. U_0 describes the interaction between atoms in the condensate and has the form $U_0 = \frac{4\pi\hbar^2 a}{m}$ with a the s-wave scattering length (positive for repulsive interaction and negative for attractive interaction).

It is convenient to normalize the wave function by requiring

$$\int_{\mathbb{R}^3} |\psi(\mathbf{x},t)|^2 d\mathbf{x} = 1. \tag{2.2}$$

2.1 Nondimensionalization

Following the physics literatures [23, 7, 8, 49], in order to rescale the equation (2.1) under the normalization (2.2), we introduce:

$$\tilde{t} = \frac{t}{t_s}, \quad \tilde{\mathbf{x}} = \frac{\mathbf{x}}{a_0}, \quad \tilde{\psi}(\tilde{\mathbf{x}}, \tilde{t}) = a_0^{3/2}\psi(\mathbf{x}, t), \tag{2.3}$$

where the dimensionless length and time units are chosen as:

$$a_0 = \sqrt{\frac{\hbar}{m\omega_x}}, \quad t_s = \frac{1}{\omega_x}. \tag{2.4}$$

Here a_0 is the length of harmonic oscillator ground state in x-direction. Plugging (2.3) into (2.1), multiplying by $\frac{1}{m\omega_x^2 a_0^{1/2}}$ and then removing all $\sim$, we get the following dimensionless Gross-Pitaevskii equation under the normalization (2.2) in 3D:

$$i\frac{\partial\psi(\mathbf{x}, t)}{\partial t} = -\frac{1}{2}\triangle\psi(\mathbf{x}, t) + V(\mathbf{x})\psi(\mathbf{x}, t) + \beta|\psi(\mathbf{x}, t)|^2\psi(\mathbf{x}, t), \quad \mathbf{x} \in \mathbb{R}^3, \tag{2.5}$$

where $V(\mathbf{x}) = \frac{1}{2}(x^2 + \gamma_y^2 y^2 + \gamma_z^2 z^2)$, $\gamma_y = \frac{\omega_y}{\omega_x}$, $\gamma_z = \frac{\omega_z}{\omega_x}$ and $\beta = \frac{4\pi a N}{a_0}$.

Here positive/negative β corresponds to the defocusing/focusing NLSE, respectively.

There are two conservation laws of the GPE (2.5). They are the normalization of the wave function

$$\begin{aligned} N(\psi(\cdot, t)) &= \|\psi(\cdot, t)\|^2 = \int_{\mathbb{R}^3} |\psi(\mathbf{x}, t)|^2 d\mathbf{x} \\ &\equiv \int_{\mathbb{R}^3} |\psi(\mathbf{x}, 0)|^2 d\mathbf{x} = N(\psi(\cdot, 0)), \quad t \geq 0 \end{aligned} \tag{2.6}$$

and the energy

$$\begin{aligned} E(\psi(\cdot, t)) &= \int_{\mathbb{R}^3} \left[\frac{1}{2}|\nabla\psi(\mathbf{x}, t)|^2 + V(\mathbf{x})|\psi(\mathbf{x}, t)|^2 + \frac{\beta}{2}|\psi(\mathbf{x}, t)|^4\right] d\mathbf{x} \\ &\equiv E(\psi(\cdot, 0)), \quad t \geq 0. \end{aligned} \tag{2.7}$$

2.2 Ground state

To find a stationary solution of (2.5), we write:

$$\psi(\mathbf{x}, t) = e^{-i\mu t}\phi(\mathbf{x}), \tag{2.8}$$

where μ is the chemical potential of the condensate and ϕ is a real function independent of time. Inserting (2.8) into (2.5) and (2.2) gives the following equation for $\phi(\mathbf{x})$:

$$\mu\phi(\mathbf{x}) = -\frac{1}{2}\triangle\phi(\mathbf{x}) + V(\mathbf{x})\phi(\mathbf{x}) + \beta|\phi(\mathbf{x})|^2\phi(\mathbf{x}), \qquad \mathbf{x} \in \mathbb{R}^3 \tag{2.9}$$

under the normalization condition:

$$N(\phi) \triangleq \|\phi\|^2 = \int_{\mathbb{R}^3} |\phi(\mathbf{x})|^2 d\mathbf{x} = 1. \tag{2.10}$$

This is a nonlinear eigenvalue problem under a constraint and any eigenvalue μ can be computed from its corresponding eigenfunction ϕ by:

$$\begin{aligned} \mu = \mu(\phi) &= \int_{\mathbb{R}^3} \left[\frac{1}{2}|\nabla\phi(\mathbf{x})|^2 + V(\mathbf{x})|\phi(\mathbf{x})|^2 + \beta|\phi(\mathbf{x})|^4\right] d\mathbf{x} \\ &= E(\phi) + E_{\text{int}}(\phi), \end{aligned} \tag{2.11}$$

where $E_{\text{int}}(\phi)$ denotes the two-body interaction energy:

$$E_{\text{int}}(\phi) = \int_{\mathbb{R}^3} \frac{\beta}{2}|\phi(\mathbf{x})|^4 d\mathbf{x}. \tag{2.12}$$

In fact, the eigenfunctions of (2.9) under the constraint (2.10) are equivalent to the critical points of the energy functional $E(\phi)$ over the unit sphere

$$S = \left\{\phi |\ \|\phi\|^2 = 1, \quad E(\phi) < \infty\right\}.$$

Furthermore, as noted in [9], the solutions of (2.9) are equivalent to the steady state solutions of the following continuous normalized gradient flow (CNGF):

$$\frac{\partial\phi}{\partial t} = \frac{1}{2}\triangle\phi - V(\mathbf{x})\phi - \beta|\phi|^2\phi + \frac{\mu(\phi)}{\|\phi(\cdot,t)\|^2}\phi, \quad \mathbf{x} \in \mathbb{R}^3, \quad t \geq 0, \tag{2.13}$$

$$\phi(\mathbf{x},0) = \phi_0(\mathbf{x}), \quad \mathbf{x} \in \mathbb{R}^3 \quad \text{with} \quad \|\phi_0\| = 1. \tag{2.14}$$

The Bose-Einstein condensate ground state $\phi_g(\mathbf{x})$ is a real non-negative function (2.10) found by minimizing the energy $E(\phi)$ over the unit sphere S; i.e. find $(\mu_g, \phi_g \in S)$, s.t.

$$E(\phi_g) = \min_{\phi\in S} E(\phi), \quad \mu_g = \mu(\phi_g) = E(\phi_g) + E_{\text{int}}(\phi_g), \tag{2.15}$$

The existence of unique positive minimizer of the minimization problem (2.15) was given in [44].

Any eigenfunction $\phi(x)$ of (2.9) under constraint (2.10) whose energy $E(\phi) > E(\phi_g)$ is usually called as excited states in physics literatures.

2.3 Numerical methods for computing ground state

There are many numerical methods to compute the ground state in the literatures, e.g. imaginary time method [24] and normalized gradient flow [9]. Since the experiments setup are usually in a cylindrical symmetric trap, here we only review the normalized gradient flow with backward Euler finite difference (BEFD) discretization, proposed in [9], to compute ground state in 3D with a cylindrical trap, i.e. $\gamma_y = 1$ in (2.5).

The time step is given by $k = \triangle t > 0$ and we define time steps by $t_n \triangleq nk$, $n = 0, 1, 2, \cdots$

In this cylindrical symmetric case, the solution $\phi(\mathbf{x}, t) = \phi(r, z, t)$ and the original 3D problem collapses to a 2D problem with $r = \sqrt{x^2 + y^2} \in [0, \infty)$ and $-\infty < z < +\infty$ [9]:

$$\frac{\partial \phi(r,z,t)}{\partial t} = \frac{1}{2}\left[\frac{1}{r}\frac{\partial}{\partial r}(r\frac{\partial \phi}{\partial r}) + \frac{\partial^2 \phi}{\partial z^2}\right] - \frac{1}{2}(\gamma_r^2 r^2 + \gamma_z^2 z^2)\phi - \beta|\phi|^2\phi \ ,$$
$$0 < r < +\infty, \qquad -\infty < z < +\infty, \qquad t_n < t < t_{n+1} \ , \quad (2.16)$$

$$\frac{\partial \psi(0,z,t)}{\partial r} = 0, \quad \lim_{r\to+\infty} \phi(r,z,t) = 0, \quad \lim_{z\to\pm\infty} \phi(r,z,t) = 0, \quad t \geq 0, \quad (2.17)$$

$$\phi(r,z,t_{n+1}) \triangleq \frac{\phi(r,z,t_{n+1}^-)}{\|\phi(\cdot,t_{n+1}^-)\|}, \qquad n \geq 0, \quad (2.18)$$

$$\phi(r,z,0) = \phi_0(r,z) \geq 0 \ . \quad (2.19)$$

The normalization condition reads:

$$\|\phi\|^2 = 2\pi \int_0^\infty \int_{-\infty}^{+\infty} \phi^2(r,z,t) r dr dz. \quad (2.20)$$

We choose $R > 0$, $a < b$ and time step $k > 0$ with $|a|$, b, R sufficiently large. Denote the mesh size $h_r = (R-0)/M$ and $h_z = (b-a)/N$ with M and N two positive integers. Let grid points be $r_j = jh_r$, $j = 0, 1, \cdots, M$ and $r_{j-\frac{1}{2}} = (j-\frac{1}{2})h_r$, $j = 0, 1, \cdots, M$, $z_l = a + lh_z$, $l = 0, 1, \cdots, N$. Furthermore, Let $\phi^n_{j-\frac{1}{2},l}$ be the approximation of $\phi(r_{j-\frac{1}{2}}, z_l, t_n)$.

Thus we get the BEFD discretization for the 3D problem with cylindrical symmetry [9]:

$$
\begin{aligned}
\frac{\phi^*_{j-\frac{1}{2},l} - \phi^n_{j-\frac{1}{2},l}}{k} &= \frac{1}{2h_r^2 r_{j-\frac{1}{2}}}\left[r_j\phi^*_{j+\frac{1}{2},l} - (r_j + r_{j-1})\phi^*_{j-\frac{1}{2},l} + r_{j-1}\phi^*_{j-\frac{3}{2},l}\right] \\
&\quad + \frac{1}{2h_z^2}\left[\phi^*_{j-\frac{1}{2},l+1} - 2\phi^*_{j-\frac{1}{2},l} + \phi^*_{j-\frac{1}{2},l-1}\right] - \frac{1}{2}(\gamma_r^2 r^2_{j-\frac{1}{2}} + \gamma_z^2 z_l^2)\phi^*_{j-\frac{1}{2},l} \\
&\quad - \beta(\phi^n_{j-\frac{1}{2},l})^2\phi^*_{j-\frac{1}{2},l}\,, \qquad j = 1, \cdots, M-1, \quad l = 1, \cdots, N-1, \\
\phi^*_{-\frac{1}{2},l} &= \phi^*_{\frac{1}{2},l}, \quad \phi^*_{M-\frac{1}{2},l} = 0, \qquad l = 1, \cdots, N-1, \\
\phi^*_{j-\frac{1}{2},0} &= \phi^*_{j-\frac{1}{2},N} = 0, \qquad j = 0, 1 \cdots, M, \\
\phi^{n+1}_{j-\frac{1}{2},l} &= \frac{\phi^*_{j-\frac{1}{2},l}}{\|\phi^*\|}, \qquad j = 0, \cdots, M, \quad l = 0, \cdots, N, \quad n = 1, 2, \cdots, \\
\phi^0_{j-\frac{1}{2},l} &= \phi_0(r_{j-\frac{1}{2}}, z_l) \qquad j = 0, \cdots, M, \quad l = 0, \cdots, N, \\
\phi^0_{-\frac{1}{2},l} &= \phi^0_{\frac{1}{2},l}, \qquad l = 0, 1, \cdots, N,
\end{aligned}
\tag{2.21}
$$

where the norm is defined as

$$
\begin{aligned}
\|\phi^*\|^2 &= 2\pi h_r h_z \sum_{j=1}^{M} r_{j-\frac{1}{2}} \left\{ \sum_{l=1}^{N-1} (\phi^*_{j-\frac{1}{2},l})^2 + \frac{1}{2}(\phi^*_{j-\frac{1}{2},0})^2 + \frac{1}{2}(\phi^*_{j-\frac{1}{2},N})^2 \right\} \\
&= 2\pi h_r h_z \sum_{j=1}^{M} \sum_{l=1}^{N-1} (\phi^*_{j-\frac{1}{2},l})^2 r_{j-\frac{1}{2}}\,.
\end{aligned}
\tag{2.22}
$$

In the next chapter, we will use this algorithm to compute the ground state of 3D GPE and then verify dimension reduction of 3D GPE numerically.

Chapter 3

Dimension Reduction for 3D GPE

In this chapter, we will first review how to reduce 3D GPE to 2D or 1D GPE in certain limiting trapping frequency regime. Then we use numerical methods to verify this dimension reduction. Finally, we derive the Thomas-Fermi and first order approximation for energy and chemical potential of ground state for d-dimension GPE with $d = 1, 2, 3$ in strongly defocusing regime.

3.1 Reduction to 2D in a disk-shaped condensate

For a disk-shaped condensate, i.e.

$$\omega_x \approx \omega_y,\ \omega_z \gg \omega_x \quad \Longleftrightarrow \quad \gamma_y \approx 1,\ \gamma_z \gg 1, \tag{3.1}$$

the 3D GPE (2.5) can be reduced to a 2D GPE by assuming that the time evolution does not cause excitations along the z-axis since it has a large energy of approximately $\hbar\omega_z$ compared to excitations along the x and y-axis with energies of about $\hbar\omega_x$. Following the physics literatures [43, 30, 7, 8], for any fixed $\beta \geq 0$ and when $\gamma_z \gg 1$, we assume that the condensation wave function along the z-axis is always well described by the ground state wave function which is well approximated by the harmonic oscillator in z-direction and set [40, 30, 7, 8]:

$$\psi(x,y,z,t) = \psi_{12}(x,y,t)\phi_3(z), \tag{3.2}$$

$$\phi_3(z) = \left(\int_{\mathbb{R}^2} |\phi_g(x,y,z)|^2 dxdy\right)^{\frac{1}{2}} \approx \phi_3^{\rm ho}(z) = \left(\frac{\gamma_z}{\pi}\right)^{1/4} e^{-\gamma_z z^2/2}, \tag{3.3}$$

where $\phi_g(x,y,z)$ is the ground state of the 3D GPE (2.5).

Plugging (3.2) into (2.5), we get:

$$i\frac{\partial \psi_{12}}{\partial t}\phi_3 = -\frac{1}{2}\left(\frac{\partial^2 \psi_{12}}{\partial x^2} + \frac{\partial^2 \psi_{12}}{\partial y^2}\right)\phi_3 - \frac{1}{2}\psi_{12}\frac{d^2\phi_3}{dz^2} + V(\mathbf{x})\psi_{12}\phi_3 + \beta|\psi_{12}|^2\psi_{12}|\phi_3|^2\phi_3,$$

Multiplying both sides by the conjugate of ϕ_3, then integrating with respect to z over $(-\infty, +\infty)$, we obtain:

$$i\frac{\partial \psi_{12}}{\partial t} = -\frac{1}{2}\triangle\psi_{12} + \frac{1}{2}\left(x^2 + \gamma_y^2 y^2 + C\right)\psi_{12} + \left(\beta\int_{-\infty}^{+\infty} |\phi_3|^4 dz\right)|\psi_{12}|^2\psi_{12}\ , \tag{3.4}$$

where

$$C \ = \ \gamma_z^2 \int_{-\infty}^{+\infty} z^2 |\phi_3(z)|^2 dz + \int_{-\infty}^{+\infty} \left|\frac{d\phi_3}{dz}\right|^2 dz\ .$$

Because equation (3.4) is time-transverse invariant, we can replace $\psi_{12} \to \psi e^{-i\frac{Ct}{2}}$ which drops the constant C in the trap potential. Then we get the 2D GPE:

$$i\frac{\partial \psi}{\partial t} = -\frac{1}{2}\triangle\psi + \frac{1}{2}(x^2 + \gamma_y^2 y^2)\psi + \beta_2|\psi|^2\psi\ , \tag{3.5}$$

where

$$\beta_2 = \beta\int_{-\infty}^{+\infty} \phi_3^4(z)dz \approx \beta\int_{-\infty}^{+\infty} |\phi_3^{\rm ho}|^4 dz = \beta_2^{\rm ho} = \beta\sqrt{\frac{\gamma_z}{2\pi}}\ . \tag{3.6}$$

To verify (3.3) and (3.6) numerically, we compute the ground state of the 3D GPE by the continuous normalized gradient flow with BEFD discretization (2.21)-(2.22). Then we get $\phi_g(r,z)$, which is used to compute $\phi_3(z)$ by (3.3) and compute β_2 by (3.6).

The computational domain is chosen as $(r,z) \in [0,R] \times [-a,a]$ for the algorithm (2.21)-(2.22). The choice of R and a for different β and γ_z is listed in Table 3.1.

Table 3.1: The choice of (R, a) in the algorithm (2.21)-(2.22) for different β and γ_z.

γ_z	25	100	400	1600
$\beta = 1$	$(7, 1.6)$	$(7, 0.8)$	$(8, 0.4)$	$(8, 0.2)$
$\beta = 10$	$(8, 1.6)$	$(8, 0.8)$	$(8, 0.4)$	$(8, 0.2)$
$\beta = 100$	$(7.8, 1.4)$	$(8.8, 0.7)$	$(9.8, 0.35)$	$(10.6, 0.17)$
$\beta = 1000$	$(10.8, 1.4)$	$(12, 0.7)$	$(13.5, 0.35)$	$(15, 0.17)$
$\beta = 10000$	$(15, 1.6)$	$(18, 0.8)$	$(21, 0.4)$	$(25, 0.2)$

Table 3.2 lists the error $|\beta_2^{\text{ho}} - \beta_2|$, Table 3.3 lists the error $\frac{|\beta_2^{\text{ho}} - \beta_2|}{\beta_2}$, Table 3.4 lists the error $\max|(\phi_3)^2 - (\phi_3^{\text{ho}})^2|$, Table 3.5 lists the error $||(\phi_3)^2 - (\phi_3^{\text{ho}})^2||_{L^1}$ and Table 3.6 lists the error $\|\phi_3 - \phi_3^{\text{ho}}\|_{L^2}$ for different β and γ_z.

Furthermore, Figure 3.1 shows the error $|\beta_2^{\text{ho}} - \beta_2|$, Figure 3.2 shows the error $\frac{|\beta_2^{\text{ho}} - \beta_2|}{\beta_2}$, Figure 3.3 shows the error $\max|(\phi_3)^2 - (\phi_3^{\text{ho}})^2|$, Figure 3.4 shows the error $||(\phi_3)^2 - (\phi_3^{\text{ho}})^2||_{L^1}$ and Figure 3.5 shows the error $\|\phi_3 - \phi_3^{\text{ho}}\|_{L^2}$ for different β and γ_z.

Table 3.2: Error analysis of $|\beta_2^{\text{ho}} - \beta_2|$ for dimension reduction from 3D to 2D.

$1/\gamma_z$	1/25	1/100	1/400	1/1600
$\beta = 1$	0.59499e-02	0.52553e-02	0.43266e-02	0.32628e-02
rate		0.09	0.14	0.20
$\beta = 10$	0.31876	0.24116	0.17620	0.12545
rate		0.20	0.23	0.25
$\beta = 100$	0.10897e+02	0.80575e+01	0.57919e+01	0.41134e+01
rate		0.22	0.24	0.25
$\beta = 1000$	0.30959e+03	0.24654e+03	0.18164e+03	0.13020e+03
rate		0.16	0.22	0.24
$\beta = 10000$	0.68895e+04	0.67926e+04	0.54789e+04	0.40470e+04
rate		0.01	0.16	0.22

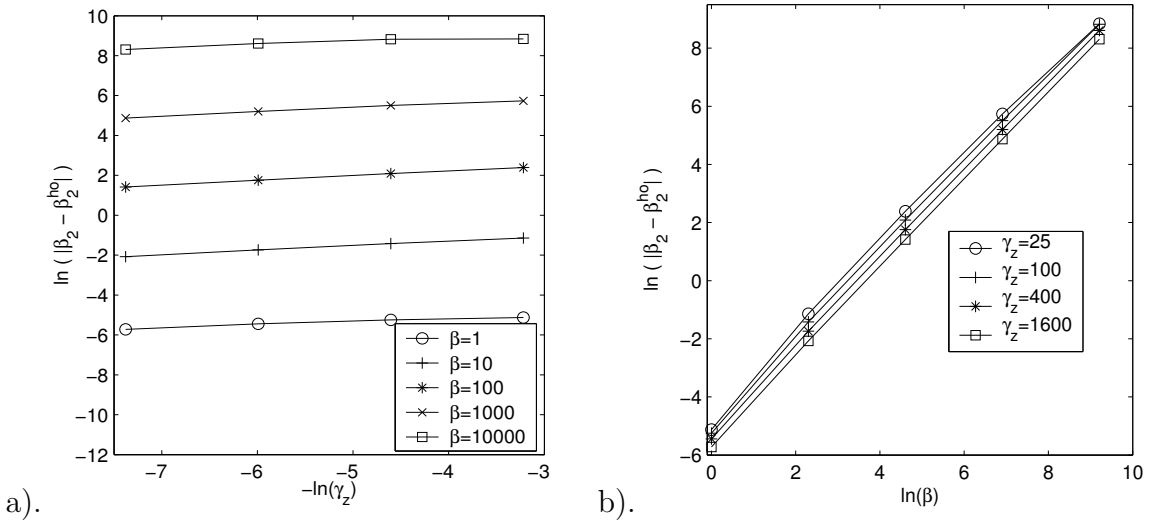

a). b).

Figure 3.1: Convergence rate of $|\beta_2^{\text{ho}} - \beta_2|$ with respect to: (a) γ_z; (b) β.

Table 3.3: Error analysis of $\frac{|\beta_2^{\rm ho}-\beta_2|}{\beta_2}$ for dimension reduction from 3D to 2D.

$1/\gamma_z$	1/25	1/100	1/400	1/1600
$\beta = 1$	0.29918e-02	0.13190e-02	0.54255e-03	0.20451e-03
rate		0.59	0.64	0.70
$\beta = 10$	0.16240e-01	0.60817e-02	0.22133e-02	0.78676e-03
rate		0.71	0.73	0.75
$\beta = 100$	0.57785e-01	0.20613e-01	0.73122e-02	0.25843e-02
rate		0.74	0.75	0.75
$\beta = 1000$	0.18372	0.65869e-01	0.23295e-01	0.82260e-02
rate		0.74	0.75	0.75
$\beta = 10000$	0.52762	0.20520	0.73731e-01	0.26021e-01
rate		0.68	0.74	0.75

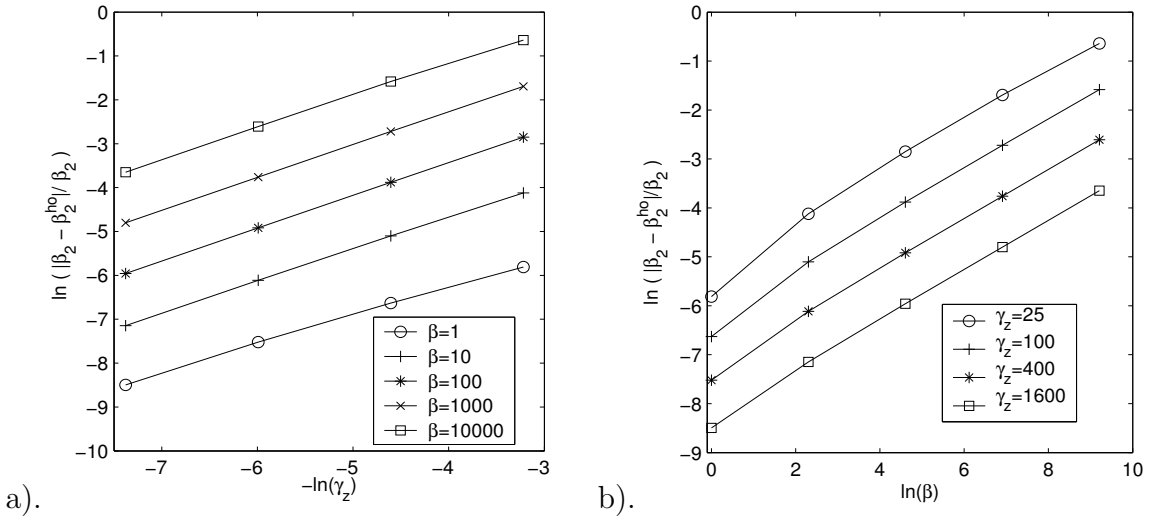

Figure 3.2: Convergence rate of $\frac{|\beta_2^{\rm ho}-\beta_2|}{\beta_2}$ with respect to: (a) γ_z; (b) β.

Table 3.4: Error analysis of $\max|(\phi_3)^2 - (\phi_3^{\rm ho})^2|$ for dimension reduction from 3D to 2D.

$1/\gamma_z$	1/25	1/100	1/400	1/1600
$\beta = 1$	2.8612e-03	1.7872e-03	1.0409e-03	5.7183e-04
rate		0.34	0.39	0.43
$\beta = 10$	1.5352e-02	8.2049e-03	4.2377e-03	2.1350e-03
rate		0.45	0.48	0.49
$\beta = 100$	5.2868e-02	2.7489e-02	1.3941e-02	6.9970e-03
rate		0.47	0.49	0.50
$\beta = 1000$	0.15315	8.4788e-02	4.3850e-02	2.2165e-02
rate		0.43	0.48	0.49
$\beta = 10000$	1.0622	1.0758	0.13343	6.9129e-02
rate		-0.01	1.5	0.47

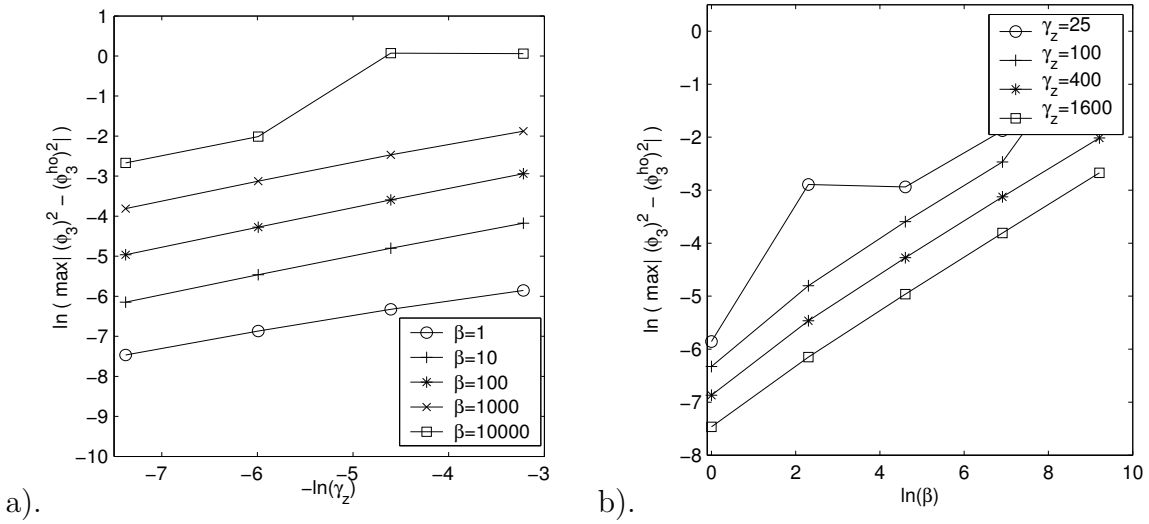

a). b).

Figure 3.3: Convergence rate of $\max|(\phi_3)^2 - (\phi_3^{\rm ho})^2|$ with respect to: (a) γ_z; (b) β.

Table 3.5: Error analysis of $||(\phi_3)^2 - (\phi_3^{\rm ho})^2||_{L^1}$ for dimension reduction from 3D to 2D.

$1/\gamma_z$	1/25	1/100	1/400	1/1600
$\beta = 1$	3.0181e-03	1.3317e-03	5.4797e-04	2.0752e-04
rate		0.59	0.64	0.70
$\beta = 10$	1.6287e-02	6.1274e-03	2.2337e-03	7.9524e-04
rate		0.71	0.73	0.75
$\beta = 100$	5.6975e-02	2.0643e-02	7.3640e-03	2.6087e-03
rate		0.73	0.74	0.75
$\beta = 1000$	0.17205	6.4757e-02	2.3305e-02	8.2826e-03
rate		0.70	0.74	0.75
$\beta = 10000$	0.43027	0.19054	7.2256e-02	2.6000e-02
rate		0.59	0.70	0.74

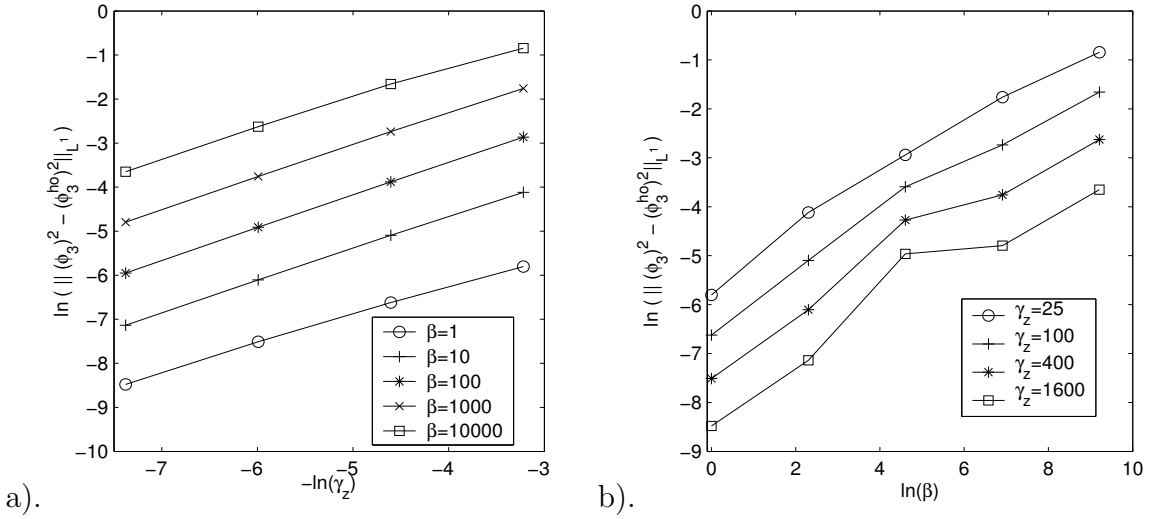

Figure 3.4: Convergence rate of $||(\phi_3)^2 - (\phi_3^{\rm ho})^2||_{L^1}$ with respect to: (a) γ_z; (b) β.

Table 3.6: Error analysis of $\|\phi_3 - \phi_3^{\rm ho}\|_{L^2}$ for dimension reduction from 3D to 2D.

$1/\gamma_z$	1/25	1/100	1/400	1/1600
$\beta = 1$	1.9542e-03	8.6198e-04	3.5470e-04	1.3464e-04
rate		0.59	0.64	0.70
$\beta = 10$	1.0565e-02	3.9683e-03	1.4459e-03	5.1497e-04
rate		0.71	0.73	0.74
$\beta = 100$	3.7093e-02	1.3387e-02	4.7689e-03	1.6891e-03
rate		0.74	0.75	0.75
$\beta = 1000$	0.11322	4.2161e-02	1.5115e-02	5.3644e-03
rate		0.71	0.74	0.75
$\beta = 10000$	0.29025	0.12557	4.7072e-02	1.6868e-02
rate		0.60	0.71	0.74

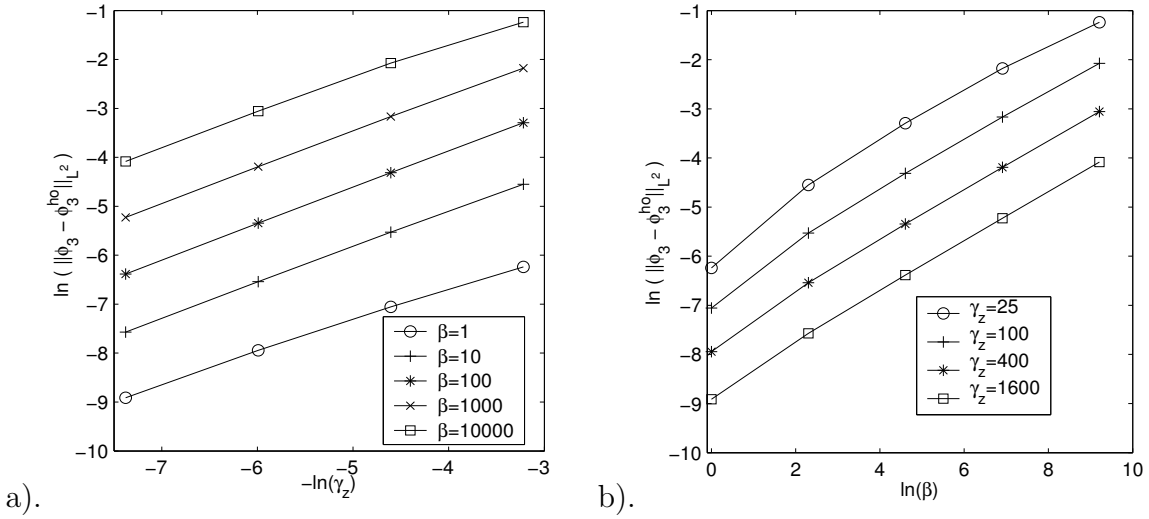

Figure 3.5: Convergence rate of $\|\phi_3 - \phi_3^{\rm ho}\|_{L^2}$ with respect to: (a) γ_z; (b) β.

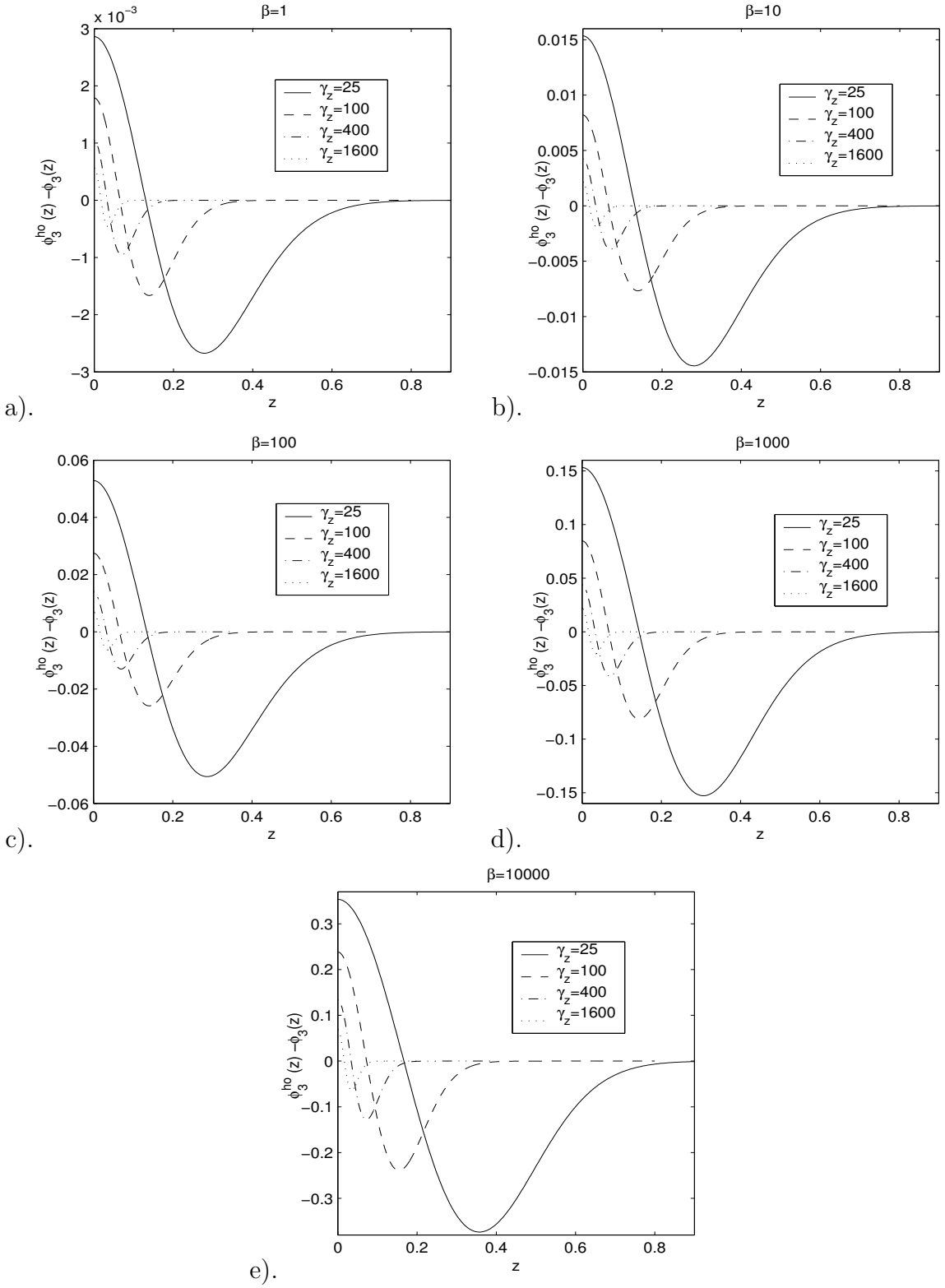

Figure 3.6: Error $\phi_3^{\mathrm{ho}}(z) - \phi_3(z)$ as function of z for different β and γ_z.

From Tables 3.2-3.6 and Figures 3.1-3.5, when $\beta \geq 0$, $\gamma_z \gg 1$ and $\beta\gamma_z^{-3/2} = o(1)$, we can draw the following conclusions:

$$\beta_2 = \beta\sqrt{\frac{\gamma_z}{2\pi}}\left(1 + O\left(\frac{\beta^{1/2}\ \ln\gamma_z}{\gamma_z^{3/4}}\right)\right), \qquad \frac{|\beta_2 - \beta_2^{\rm ho}|}{\beta_2} = O\left(\frac{\beta^{1/2}\ \ln\gamma_z}{\gamma_z^{3/4}}\right),$$

$$\|\phi_3(z) - \phi_3^{\rm ho}(z)\|_{L^2} = O\left(\frac{\beta^{1/2}\ \ln\gamma_z}{\gamma_z^{3/4}}\right),$$

$$\|(\phi_3(z))^2 - (\phi_3^{\rm ho}(z))^2\|_{L^\infty} = O\left(\frac{\beta^{1/2}\ \ln\gamma_z}{\gamma_z^{1/2}}\right),$$

$$\|(\phi_3(z))^2 - (\phi_3^{\rm ho}(z))^2\|_{L^1} = O\left(\frac{\beta^{1/2}\ln\gamma_z}{\gamma_z^{3/4}}\right).$$

Furthermore, from Figure 3.6, we can see that for fixed β, $\phi_3(z)$ converges to $\phi_3^{\rm ho}(z)$ pointwisely when $\gamma_z \to +\infty$.

3.2 Reduction to 1D in a cigar-shaped condensate

For a cigar-shaped condensate, i.e.

$$\omega_y \gg \omega_x,\ \omega_z \gg \omega_x \quad \Longleftrightarrow \quad \gamma_y \gg 1,\ \gamma_z \gg 1\ , \tag{3.7}$$

the 3D GPE (2.5) can be reduced to 1D GPE analogously. For any fixed $\beta \geq 0$ and when $\gamma_y \to \infty$ and $\gamma_z \to \infty$, we set:

$$\psi(x, y, z, t) = \psi_1(x, t)\phi_{23}(y, z)\ , \tag{3.8}$$

and

$$\begin{aligned}\phi_{23}(y, z) &= \left(\int_{\mathbb{R}} |\phi_g(x, y, z)|^2 dx\right)^{1/2} \\ &\approx \phi_{23}^{\rm ho}(y, z) = \left(\frac{\gamma_y\gamma_z}{\pi^2}\right)^{1/4} e^{-(\gamma_y y^2 + \gamma_z z^2)/2},\end{aligned} \tag{3.9}$$

where $\phi_g(x, y, z)$ is the ground state of the 3D GPE (2.5).

Plugging (3.8) into (2.5), we get:

$$i\frac{\partial\psi_1}{\partial t}\phi_{23} = -\frac{1}{2}\frac{\partial^2\psi_1}{\partial x^2}\phi_{23} - \frac{1}{2}\psi_1\triangle\phi_{23} + V(\mathbf{x})\psi_1\phi_{23} + \beta|\psi_1|^2\psi_1|\phi_{23}|^2\phi_{23}\ .$$

Multiplying both sides by the conjugate of $\phi_{23}(y,z)$, then integrating both sides in yz-plane over $\mathbb{R}^2$, we obtain:

$$i\frac{\partial\psi_1}{\partial t} = -\frac{1}{2}\frac{\partial^2\psi_1}{\partial x^2} + \frac{1}{2}\left(x^2+C\right)\psi_1 + \left(\beta\int_{-\infty}^{+\infty}|\phi_{23}|^4 dydz\right)|\psi_1|^2\psi_1 \ , \qquad (3.10)$$

where

$$C = \int_{-\infty}^{+\infty}|\nabla\phi_{23}|^2 dydz + \int_{-\infty}^{+\infty}(\gamma_y^2y^2+\gamma_z^2z^2)|\phi_{23}|^2 dydz \ .$$

Since equation (3.10) is time-transverse invariant, we can replace $\psi_1 \longrightarrow \psi e^{-i\frac{Ct}{2}}$ which drops the constant C in the trap potential. Then we get the 1D GPE:

$$i\frac{\partial\psi}{\partial t} = -\frac{1}{2}\psi_{xx} + \frac{x^2}{2}\psi + \beta_1|\psi|^2\psi \ , \qquad (3.11)$$

where

$$\beta_1 = \beta\int_{\mathbb{R}^2}\phi_{23}^4(y,z)dydz \approx \beta\int_{\mathbb{R}^2}|\phi_{23}^{\rm ho}|^4 dydz = \beta_1^{\rm ho} = \beta\frac{\sqrt{\gamma_y\gamma_z}}{2\pi} \ . \qquad (3.12)$$

To verify (3.9) and (3.12) numerically with $\gamma_r \triangleq \gamma_y = \gamma_z$, we compute the ground state of the 3D GPE by the continuous normalized gradient flow with BEFD discretization for (2.5). Then we get $\phi_g(r,z)$, which is used to compute $\phi_{23}(z)$ by (3.9) and compute β_1 by (3.12).

The computational domain is chosen as $(r,x) \in [0,R]\times[-a,a]$ for the algorithm (2.21)-(2.22). The choice of R and a for different β and γ_r is listed in Table 3.7.

Table 3.8 lists the error $|\beta_1-\beta_1^{\rm ho}|$, Table 3.9 lists the error $\frac{|\beta_1-\beta_1^{\rm ho}|}{\beta_1}$, Table 3.10 lists the error $\max|\phi_{23}-\phi_{23}^{\rm ho}|$, Table 3.11 lists the error $\frac{\max|\phi_{23}-\phi_{23}^{\rm ho}|}{\max|\phi_{23}|}$, Table 3.12 lists the error $||(\phi_{23})^2-(\phi_{23}^{\rm ho})^2||_{L^1}$ and Table 3.13 lists the error $\frac{||(\phi_{23})^2-(\phi_{23}^{\rm ho})^2||_{L^1}}{||(\phi_{23})^2||_{L^1}}$ for different β and γ_r.

Furthermore, Figure 3.7 shows the error $|\beta_1-\beta_1^{\rm ho}|$, Figure 3.8 shows the error $\frac{|\beta_1-\beta_1^{\rm ho}|}{\beta_1}$, Figure 3.9 shows the error $\max|\phi_{23}-\phi_{23}^{\rm ho}|$, Figure 3.10 shows the error $\frac{\max|\phi_{23}-\phi_{23}^{\rm ho}|}{\max|\phi_{23}|}$, Figure 3.11 shows the error $||(\phi_{23})^2-(\phi_{23}^{\rm ho})^2||_{L^1}$ and Figure 3.12 shows the error $\frac{||(\phi_{23})^2-(\phi_{23}^{\rm ho})^2||_{L^1}}{||(\phi_{23})^2||_{L^1}}$ for different β and γ_r.

Table 3.7: The choice of (R, a) in the algorithm (2.21)-(2.22) for different β and γ_r.

γ_r	12.5	25	50	100	200
$\beta = 25$	$(2.0, 8.5)$	$(1.4, 9.5)$	$(1.0, 10.5)$	$(0.7, 12.0)$	$(0.5, 14.0)$
$\beta = 50$	$(2.0, 9.0)$	$(1.4, 10.5)$	$(1.0, 12.0)$	$(0.7, 14.0)$	$(0.5, 16.5)$
$\beta = 100$	$(2.0, 10.0)$	$(1.4, 11.5)$	$(1.0, 13.5)$	$(0.7, 16.0)$	$(0.5, 19.0)$
$\beta = 200$	$(2.0, 11.0)$	$(1.4, 13.0)$	$(1.0, 15.5)$	$(0.7, 18.5)$	$(0.5, 23.0)$
$\beta = 400$	$(2.0, 12.0)$	$(1.5, 14.5)$	$(1.0, 17.5)$	$(0.7, 21.5)$	$(0.48, 27.0)$

Table 3.8: Error analysis of $|\beta_1 - \beta_1^{\rm ho}|$ for dimension reduction from 3D to 1D.

γ_r	12.5	25	50	100	200
$\beta = 25$	11.62	19.66	32.85	54.40	89.37
rate		0.76	0.74	0.73	0.72
$\beta = 50$	31.86	54.97	93.66	157.8	263.3
rate		0.79	0.77	0.75	0.74
$\beta = 100$	83.00	146.7	255.8	440.5	749.8
rate		0.86	0.84	0.82	0.80
$\beta = 200$	205.4	371.9	665.0	1174	2047
rate		0.86	0.84	0.82	0.80
$\beta = 400$	484.8	897.7	1644	2976	5321
rate		0.89	0.87	0.86	0.84

a).

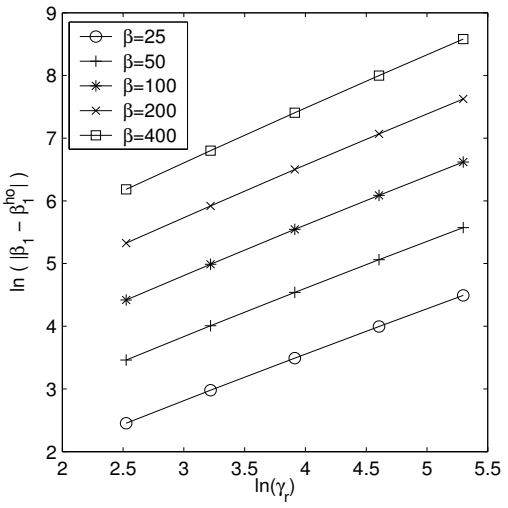

b).

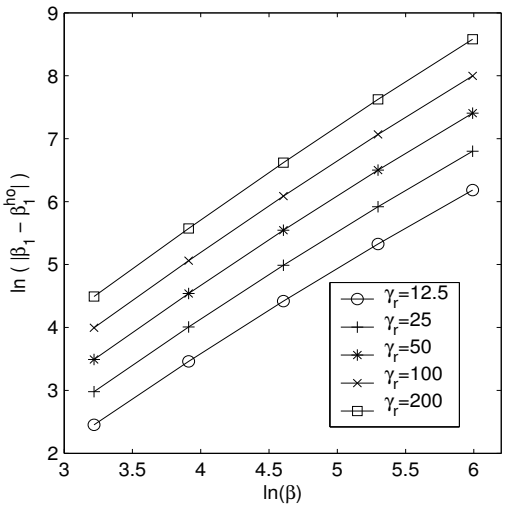

Figure 3.7: Convergence rate of $|\beta_1 - \beta_1^{\rm ho}|$ with respect to: (a) γ_r; (b) β.

Table 3.9: Error analysis of $\frac{|\beta_1-\beta_1^{\rm ho}|}{\beta_1}$ for dimension deduction from 3D to 1D.

$\frac{1}{\gamma_r}$	1/12.5	1/25	1/50	1/100	1/200
$\beta = 25$	0.3048	0.2463	0.1978	0.1584	0.1265
rate		0.31	0.32	0.32	0.32
$\beta = 50$	0.4712	0.3818	0.3078	0.2474	0.1982
rate		0.30	0.31	0.32	0.32
$\beta = 100$	0.7158	0.5838	0.4736	0.3827	0.3082
rate		0.29	0.30	0.31	0.31
$\beta = 200$	1.067	0.8773	0.7177	0.5844	0.4738
rate		0.28	0.29	0.30	0.30
$\beta = 400$	1.559	1.294	1.068	0.8778	0.7179
rate		0.27	0.28	0.29	0.29

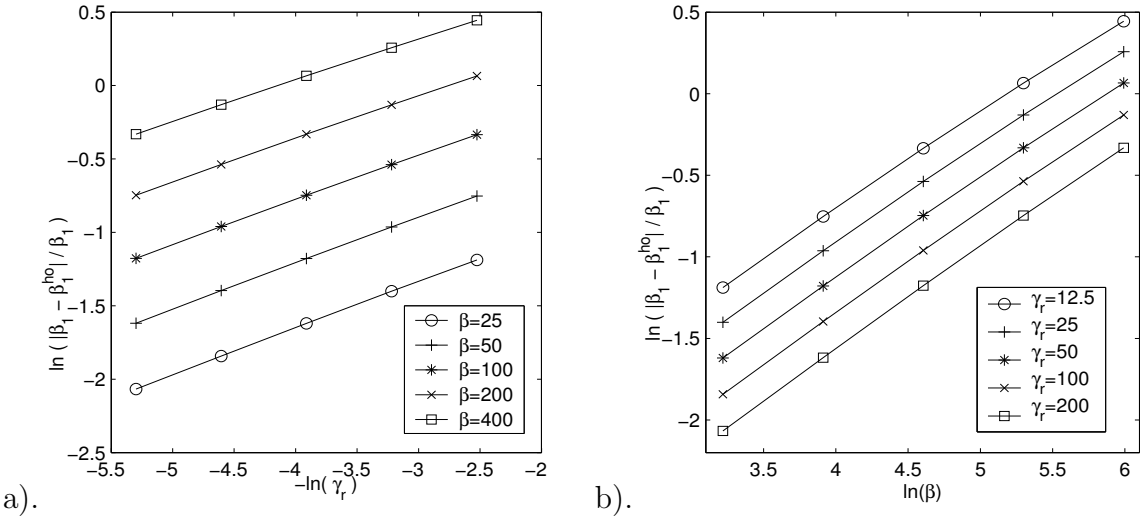

Figure 3.8: Convergence rate of $\frac{|\beta_1-\beta_1^{\rm ho}|}{\beta_1}$ with respect to: (a) γ_r; (b) β.

Table 3.10: Error analysis of $\max|\phi_{23} - \phi_{23}^{\mathrm{ho}}|$ for dimension deduction from 3D to 1D.

γ_r	12.5	25	50	100	200
$\beta = 25$	0.2937	0.3490	0.4098	0.4772	0.5517
rate		0.25	0.23	0.22	0.21
$\beta = 50$	0.4105	0.4963	0.5928	0.7010	0.8214
rate		0.27	0.26	0.24	0.23
$\beta = 100$	0.5469	0.6759	0.8248	0.9949	1.187
rate		0.31	0.29	0.27	0.25
$\beta = 200$	0.6938	0.8776	1.096	1.353	1.651
rate		0.34	0.32	0.30	0.29
$\beta = 400$	0.8406	1.087	1.389	1.756	2.194
rate		0.37	0.35	0.34	0.32

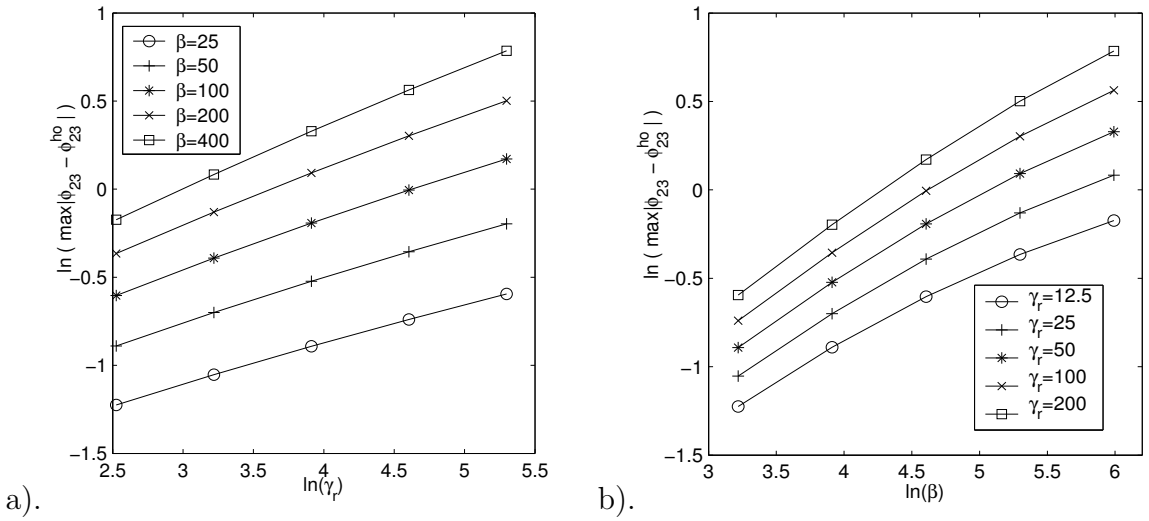

a). b).

Figure 3.9: Convergence rate of $\max|\phi_{23} - \phi_{23}^{\mathrm{ho}}|$ with respect to: (a) γ_r; (b) β.

Table 3.11: Error analysis of $\frac{\max|\phi_{23}-\phi_{23}^{\rm ho}|}{\max|\phi_{23}|}$ for dimension deduction from 3D to 1D.

$\frac{1}{\gamma_r}$	1/12.5	1/25	1/50	1/100	1/200
$\beta = 25$	0.1727	0.1412	0.1145	0.09240	0.07428
rate		0.29	0.30	0.31	0.32
$\beta = 50$	0.2591	0.2135	0.1746	0.1419	0.1148
rate		0.28	0.29	0.30	0.31
$\beta = 100$	0.3778	0.3151	0.2606	0.2141	0.1748
rate		0.26	0.27	0.28	0.29
$\beta = 200$	0.5334	0.4517	0.3791	0.3156	0.2608
rate		0.24	0.25	0.26	0.28
$\beta = 400$	0.7285	0.6266	0.5345	0.4521	0.3792
rate		0.22	0.23	0.24	0.25

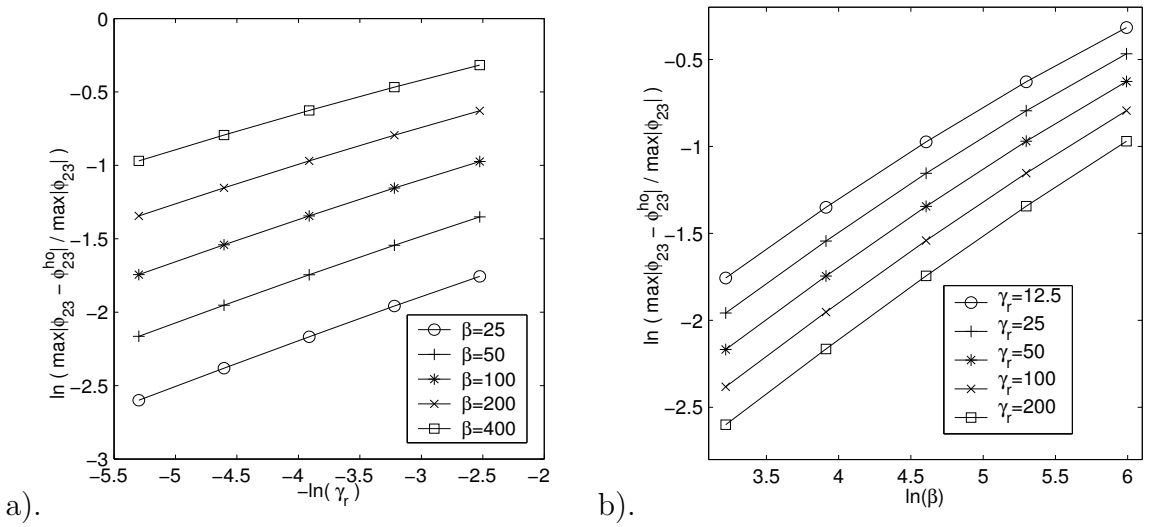

Figure 3.10: Convergence rate of $\frac{\max|\phi_{23}-\phi_{23}^{\rm ho}|}{\max|\phi_{23}|}$ with respect to: (a) γ_r; (b) β.

Table 3.12: Error analysis of $||(\phi_{23})^2 - (\phi_{23}^{\rm ho})^2||_{L^1}$ for dimension deduction from 3D to 1D.

$\frac{1}{\gamma_r}$	1/12.5	1/25	1/50	1/100	1/200
$\beta_3 = 25$	0.2001	0.1651	0.1350	0.1097	0.08864
rate		0.28	0.29	0.30	0.31
$\beta_3 = 50$	0.2922	0.2441	0.2019	0.1658	0.1352
rate		0.26	0.27	0.28	0.29
$\beta_3 = 100$	0.4108	0.3490	0.2936	0.2446	0.2021
rate		0.24	0.25	0.26	0.28
$\beta_3 = 200$	0.5526	0.4796	0.4117	0.3494	0.2937
rate		0.20	0.22	0.24	0.25
$\beta_3 = 400$	0.7102	0.6305	0.5532	0.4799	0.4117
rate		0.17	0.19	0.21	0.22

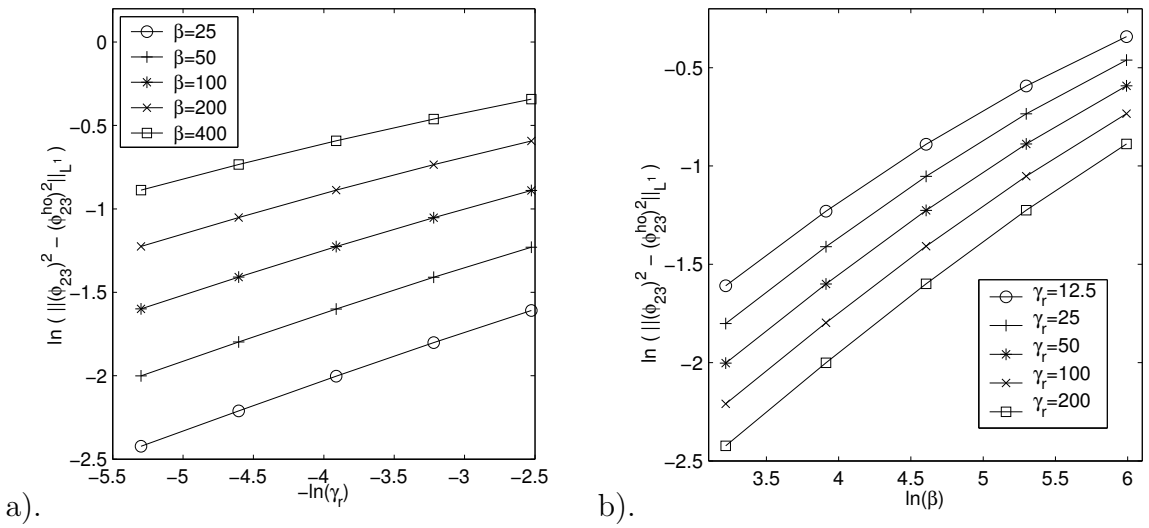

a). b).

Figure 3.11: Convergence rate of $||(\phi_{23})^2 - (\phi_{23}^{\rm ho})^2||_{L^1}$ with respect to: (a) γ_r; (b) β.

Table 3.13: Error analysis of $\frac{||(\phi_{23})^2-(\phi_{23}^{\rm ho})^2||_{L^1}}{||(\phi_{23})^2||_{L^1}}$ for dimension deduction from 3D to 1D.

$\frac{1}{\gamma_r}$	1/12.5	1/25	1/50	1/100	1/200
$\beta_3 = 25$	0.2001	0.1651	0.1350	0.1097	0.08864
rate		0.28	0.29	0.30	0.31
$\beta_3 = 50$	0.2922	0.2441	0.2019	0.1658	0.1352
rate		0.26	0.27	0.28	0.29
$\beta_3 = 100$	0.4108	0.3490	0.2936	0.2446	0.2021
rate		0.24	0.25	0.26	0.28
$\beta_3 = 200$	0.5526	0.4796	0.4117	0.3494	0.2937
rate		0.20	0.22	0.24	0.25
$\beta_3 = 400$	0.7102	0.6305	0.5532	0.4799	0.4117
rate		0.17	0.19	0.21	0.22

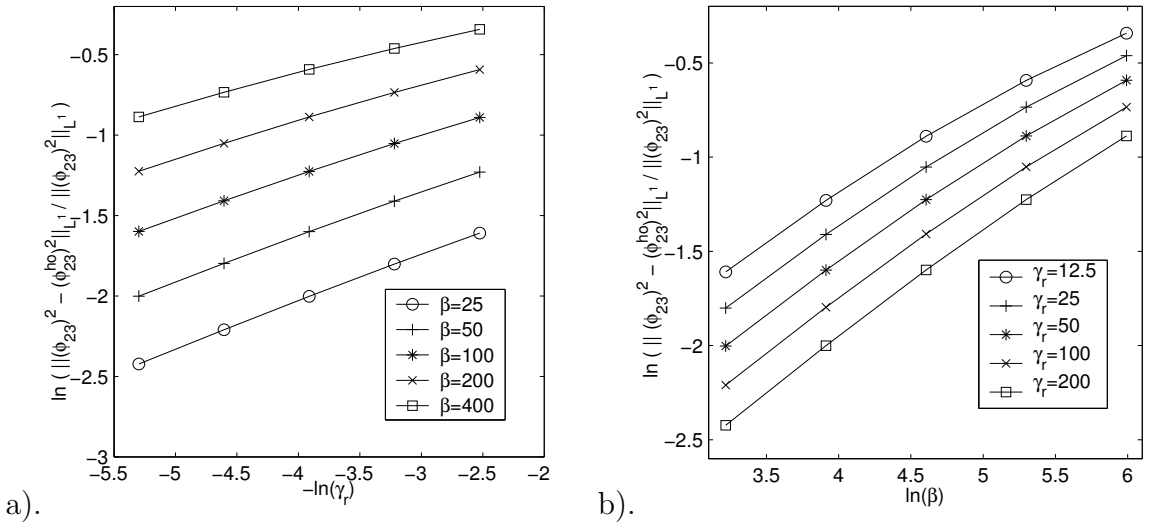

a). b).

Figure 3.12: Convergence rate of $\frac{||(\phi_{23})^2-(\phi_{23}^{\rm ho})^2||_{L^1}}{||(\phi_{23})^2||_{L^1}}$ with respect to: (a) γ_r; (b) β.

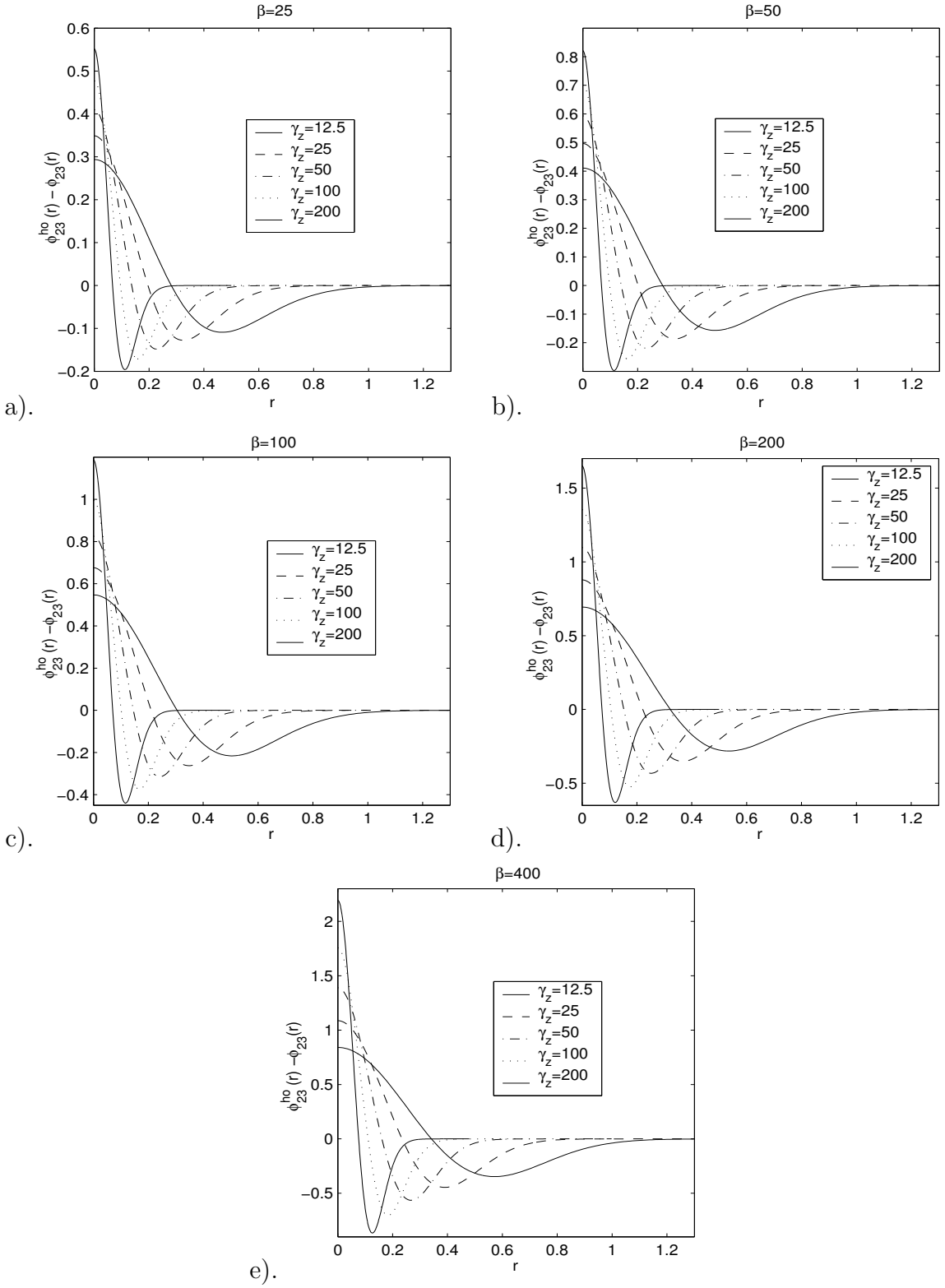

Figure 3.13: Error of $(\phi_{23}(y,z) - \phi_{23}^{\rm ho}(y,z)) = (\phi_{23}(r) - \phi_{23}^{\rm ho}(r))$ as function of r for different β and $\gamma_z = \gamma_y$

From Tables 3.8-3.11 and Figures 3.7-3.10, when $\beta \geq 0$, $\gamma_r := \gamma_y = \gamma_z \gg 1$ and $\beta\gamma_r^{-1} = o(1)$, we can draw the conclusion:

$$\beta_1 = \beta\frac{\gamma_r}{2\pi}\left(1 + O\left(\frac{\beta^{1/3}\ln\gamma_r}{\gamma_r^{1/3}}\right)\right), \qquad \frac{|\beta_1 - \beta_1^{\rm ho}|}{\beta_1} = O\left(\frac{\beta^{1/3}\ln\gamma_r}{\gamma_r^{1/3}}\right),$$
$$\|\phi_{23}(y,z) - \phi_{23}^{\rm ho}(y,z)\|_{L^\infty} = O\left(\beta^{1/3}\gamma_r^{1/3}\ln\gamma_r\right),$$
$$\frac{\|\phi_{23}(y,z) - \phi_{23}^{\rm ho}(y,z)\|_{L^\infty}}{\|\phi_{23}(y,z)\|_{L^\infty}} = O\left(\frac{\beta^{1/3}\ln\gamma_r}{\gamma_r^{1/3}}\right),$$
$$\|\phi_{23}^2(y,z) - (\phi_{23}^{\rm ho})^2(y,z)\|_{L^1} = O\left(\beta^{1/3}\gamma_r^{1/3}\ln\gamma_r\right),$$
$$\frac{\|\phi_{23}^2(y,z) - (\phi_{23}^{\rm ho})^2(y,z)\|_{L^1}}{\|\phi_{23}^2(y,z)\|_{L^1}} = O\left(\frac{\beta^{1/3}\ln\gamma_r}{\gamma_r^{1/3}}\right).$$

Furthermore, from Figure 3.13, we can see that for fixed β, $\phi_{23}(y,z)$ does not converge to $\phi_{23}^{ho}(y,z)$ pointwisely when $\gamma_r \to +\infty$.

3.3 GPE and conservation laws

In fact, the 3D GPE (2.5), 2D GPE (3.5) and 1D GPE (3.11) can be written in a unified way [30, 7, 8]:

$$i\,\frac{\partial\psi(\mathbf{x},t)}{\partial t} = -\frac{1}{2}\triangle\psi(\mathbf{x},t) + V_d(\mathbf{x})\psi(\mathbf{x},t) + \beta_d\,|\psi(\mathbf{x},t)|^2\psi(\mathbf{x},t), \qquad (3.13)$$
$$\psi(\mathbf{x},0) = \psi_0(\mathbf{x}), \quad \mathbf{x}\in\mathbb{R}^d, \qquad d = 1,2,3, \qquad (3.14)$$

where $\beta_3 = \beta$ and

$$V_d(\mathbf{x}) = \frac{1}{2}\begin{cases} x^2, & \text{d=1,} \\ (x^2+\gamma_y^2y^2), & \text{d=2,} \\ (x^2+\gamma_y^2y^2+\gamma_z^2z^2), & \text{d=3.} \end{cases}$$

There are two important invariants of (3.13), i.e. the normalization of the wave function

$$N(\psi) = \int_{\mathbb{R}^d}|\psi(\mathbf{x},t)|^2\,d\mathbf{x} \equiv N(\psi_0) = \int_{\mathbb{R}^d}|\psi_0(\mathbf{x})|^2\,d\mathbf{x} = 1, \quad t\geq 0, \qquad (3.15)$$

and the energy

$$E(\psi) = \int_{\mathbb{R}^d}\left[\frac{1}{2}|\nabla\psi|^2 + V_d(\mathbf{x})|\psi|^2 + \frac{\beta_d}{2}|\psi|^4\right]d\mathbf{x} \equiv E(\psi_0), \quad t\geq 0. \qquad (3.16)$$

3.4 Ground state of GPE and its approximation

To find a stationary solution of (3.13), we write:

$$\psi(\mathbf{x},t) = e^{-i\mu t}\phi(\mathbf{x}), \tag{3.17}$$

where μ is the chemical potential of the condensate and ϕ is a real function independent of time. Inserting (3.17) into (3.13) and (3.15) gives the following equation for $\phi(\mathbf{x})$:

$$\mu\phi(\mathbf{x}) = -\frac{1}{2}\triangle\phi(\mathbf{x}) + V(\mathbf{x})\phi(\mathbf{x}) + \beta_d|\phi(\mathbf{x})|^2\phi(\mathbf{x}), \qquad \mathbf{x}\in\mathbb{R}^d \tag{3.18}$$

under the normalization condition:

$$N(\phi) \triangleq \|\phi\|^2 = \int_{\mathbb{R}^d} |\phi(\mathbf{x})|^2 d\mathbf{x} = 1. \tag{3.19}$$

This is a nonlinear eigenvalue problem under a constraint and any eigenvalue μ can be computed from its corresponding eigenfunction ϕ by:

$$\begin{aligned} \mu = \mu(\phi) &= \int_{\mathbb{R}^d} \left[\frac{1}{2}|\nabla\phi(\mathbf{x})|^2 + V(\mathbf{x})|\phi(\mathbf{x})|^2 + \beta_d|\phi(\mathbf{x})|^4\right] d\mathbf{x} \\ &= E(\phi) + E_{\text{int}}(\phi), \end{aligned} \tag{3.20}$$

where $E_{\text{int}}(\phi)$ denotes the two-body interaction energy:

$$E_{\text{int}}(\phi) = \int_{\mathbb{R}^d} \frac{\beta_d}{2}|\phi(\mathbf{x})|^4 d\mathbf{x}. \tag{3.21}$$

In fact, the eigenfunctions of (3.18) under the constraint (3.19) are equivalent to the critical points of the energy functional $E(\phi)$ over the unit sphere

$$S = \left\{\phi \mid \|\phi\|^2 = 1, \quad E(\phi) < \infty\right\}.$$

Furthermore, as noted in [9], the solutions of (3.18) are equivalent to the steady state solutions of the following continuous normalized gradient flow (CNGF):

$$\frac{\partial\phi}{\partial t} = \frac{1}{2}\triangle\phi - V(\mathbf{x})\phi - \beta_d|\phi|^2\phi + \frac{\mu(\phi)}{\|\phi(\cdot,t)\|^2}\phi, \quad \mathbf{x}\in\mathbb{R}^d, \quad t\geq 0 \tag{3.22}$$

$$\phi(\mathbf{x},0) = \phi_0(\mathbf{x}), \quad \mathbf{x}\in\mathbb{R}^d \quad \text{with} \quad \|\phi_0\| = 1. \tag{3.23}$$

The Bose-Einstein condensate ground state $\phi_g(\mathbf{x})$ is a real non-negative function found by minimizing the energy $E(\phi)$ over the unit sphere S; i.e. find $(\mu_g, \phi_g \in S)$, s.t.

$$E(\phi_g) = \min_{\phi \in S} E(\phi), \quad \mu_g = \mu(\phi_g) = E(\phi_g) + E_{\rm int}(\phi_g), \tag{3.24}$$

The existence of unique positive minimizer of the minimization problem (3.24) was given in [44]. And different numerical methods were proposed in the literatures for computing the ground state of BEC [9, 31, 4, 5, 7, 23, 24].

For a weakly interacting condensate, i.e. $\beta_d = \circ(1)$, we drop the nonlinear term, i.e. the last term on the right-hand side of (3.18), and get the harmonic oscillator approximation:

$$\mu_g^{\rm ho}\phi_g^{\rm ho}(\mathbf{x}) = -\frac{1}{2}\triangle\phi_g^{\rm ho}(\mathbf{x}) + V_d(\mathbf{x})\phi_g^{\rm ho}(\mathbf{x}), \qquad \mathbf{x} \in \mathbb{R}^d. \tag{3.25}$$

The ground state solution of (3.25) is

$$\mu_g^{\rm ho} = \frac{1}{2}\begin{cases} 1, & \\ 1+\gamma_y, & \\ 1+\gamma_y+\gamma_z, & \end{cases} \qquad \phi_g^{\rm ho}(\mathbf{x}) = \frac{1}{(\pi)^{d/4}}\begin{cases} e^{-x^2/2}, & \text{d=1,} \\ \gamma_y^{1/4} e^{-(x^2+\gamma_y y^2)/2}, & \text{d=2,} \\ (\gamma_y\gamma_z)^{1/4} e^{-(x^2+\gamma_y y^2+\gamma_z z^2)/2}, & \text{d=3.} \end{cases} \tag{3.26}$$

This solution can be viewed as an approximate ground state solution of (3.13) in the case of a weakly interacting condensate, i.e. $\beta_d = \circ(1)$, with an $O(\beta)$-error in approximating the chemical potential and the energy.

For a condensate with strong repulsive interactions, i.e. $\beta_d \gg 1$, we drop the diffusion term, i.e. the first term on the right-hand side of (3.13), and get the Thomas Fermi approximation:

$$\mu_g^{\rm TF}\ \phi_g^{\rm TF}(\mathbf{x}) = V_d(\mathbf{x})\phi_g^{\rm TF}(\mathbf{x}) + \beta_d|\phi_g^{\rm TF}(\mathbf{x})|^2\phi_g^{\rm TF}(\mathbf{x}), \qquad \mathbf{x} \in \mathbb{R}^d. \tag{3.27}$$

Solving (3.27), we obtain the TF approximation for the ground state:

$$\phi_g^{\rm TF}(\mathbf{x}) = \begin{cases} \sqrt{\left(\mu_g^{\rm TF} - V_d(\mathbf{x})\right)/\beta_d}, & V_d(\mathbf{x}) \le \mu_g^{\rm TF}, \\ 0, & \text{otherwise.} \end{cases} \tag{3.28}$$

Plugging (3.28) into (3.19) with $\phi = \phi_g^{\rm TF}$, we obtain [7, 8]

$$\mu_g^{\rm TF} = \frac{1}{2}\begin{cases} \left(\frac{3\beta_1}{2}\right)^{2/3}, & d=1, \\ \left(\frac{8\beta_2\gamma_y}{2\pi}\right)^{1/2}, & d=2, \\ \left(\frac{15\beta\gamma_y\gamma_z}{4\pi}\right)^{2/5}, & d=3. \end{cases} \tag{3.29}$$

Due to $\phi_g^{\rm TF}(\mathbf{x})$ is not differentiable at $V_d(\mathbf{x}) = \mu_g^{\rm TF}$, as observed in [7, 8, 11], $E(\phi_g^{\rm TF}) = \infty$, thus one can't use the definition (3.16) to define the energy of the TF approximation (3.28). According to (3.20) and (3.21), as observed in [11], here we use the following way to calculate it:

$$E_g^{\rm TF} \approx E_g = E(\phi_g) = \mu(\phi_g) - E_{\rm int}(\phi_g) \approx \mu_g^{\rm TF} - E_{\rm int}(\phi_g^{\rm TF}) = \frac{d+2}{d+4}\mu_g^{\rm TF}. \tag{3.30}$$

3.5 Leading-order approximate energy and chemical potential

Let us consider for simplicity a radial trap ($d = 2$ with $\gamma_y = 1$), or spherical trap ($d = 3$ with $\gamma_y = \gamma_z = 1$), the ground state solution of the nonlinear eigenvalue problem (3.18) is symmetric, i.e. $\phi_g(\mathbf{x}) = \phi(r)$ with $r = |\mathbf{x}|$ and satisfies:

$$-\frac{1}{2r^{d-1}}\frac{d}{dr}\left(r^{d-1}\frac{d\phi}{dr}\right) + \left(\frac{r^2}{2} - \mu\right)\phi + \beta_d\phi^3 = 0. \tag{3.31}$$

It is equivalent to:

$$-\frac{1}{2}\frac{d^2\phi}{dr^2} - \frac{d-1}{2r}\frac{d\phi}{dr} + \left(\frac{r^2}{2} - \mu\right)\phi + \beta_d\phi^3 = 0. \tag{3.32}$$

Let R be the radius of the wave function, determined by the equation $\mu^{TF} = V(R)$ which implies $R = \sqrt{2\mu_g^{TF}}$. Near this point, where $|r - R| \ll R$, we have

$$\begin{aligned} V_d(\mathbf{r}) - \mu &\approx V_d(\mathbf{r}) - \mu_g^{TF} = \frac{r^2}{2} - \frac{R^2}{2} \\ &= (r-R)\frac{r+R}{2} \approx (r-R)R. \end{aligned}$$

Moreover, for values of R much larger than the thickness of the boundary, the seconde term in equation (3.32) is negligible. Indeed one can easily check that the effect of the first derivative is much smaller than the one of the second derivative in determining the shape of the profile close to R, when R is sufficiently large. Thus one can approximate the GPE (3.32) in this limit with the new equation:

$$-\frac{1}{2}\frac{d^2\phi}{dr^2} + (r-R)R\phi + \beta_d\phi^3 = 0. \tag{3.33}$$

Let us introduce the dimensionless variable: $s = (r-R)/l$ and let $\phi(r) = \alpha\tilde{\phi}(s)$. Then we get:

$$-\frac{d^2\tilde{\phi}(s)}{ds^2} + 2sl^3R\tilde{\phi}(s) + 2\beta_d\alpha^2l^2\tilde{\phi}^3(s) = 0.$$

Choose l and α such that:

$$\begin{cases} 2Rl^3 = 1, \\ 2\beta_d\alpha^2l^2 = 1. \end{cases} \Rightarrow \begin{cases} l = (2R)^{-1/3}, \\ \alpha = (2^{1/3}\beta_d)^{-1/2}R^{1/3}. \end{cases}$$

Then the equation (3.33) is transformed into:

$$\widetilde{\phi}'' - (s + \widetilde{\phi}^2)\widetilde{\phi} = 0. \tag{3.34}$$

As $s \to +\infty$, $\widetilde{\phi} \to 0$, drop $\widetilde{\phi}^3$ item, then we get:

$$\widetilde{\phi}'' - s\widetilde{\phi} = 0,$$

which implies

$$\widetilde{\phi}(s \to +\infty) \simeq \frac{A}{2s^{1/4}}e^{-\frac{2}{3}s^{2/3}}, \qquad A = 0.794\ . \tag{3.35}$$

As $s \to -\infty$, drop $\widetilde{\phi}''$ term, then we get:

$$s + \widetilde{\phi}^2 = 0\ ,$$

which implies

$$\widetilde{\phi}(s \to -\infty) = \sqrt{-s}\ , \quad \widetilde{\phi}\,'(s \to -\infty) = -\frac{1}{2\sqrt{-s}}\ .$$

Choosing ε such that $l \ll \varepsilon \ll R$, then using $\phi_g \approx \phi_g^{TF}$ for $r \in [0, R-\varepsilon]$ and $\phi(r) = \alpha\tilde{\phi}(s)$ for $r \in [R-\varepsilon, +\infty)$, we get:

$$\begin{aligned} E_{\text{kin}} &= \frac{1}{2}\int_{\mathbb{R}^d} |\nabla\phi|^2 d\mathbf{x} = \frac{1}{2}C_d \int_0^{\infty} (\phi^{'}(r))^2 r^{d-1} dr, \\ &= \frac{C_d}{2}\left[\int_0^{R-\varepsilon} (\phi^{'}(r))^2 r^{d-1} dr + \int_{R-\varepsilon}^{+\infty} |\phi^{'}(r)|^2 r^{d-1} dr\right] . \end{aligned} \tag{3.36}$$

We compute the two terms of (3.36), respectively. The first term is

$$\begin{aligned} \int_0^{R-\varepsilon} (\phi^{'}(r))^2 r^{d-1} dr &\approx \int_0^{R-\varepsilon} \left(\frac{d\phi^{TF}(r)}{dr}\right)^2 r^{d-1} dr \\ &= \int_0^{R-\varepsilon} \left(\frac{r/\beta_d}{2\sqrt{(\mu^{TF} - \frac{r^2}{2})/\beta_d}}\right)^2 r^{d-1} dr \\ &= \int_0^{R-\varepsilon} \frac{r^{d+1}/\beta_d}{2(2\mu^{TF} - r^2)} dr = \frac{1}{2\beta_d}\int_0^{R-\varepsilon} \frac{r^{d+1}}{2\mu^{TF} - r^2} dr \\ &= \frac{R^d}{4\beta_d}\left[\ln\frac{2R}{\varepsilon} - D_d\right] , \end{aligned}$$

and the second term is

$$\begin{aligned} &\int_{R-\varepsilon}^{+\infty} |\phi^{'}(r)|^2 r^{d-1} dr \\ = &\int_{-\varepsilon/l}^{\infty} \frac{\alpha^2}{l^2} |\widetilde{\phi}^{'}(s)|^2 (ls+R)^{d-1} l ds = \frac{\alpha^2 R^{d-1}}{l}\int_{-\varepsilon/l}^{\infty} |\widetilde{\phi}^{'}(s)|^2 (1+\frac{ls}{R})^{d-1} ds \\ \approx &\frac{\alpha^2 R^{d-1}}{l}\int_{-\varepsilon/l}^{\infty} |\widetilde{\phi}^{'}(s)|^2 ds \qquad (|r-R| \ll R \Rightarrow 1 + \frac{ls}{R} = \frac{r}{R} \approx 1) \\ = &\frac{\alpha^2 R^{d-1}}{l}\int_{-\varepsilon/l}^{\infty} |\widetilde{\phi}^{'}(s)|^2 \sqrt{1+s^2}\, d\ln(s+\sqrt{1+s^2}) \\ = &\frac{\alpha^2 R^{d-1}}{l}\left[|\widetilde{\phi}^{'}(s)|^2 \sqrt{1+s^2}\ln(s+\sqrt{1+s^2})\Big|_{-\varepsilon/l}^{\infty} + C\right] \\ = &\frac{\alpha^2 R^{d-1}}{l}\left[-\frac{1}{4\varepsilon/l}\sqrt{1+\frac{\varepsilon^2}{l^2}}\ln(\sqrt{1+\varepsilon^2/l^2} - \frac{\varepsilon}{l}) + C\right] \\ = &\frac{\alpha^2 R^{d-1}}{l}\left[-\frac{1}{4}\sqrt{1+\frac{l^2}{\varepsilon^2}}\ln\frac{1}{\frac{\varepsilon}{l} + \sqrt{1+\frac{\varepsilon^2}{l^2}}} + C\right] \\ \approx &\frac{\alpha^2 R^{d-1}}{4l}\left[\ln\frac{2\varepsilon}{l} + 4C\right] = \frac{R^d}{4\beta_d}\left[\ln\frac{2\varepsilon}{l} + 4C\right]. \end{aligned}$$

Summing the two terms together, we get

$$\begin{aligned} E_{\text{kin}} &= \frac{C_d}{2}\left[\frac{R^d}{4\beta_d}(\ln\frac{2R}{\varepsilon}-D_d)+\frac{R^d}{4\beta_d}(\ln\frac{2\varepsilon}{l}+4C)\right] \\ &= \frac{C_dR^d}{8\beta_d}\left[\ln\frac{4R}{l}+4C-D_d\right] \\ &= \frac{C_dR^d}{8\beta_d}\left[\ln\frac{4R}{(2R)^{-1/3}}+4C-D_d\right] \\ &= \frac{C_dR^d}{8\beta_d}\left[\ln R^{4/3}+\frac{7}{3}\ln 2+4C-D_d\right], \end{aligned}$$

where

$$C_d=\begin{cases}2, & \\ 2\pi, & \\ 4\pi, & \end{cases} \qquad D_d=\begin{cases}2, & d=1,\\ 1+\ln 4, & d=2,\\ \frac{8}{3}, & d=3,\end{cases}$$

$$R=\sqrt{2\mu_g^{TF}}=\begin{cases}(\frac{3\beta_1}{2})^{1/3}, & \\ (\frac{4\beta_2}{\pi})^{1/4}, & \\ (\frac{15\beta}{4\pi})^{1/5}, & \end{cases} \qquad \beta_d=\begin{cases}\frac{\beta}{2\pi}, & d=1,\\ \frac{\beta}{\sqrt{2\pi}}, & d=2,\\ \beta, & d=3,\end{cases}$$

$$\begin{aligned} C &= -\int_{-\varepsilon/l}^{+\infty}\ln(\sqrt{1+s^2}+s)\frac{d}{ds}[(\phi')^2\sqrt{1+s^2}]ds \\ &\approx 0.176. \end{aligned}$$

Let:

$$A_d=\begin{cases}\frac{1}{4}(\frac{3}{2})^{1/3}, & d=1,\\ \frac{\sqrt{\pi}}{2}, & d=2,\\ \frac{\pi}{2}(\frac{15}{4\pi})^{3/5}, & d=3,\end{cases} \qquad B_d=\begin{cases}2^{\frac{7}{3}}e^{4C-D_1}(\frac{3}{2})^{4/9}, & d=1,\\ 2^{\frac{7}{3}}e^{4C-D_2}(\frac{4}{\pi})^{1/3}, & d=2,\\ 2^{\frac{7}{3}}e^{4C-D_3}(\frac{15}{4\pi})^{4/15}, & d=3,\end{cases}$$

$$\begin{aligned} H_d &= \frac{C_d^{2/(d+2)}[(d+1)^2-1]^{d/(d+2)}}{6(d+2)}, \qquad d=1,2,3, \\ G_d &= \ln\frac{(d+1)^2-1}{C_d}+(d+2)\left(\frac{7}{4}\ln 2+3C-\frac{3}{4}D_d\right), \end{aligned}$$

We get:

$$\begin{aligned} E_{\text{kin}} &= \frac{C_d R^d}{8\beta_d}\left[\ln R^{4/3} + \frac{7}{3}\ln 2 + 4C - D_d\right] \\ &= (A_d \frac{4}{3(d+2)})\beta_d^{-\frac{2}{d+2}} \ln\beta_d + (A_d \ln B_d)\beta_d^{-\frac{2}{d+2}} \\ &= \frac{H_d}{\beta_d^{2/(d+2)}}(\ln\beta_d + G_d). \end{aligned} \tag{3.37}$$

Thus when $\beta_d \gg 1$, we get the first order approximation for E_g and μ_g

$$\begin{aligned} E_g &\approx E_g^{\text{TF}} + E_{\text{kin}}(\phi_g) && (3.38) \\ &\approx \frac{d+2}{2(d+4)}\left[\frac{((d+1)^2-1)\beta_d}{C_d}\right]^{2/(d+2)} + \frac{H_d}{\beta_d^{2/(d+2)}}(\ln\beta_d + G_d) \\ &= \frac{d+2}{2(d+4)}\left[\frac{((d+1)^2-1)\beta_d}{C_d}\right]^{2/(d+2)} + O\left(\frac{\ln\beta_d}{\beta_d^{2/(d+2)}}\right), && (3.39) \end{aligned}$$

$$\begin{aligned} \mu_g &\approx \mu_g^{\text{TF}} + E_{\text{kin}}(\phi_g) && (3.40) \\ &\approx \frac{1}{2}\left[\frac{((d+1)^2-1)\beta_d}{C_d}\right]^{2/(d+2)} + \frac{H_d}{\beta_d^{2/(d+2)}}(\ln\beta_d + G_d) \\ &= \frac{1}{2}\left[\frac{((d+1)^2-1)\beta_d}{C_d}\right]^{2/(d+2)} + O\left(\frac{\ln\beta_d}{\beta_d^{2/(d+2)}}\right). && (3.41) \end{aligned}$$

These asymptotic results were confirmed by the numerical results in [7] for $d = 1, 2, 3$.

Chapter 4

Approximate Ground States in 3D

In this chapter, we will derive approximate ground states as well as their energy and chemical potential of 3D GPE (2.5) with $d = 3$ and external potential $V(\mathbf{x}) = \frac{1}{2}\left(x^2 + \gamma_y^2 y^2 + \gamma_z^2 z^2\right)$ with $\mathbf{x} = (x, y, z)$ for different parameters regimes of β, γ_y and γ_z, by applying the results in the previous chapter.

4.1 Isotropic shaped condensation

In the case of isotropic shaped condensation, i.e. $\gamma_y = O(1)$ and $\gamma_z = O(1)$ ($\Longleftrightarrow$ $\omega_y \approx \omega_x$ and $\omega_z \approx \omega_x$), there are three typical regimes:

4.1.1 Weakly interacting regime

When $\beta = o(1)$, i.e. in a weakly interacting regime, the ground state is approximated by the harmonic oscillator ground state:

$$\phi_g(\mathbf{x}) \approx \phi_g^{\mathrm{ho}}(x, y, z) = \frac{(\gamma_y\gamma_z)^{1/4}}{\pi^{3/4}} e^{-(x^2+\gamma_y y^2+\gamma_z z^2)/2}, \qquad \mathbf{x} \in \mathbb{R}^3, \tag{4.1}$$

$$E_g \approx \frac{1}{2}\left(1 + \gamma_y + \gamma_z\right) + O(\beta), \qquad |\beta| \ll 1, \tag{4.2}$$

$$\mu_g \approx \frac{1}{2}\left(1 + \gamma_y + \gamma_z\right) + O(\beta). \tag{4.3}$$

4.1.2 Intermediate repulsive interacting regime

When $\beta = O(1)$, i.e. in a intermediate repulsive interacting regime, the ground state can be obtained by solving the 3D minimization problem (2.15). Different numerical methods were proposed in the literatures for computing the ground states [7, 9, 12, 23, 24].

4.1.3 Strong repulsive interacting regime

When $\beta \gg 1$, i.e. in a strong repulsive interacting regime, the ground state is approximated by the TF approximation:

$$\mu_g^{\rm TF} = \frac{1}{2}\left(\frac{15\beta\gamma_y\gamma_z}{4\pi}\right)^{2/5}, \quad \phi_g(\mathbf{x}) \approx \begin{cases} \sqrt{\left(\mu_g^{\rm TF} - V(\mathbf{x})\right)/\beta}, & V(\mathbf{x}) < \mu_g^{\rm TF}, \\ 0 & \text{otherwise}, \end{cases} \tag{4.4}$$

$$E_g \approx \frac{5}{7}\mu_g^{\rm TF} + \frac{H_3}{\beta^{2/5}}(\ln\beta + G_3) = \frac{5}{7}\mu_g^{\rm TF} + O\left(\frac{\ln\beta}{\beta^{2/5}}\right), \qquad \beta \gg 1, \tag{4.5}$$

$$\mu_g \approx \mu_g^{\rm TF} + \frac{H_3}{\beta^{2/5}}(\ln\beta + G_3) = \mu_g^{\rm TF} + O\left(\frac{\ln\beta}{\beta^{2/5}}\right). \tag{4.6}$$

For $\gamma_y = \gamma_z = 1$, (4.5) and (4.6) were confirmed numerically in [7].

4.2 Disk-shaped condensation

In the case of disk shaped condensation, i.e. $\gamma_y = O(1)$ and $\gamma_z \gg 1$ ($\Longleftrightarrow \omega_y \approx \omega_x$ and $\omega_z \gg \omega_x$), we set

$$\mu_g \approx \mu + \frac{\gamma_z}{2}, \qquad \phi_g(\mathbf{x}) \approx \phi_{12}(x,y)\phi_3^{\rm ho}(z) \quad \text{with } \phi_3^{\rm ho}(z) = \frac{\gamma_z^{1/4}}{\pi^{1/4}} e^{-\gamma_z z^2/2}. \tag{4.7}$$

Plugging (4.7) into (2.9), multiplying both sides by $\phi_3^{\rm ho}(z)$ and integrating over $z \in (-\infty, \infty)$, we get

$$\mu\ \phi(x,y) = -\frac{1}{2}\Delta\phi + V_2(x,y)\phi + \beta_2\ |\phi|^2\phi, \qquad (x,y) \in \mathbb{R}^2, \tag{4.8}$$

where $V_2(x,y) = \frac{1}{2}\left(x^2 + \gamma_y^2 y^2\right)$ and $\beta_2 = \beta\sqrt{\frac{\gamma_z}{2\pi}}$. Using the results in the previous section for 2D GPE, again we get approximate ground state in three typical regimes:

4.2.1 Weakly interacting regime

When $\beta_2 = o(1)$, i.e. in a weakly interacting regime, the ground state is approximated by the harmonic oscillator ground state:

$$\phi_g(\mathbf{x}) \approx \phi_{12}^{\mathrm{ho}}(x,y)\phi_3^{\mathrm{ho}}(z) = \phi_g^{\mathrm{ho}}(x,y,z), \qquad \mathbf{x} \in \mathbb{R}^3, \tag{4.9}$$

$$E_g \approx \frac{\gamma_z}{2} + \frac{1+\gamma_y}{2} + O(\beta_2^{ho}) = \frac{\gamma_z}{2} + \frac{1+\gamma_y}{2} + O\left(\beta\gamma_z^{1/2}\right), \tag{4.10}$$

$$\mu_g \approx \frac{\gamma_z}{2} + \frac{1+\gamma_y}{2} + O(\beta_2^{ho}) = \frac{\gamma_z}{2} + \frac{1+\gamma_y}{2} + O\left(\beta\gamma_z^{1/2}\right), \ \gamma_z \gg 1 \& \beta_2^{ho} \ll 1. \tag{4.11}$$

4.2.2 Intermediate or strong repulsive interacting regime

When $\beta_2 = O(1)$ or $\beta_2 \gg 1$, i.e. in a intermediate or strong repulsive interacting regime, the ground state can be approximated by

$$\phi_g(\mathbf{x}) \approx \phi_g^{\mathrm{DS}}(\mathbf{x}) := \phi_g^{\mathrm{2D}}(x,y)\phi_3^{\mathrm{ho}}(z), \qquad \mathbf{x} \in \mathbb{R}^3. \tag{4.12}$$

$$E_g \approx E_g^{\mathrm{DS}} := E(\phi_g^{\mathrm{2D}}(x,y)\phi_3^{\mathrm{ho}}(z)) = \frac{\gamma_z}{2} + E_{\mathrm{2D}}(\phi_g^{\mathrm{2D}}) := \frac{\gamma_z}{2} + E_g^{\mathrm{2D}}, \tag{4.13}$$

$$\mu_g \approx \mu_g^{\mathrm{DS}} := \mu(\phi_g^{\mathrm{2D}}(x,y)\phi_3^{\mathrm{ho}}(z)) = \frac{\gamma_z}{2} + \mu_{\mathrm{2D}}(\phi_g^{\mathrm{2D}}) := \frac{\gamma_z}{2} + \mu_g^{\mathrm{2D}}, \tag{4.14}$$

where

$$E_g^{\mathrm{2D}} = \int_{\mathbb{R}^2} \left[\frac{1}{2}|\nabla\phi_g^{\mathrm{2D}}|^2 + V_2(x,y)|\phi_g^{\mathrm{2D}}|^2 + \frac{\beta_2^{ho}}{2}|\phi_g^{\mathrm{2D}}|^4\right] dxdy,$$

$$\mu_g^{\mathrm{2D}} = \int_{\mathbb{R}^2} \left[\frac{1}{2}|\nabla\phi_g^{\mathrm{2D}}|^2 + V_2(x,y)|\phi_g^{\mathrm{2D}}|^2 + \beta_2^{ho}|\phi_g^{\mathrm{2D}}|^4\right] dxdy.$$

Here ϕ_g^{2D}, E_g^{2D} and μ_g^{2D} are the ground state, energy and chemical potential of the 2D problem (4.8). In this case, one needs only solve a 2D problem numerically and thus computational time, memory and cost are saved significantly.

To verify (4.12), (4.13) and (4.14) numerically, we solve (3.13) with BEFD discretization method we reviewed in chapter 2 for $d = 2, 3$. The computational domain is chosen as $(r, z) \in [0, R] \times [-a, a]$ in the algorithm (2.21)-(2.22). The choice of R and a is listed in Table 3.1 for different β and γ_z for the 3D GPE. The computational

domain for 2D GPE is chosen as $r \in [0, R]$. The choice of R is also listed in Table 3.1. Then we get $\phi_g(x, y, z)$ and $\phi_g^{2D}(x, y)$. We got $\phi_3^{ho}(z)$ by (3.3). Finally we compare $\phi_g(x, y, z)$ with $\phi_g^{\mathrm{DS}}(\mathbf{x}) := \phi_g^{\mathrm{2D}}(x, y)\phi_3^{\mathrm{ho}}(z)$.

Table 4.1 lists the error $\max|\phi_g - \phi_g^{DS}|$, Table 4.2 lists the error $||\phi_g - \phi_g^{DS}||_{L^2}$, Table 4.3 lists the error $\max|(\phi_g)^2 - (\phi_g^{DS})^2|$, Table 4.4 lists the error $||(\phi_g)^2 - (\phi_g^{DS})^2||_{L^1}$, Table 4.5 lists the error $|E_g - E_g^{DS}|$ and Table 4.6 lists the error $|\mu_g - \mu_g^{DS}|$ for different β and γ_z.

Furthermore, Figure 4.1 shows the error $\max|\phi_g - \phi_g^{DS}|$, Figure 4.2 shows the error $||\phi_g - \phi_g^{DS}||_{L^2}$, Figure 4.3 shows the error $||(\phi_g)^2 - (\phi_g^{DS})^2||_{L^1}$, Figure 4.4 shows the error $|E_g - E_g^{DS}|$ and Figure 4.5 shows the error $|\mu_g - \mu_g^{DS}|$ for different β and γ_z.

Table 4.1: Error analysis of $\max|\phi_g - \phi_g^{DS}|$ for the ground state in 3D with a disk-shaped trap.

$1/\gamma_z$	1/25	1/100	1/400	1/1600
$\beta_3 = 1$	2.7165e-03	1.6256e-03	8.6990e-04	4.6582e-04
rate		0.37	0.45	0.45
$\beta_3 = 10$	9.9580e-03	4.4016e-03	1.8771e-03	7.8922e-04
rate		0.59	0.61	0.63
$\beta = 100$	1.8283e-02	7.8510e-03	3.3251e-03	1.4279e-03
rate		0.61	0.62	0.61
$\beta = 1000$	2.9793e-02	1.3614e-02	5.8602e-03	2.5056e-03
rate		0.56	0.61	0.61
$\beta_3 = 10000$	3.8178e-02	2.1891e-02	1.0138e-02	4.8558e-03
rate		0.40	0.56	0.53

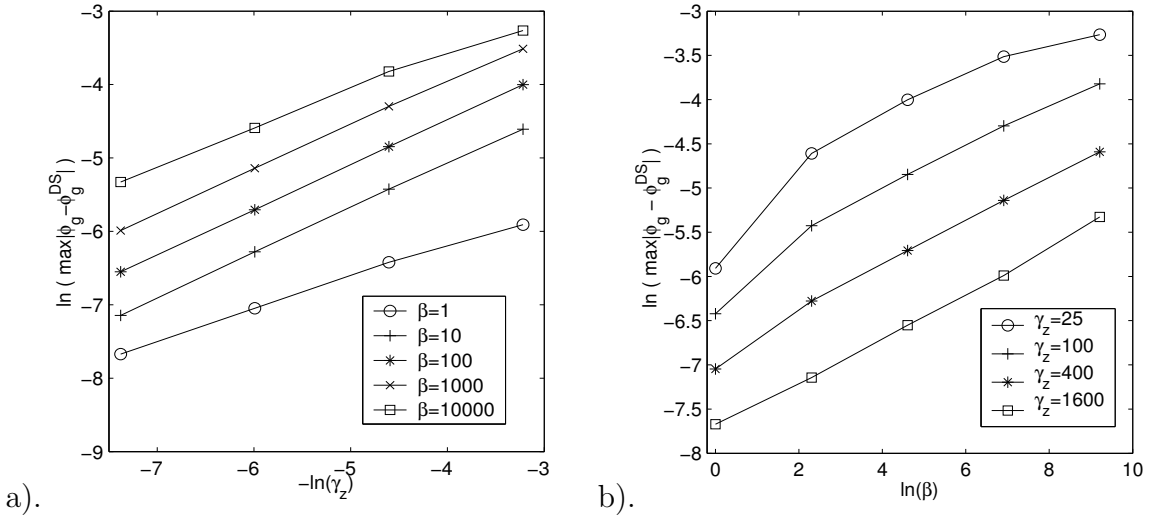

a). b).

Figure 4.1: Convergence rate of $\max|\phi_g - \phi_g^{DS}|$ in 3D with a disk-shaped trap with respect to: (a) γ_z; (b) β.

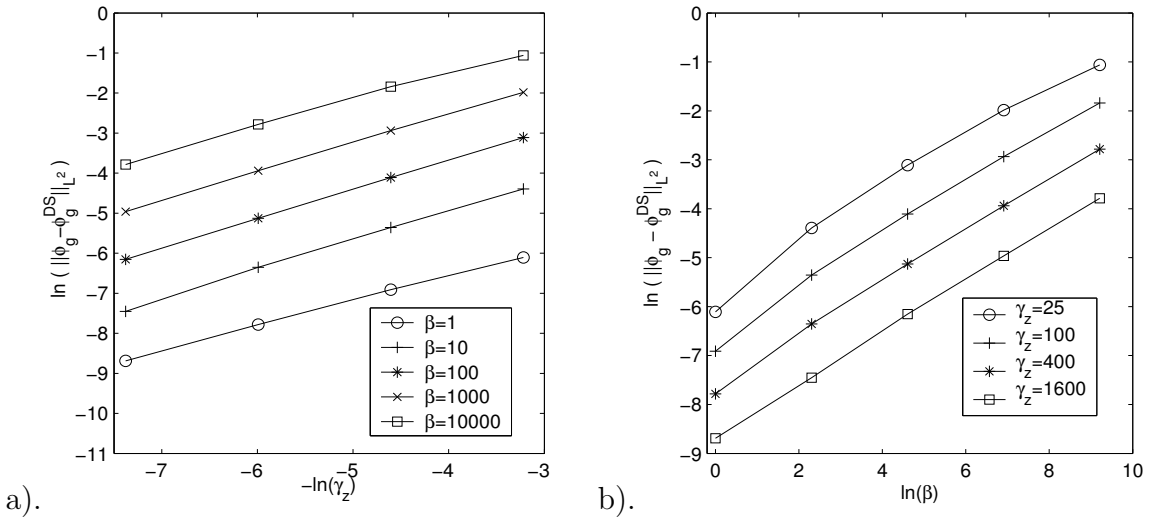

a). b).

Figure 4.2: Convergence rate of $||\phi_g - \phi_g^{DS}||_{L^2}$ in 3D with a disk-shaped trap with respect to: (a) γ_z; (b) β.

Table 4.2: Error analysis of $||\phi_g - \phi_g^{DS}||_{L^2}$ for the ground state in 3D with a disk-shaped trap.

$1/\gamma_z$	1/25	1/100	1/400	1/1600
$\beta_3 = 1$	2.2292e-03	9.9667e-04	4.1720e-04	1.6839e-04
rate		0.58	0.63	0.65
$\beta_3 = 10$	1.2352e-02	4.7214e-03	1.7425e-03	5.8019e-04
rate		0.70	0.72	0.80
$\beta_3 = 100$	4.4559e-02	1.6419e-02	5.9334e-03	2.1262e-03
rate		0.72	0.73	0.74
$\beta_3 = 1000$	0.13758	5.3087e-02	1.9432e-02	6.9931e-03
rate		0.69	0.73	0.74
$\beta_3 = 10000$	0.34614	0.15876	6.1901e-02	2.2674e-02
rate		0.56	0.68	0.72

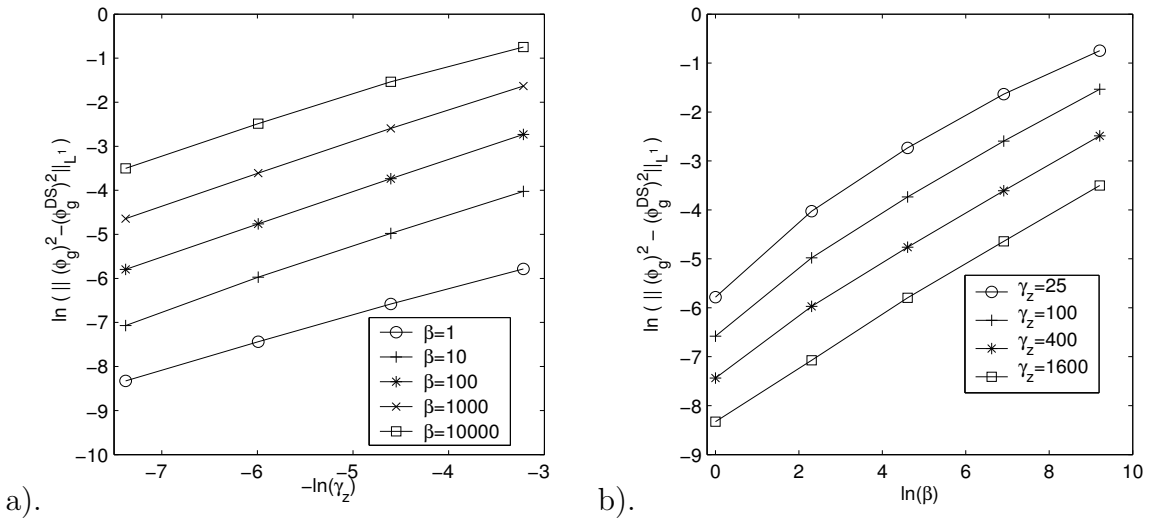

Figure 4.3: Convergence rate of $||(\phi_g)^2 - (\phi_g^{DS})^2||_{L^1}$ in 3D with a disk-shaped trap with respect to: (a) γ_z; (b) β.

Table 4.3: Error analysis of $\max|(\phi_g)^2 - (\phi_g^{DS})^2|$ for the ground state in 3D with a disk-shaped trap.

$1/\gamma_z$	1/25	1/100	1/400	1/1600
$\beta_3 = 1$	4.2104e-03	2.9316e-03	1.6270e-03	8.9928e-04
rate		0.26	0.42	0.43
$\beta_3 = 10$	6.8158e-03	3.3444e-03	1.6368e-03	9.0873e-04
rate		0.51	0.52	0.42
$\beta_3 = 100$	6.2500e-03	3.2179e-03	1.6262e-03	8.3692e-04
rate		0.48	0.49	0.48
$\beta_3 = 1000$	5.5415e-03	3.1051e-03	1.6050e-03	8.2083e-04
rate		0.42	0.48	0.48
$\beta_3 = 10000$	3.5845e-03	2.7072e-03	1.5437e-03	8.0167-04
rate		0.20	0.40	0.47

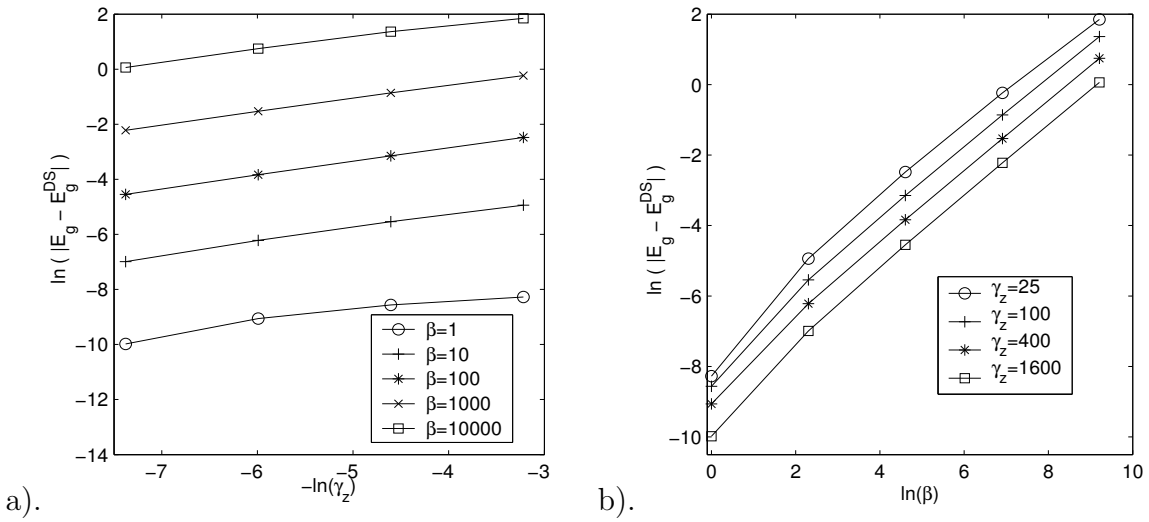

Figure 4.4: Convergence rate of $|E_g - E_g^{DS}|$ in 3D with a disk-shaped trap with respect to: (a) γ_z; (b) β.

Table 4.4: Error analysis of $||(\phi_g)^2 - (\phi_g^{DS})^2||_{L^1}$ for the ground state in 3D with a disk-shaped trap.

$1/\gamma_z$	1/25	1/100	1/400	1/1600
$\beta_3 = 1$	3.0733e-03	1.3850e-03	5.8874e-04	2.4139e-04
rate		0.57	0.62	0.64
$\beta_3 = 10$	1.7851e-02	6.8785e-03	2.5500e-03	8.4851e-04
rate		0.69	0.72	0.79
$\beta_3 = 100$	6.5043e-02	2.3857e-02	8.5544e-03	3.0379e-03
rate		0.72	0.74	0.75
$\beta_3 = 1000$	0.19508	7.4657e-02	2.7047e-02	9.6342e-03
rate		0.69	0.73	0.74
$\beta_3 = 10000$	0.47323	0.21564	8.3192e-02	3.0162e-02
rate		0.57	0.69	0.73

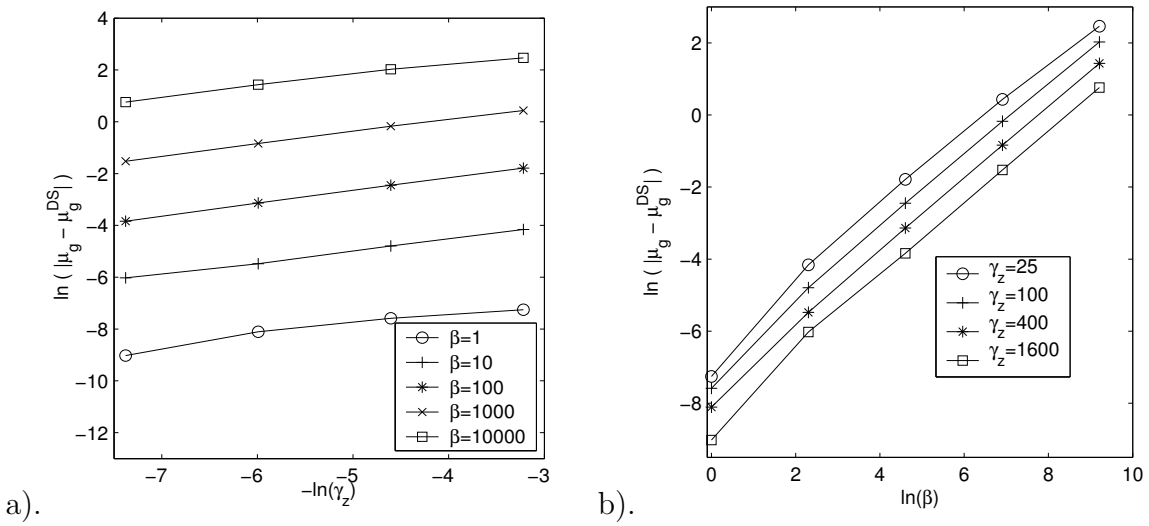

Figure 4.5: Convergence rate of $|\mu_g - \mu_g^{DS}|$ in 3D with a disk-shaped trap with respect to: (a) γ_z; (b) β.

Table 4.5: Error analysis of $|E_g - E_g^{DS}|$ for the ground state in 3D with a disk-shaped trap.

$1/\gamma_z$	1/25	1/100	1/400	1/1600
$\beta_3 = 1$	2.5509e-04	1.9100e-04	1.1598e-04	4.6241e-05
rate		0.21	0.36	0.66
$\beta_3 = 10$	7.1493e-03	3.9211e-03	1.9933e-03	9.2032e-04
rate		0.43	0.49	0.56
$\beta_3 = 100$	8.3553e-02	4.3013e-02	2.1584e-02	1.0604e-02
rate		0.48	0.50	0.51
$\beta_3 = 1000$	0.79026	0.42380	0.21651	0.10841
rate		0.45	0.48	0.50
$\beta_3 = 10000$	6.3418	3.9073	2.1104	1.0662
rate		0.35	0.46	0.49

Table 4.6: Error analysis of $|\mu_g - \mu_g^{DS}|$ for the ground state in 3D with a disk-shaped trap.

$1/\gamma_z$	1/25	1/100	1/400	1/1600
$\beta_3 = 1$	7.0581e-04	5.0744e-04	3.0116e-04	1.2072e-04
rate		0.24	0.38	0.66
$\beta_3 = 10$	1.5620e-02	8.2793e-03	4.1715e-03	2.4183e-03
rate		0.46	0.49	0.39
$\beta_3 = 100$	0.16745	8.6323e-02	4.3446e-02	2.1534e-02
rate		0.48	0.50	0.51
$\beta_3 = 1000$	1.5391	0.84043	0.43244	0.21765
rate		0.44	0.48	0.50
$\beta_3 = 10000$	11.748	7.5786	4.1793	2.1416
rate		0.32	0.44	0.48

From Tables 4.1-4.6 and Figures 4.1-4.5, when $\beta \geq 0$, $\gamma_z \geq 1$ and $\beta\gamma_z^{-3/2} = o(1)$, we can draw the following conclusion:

$$\|\phi_g - \phi_g^{\mathrm{DS}}\|_{L^2} = O\left(\frac{\beta^{1/2}\ \ln\gamma_z}{\gamma_z^{3/4}}\right), \quad \|(\phi_g)^2 - (\phi_g^{\mathrm{DS}})^2\|_{L^1} = O\left(\frac{\beta^{1/2}\ \ln\gamma_z}{\gamma_z^{3/4}}\right),$$
$$|E_g - E_g^{\mathrm{DS}}| = O\left(\frac{\beta\ \ln\gamma_z}{\gamma_z^{1/2}}\right), \quad |\mu_g - \mu_g^{\mathrm{DS}}| = O\left(\frac{\beta\ \ln\gamma_z}{\gamma_z^{1/2}}\right).$$

4.2.3 Strong repulsive interacting regime

When $\beta_2 \gg 1$, i.e. strong repulsive interacting regime, the ground state is approximated by the multiplication of the TF approximation in xy-plane and the harmonic oscillator approximation in z-direction:

$$\phi_g(\mathbf{x}) \approx \phi_g^{\mathrm{TF1}}(\mathbf{x}) := \phi_{2\mathrm{D}}^{\mathrm{TF}}(x,y)\phi_3^{\mathrm{ho}}(z), \qquad \mathbf{x} \in \mathbb{R}^3, \tag{4.15}$$

where

$$\phi_{2\mathrm{D}}^{\mathrm{TF}}(x,y) = \begin{cases} \sqrt{\left(\mu_{2\mathrm{D}}^{\mathrm{TF}} - V_2(x,y)\right)/\beta_2^{ho}}, & V_2(x,y) < \mu_{2\mathrm{D}}^{\mathrm{TF}}, \\ 0 & \text{otherwise}, \end{cases} \tag{4.16}$$

$$\mu_{2\mathrm{D}}^{\mathrm{TF}} = \left(\frac{\beta_2^{ho}\gamma_y}{\pi}\right)^{1/2} = \frac{\beta^{1/2}\gamma_y^{1/2}\gamma_z^{1/4}}{2^{1/4}\pi^{3/4}}. \tag{4.17}$$

Plugging (4.12), (4.8), (3.30) with $d = 2$, (4.17), (3.37) with $d = 2$ and $\beta_2 = \beta_2^{ho}$ into (3.16), we get the approximate energy

$$\begin{aligned} E_g &= E(\phi_g) = E(\phi_g^{2\mathrm{D}}(x,y)\phi_3^{\mathrm{ho}}(z)) + O\left(\frac{\beta\ln\gamma_z}{\gamma_z^{1/2}}\right) \\ &= \frac{\gamma_z}{2} + E_{2\mathrm{D}}(\phi_g^{2\mathrm{D}}) + O\left(\frac{\beta\ln\gamma_z}{\gamma_z^{1/2}}\right) = \frac{\gamma_z}{2} + E_g^{2\mathrm{D}} + O\left(\frac{\beta\ln\gamma_z}{\gamma_z^{1/2}}\right) \\ &\approx \frac{\gamma_z}{2} + \frac{2}{3}\left(\frac{\beta_2^{ho}\gamma_y}{\pi}\right)^{1/2} + \frac{H_2}{(\beta_2^{ho})^{2/4}}(\ln\beta_2^{ho} + G_2) + O\left(\frac{\beta\ln\gamma_z}{\gamma_z^{1/2}}\right) \\ &\approx \frac{\gamma_z}{2} + \frac{2^{3/4}\gamma_y^{1/2}(\beta^2\gamma_z)^{1/4}}{3\pi^{3/4}} + \frac{H_2(2\pi)^{1/4}}{2(\beta^2\gamma_z)^{1/4}}\left[\ln(\beta^2\gamma_z) + 2G_2 - \ln 2\pi\right] + O\left(\frac{\beta\ln\gamma_z}{\gamma_z^{1/2}}\right) \\ &= E_g^{\mathrm{TF1}} + O\left(\frac{\ln(\beta^2\gamma_z)}{(\beta^2\gamma_z)^{1/4}} + \frac{\beta\ln\gamma_z}{\gamma_z^{1/2}}\right), \end{aligned} \tag{4.18}$$

where

$$E_g^{\mathrm{TF1}} = \frac{\gamma_z}{2} + \frac{2^{3/4}\gamma_y^{1/2}(\beta^2\gamma_z)^{1/4}}{3\pi^{3/4}} = \frac{\gamma_z}{2} + \frac{2}{3}\mu_{2D}^{TF}. \tag{4.19}$$

Similarly, we get the approximate chemical potential:

$$\mu_g \approx \mu_g^{\mathrm{TF1}} + O\left(\frac{\ln(\beta^2\gamma_z)}{(\beta^2\gamma_z)^{1/4}} + \frac{\beta\ln\gamma_z}{\gamma_z^{1/2}}\right), \tag{4.20}$$

where

$$\mu_g^{\mathrm{TF1}} = \frac{\gamma_z}{2} + \frac{\gamma_y^{1/2}(\beta^2\gamma_z)^{1/4}}{2^{1/4}\pi^{3/4}} = \frac{\gamma_z}{2} + \mu_{2D}^{TF}. \tag{4.21}$$

To verify (4.15), (4.18) and (4.20) numerically, we solve (3.13) with BEFD discretization method we reviewed in chapter 2 for $d = 3$ and we get $\phi_g(x, y, z)$. The computational domains for 3D GPE and 2D GPE are the same as those in the previous subsection. Then we got $\phi_3^{ho}(z)$ by (3.3) and got $\phi_{2D}^{TF}(x, y)$ by (4.16). Finally we compare $\phi_g(x, y, z)$ with $\phi_g^{\mathrm{TF1}}(x, y, z) := \phi_{2\mathrm{D}}^{TF}(x, y)\phi_3^{\mathrm{ho}}(z)$.

Table 4.7 lists the error $||\phi_g - \phi_g^{TF1}||_{L^2}$, Table 4.8 lists the error $||(\phi_g)^2 - (\phi_g^{TF1})^2||_{L^1}$, Table 4.9 lists the error $|E_g - E_g^{TF1}|$ and Table 4.10 lists the error $|\mu_g - \mu_g^{TF1}|$ for different β and γ_z.

Furthermore, Figure 4.6 shows the error $|E_g - E_g^{TF1}|$ and Figure 4.7 shows the error $|\mu_g - \mu_g^{TF1}|$ for different β and γ_z.

Table 4.7: Error analysis of $||\phi_g - \phi_g^{TF1}||_{L^2}$ for the ground state in 3D with a disk-shaped trap.

$1/\gamma_z$	1/25	1/100	1/400	1/1600
$\beta_3 = 1$	0.54466	0.44370	0.35676	0.28780
rate		0.15	0.16	0.15
$\beta_3 = 10$	0.26575	0.21545	0.17363	0.14040
rate		0.15	0.16	0.15
$\beta_3 = 100$	0.12895	0.10296	8.4337e-02	6.7750e-02
rate		0.16	0.14	0.16
$\beta_3 = 1000$	0.13991	6.4893e-02	4.1214e-02	3.1973e-02
rate		0.55	0.33	0.18
$\beta_3 = 10000$	0.34437	0.15654	6.0349e-02	2.3976e-02
rate		0.57	0.69	0.67

From Tables 4.7-4.10 and Figures 4.6-4.7, when $\beta > 0$, $\gamma_z \geq 1$ and $\beta\gamma_z^{-3/2} = o(1)$, we can draw the following conclusion:

$$\|\phi_g - \phi^{\mathrm{TF1}}\|_{L^2} = O\left(\frac{C(\beta)\ln\gamma_z}{\gamma_z^{1/4}}\right), \quad \|\phi_g^2 - (\phi^{\mathrm{TF1}})^2\|_{L^1} = O\left(\frac{C(\beta)\ln\gamma_z}{\gamma_z^{1/4}}\right),$$
$$|E_g - E_g^{\mathrm{TF1}}| = O\left(\frac{\ln\gamma_z}{\gamma_z^{1/4}} + \beta\right), \qquad |\mu_g - \mu_g^{\mathrm{TF1}}| = O\left(\frac{\ln\gamma_z}{\gamma_z^{1/4}} + \beta\right),$$

where $C(\beta)$ depends on β. These results confirm the asymptotic results (4.18) and (4.20). Furthermore, our numerical results indicate that $(\phi^{\mathrm{TF1}}(\mathbf{x}))^2$ doesn't converges pointwisely to the ground state $\phi_g^2(\mathbf{x})$ when $\gamma_z \to \infty$ and $\beta > 0$.

Table 4.8: Error analysis of $||(\phi_g)^2 - (\phi_g^{TF1})^2||_{L^1}$ for the ground state in 3D with a disk-shaped trap.

$1/\gamma_z$	1/25	1/100	1/400	1/1600
$\beta_3 = 1$	0.58819	0.41360	0.27900	0.18477
rate		0.25	0.28	0.30
$\beta_3 = 10$	0.16239	0.10752	7.1278e-02	4.7097e-02
rate		0.30	0.30	0.30
$\beta_3 = 100$	9.2648e-02	4.5162e-02	2.3347e-02	1.2906e-02
rate		0.52	0.48	0.43
$\beta_3 = 1000$	0.19484	7.5742e-02	2.8252e-02	1.0454e-02
rate		0.68	0.71	0.72
$\beta_3 = 10000$	0.47092	0.21356	8.1421e-02	2.8627e-02
rate		0.57	0.69	0.75

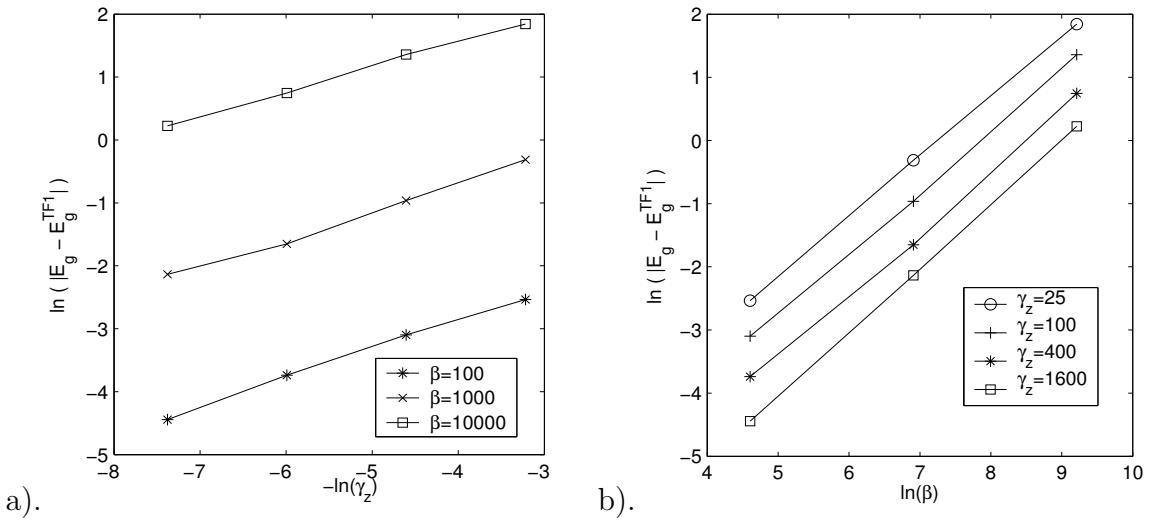

a). b).

Figure 4.6: Convergence rate of $|E_g - E_g^{TF1}|$ in 3D with a disk-shaped trap with respect to: (a) γ_z; (b) β.

Table 4.9: Error analysis of $|E_g - E_g^{TF1}|$ for the ground state in 3D with a disk-shaped trap.

$1/\gamma_z$	1/25	1/100	1/400	1/1600
$\beta_3 = 1$	0.61409	0.51950	0.41888	0.29887
rate		0.12	0.16	0.24
$\beta_3 = 10$	0.31540	0.24876	0.18610	0.10594
rate		0.17	0.21	0.41
$\beta_3 = 100$	7.9214e-02	4.5140e-02	2.3770e-02	1.1733e-02
rate		0.41	0.46	0.51
$\beta_3 = 1000$	0.73168	0.38127	0.19196	0.11818
rate		0.47	0.50	0.35
$\beta_3 = 10000$	6.3193	3.8930	2.1096	1.2518
rate		0.35	0.44	0.38

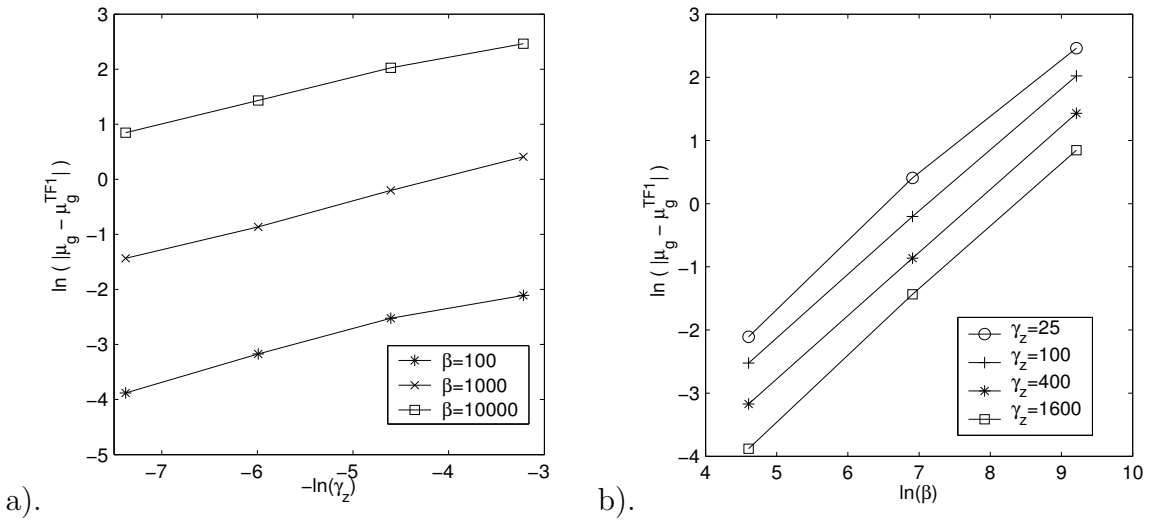

Figure 4.7: Convergence rate of $|\mu_g - \mu_g^{TF1}|$ in 3D with a disk-shaped trap with respect to: (a) γ_z; (b) β.

Table 4.10: Error analysis of $|\mu_g - \mu_g^{TF1}|$ for the ground state in 3D with a disk-shaped trap.

$1/\gamma_z$	1/25	1/100	1/400	1/1600
$\beta_3 = 1$	0.48380	0.38452	0.29107	0.18647
rate		0.17	0.20	0.32
$\beta_3 = 10$	0.20034	0.15591	0.11214	4.7083-02
rate		0.18	0.24	0.63
$\beta_3 = 100$	0.12140	8.0114e-02	4.1908e-02	2.0630e-02
rate		0.30	0.47	0.51
$\beta_3 = 1000$	1.5039	0.81591	0.42166	0.23790
rate		0.44	0.48	0.41
$\beta_3 = 10000$	11.735	7.5715	4.1839	2.3312
rate		0.32	0.43	0.42

4.3 Cigar-shaped condensation

In the case of cigar shaped condensation, i.e. $\gamma_y \gg 1$ and $\gamma_z \gg 1$ ($\Longleftrightarrow \omega_y \gg \omega_x$ and $\omega_z \gg \omega_x$), we set

$$\mu_g \approx \mu + \frac{\gamma_y + \gamma_z}{2}, \quad \phi_g(\mathbf{x}) \approx \phi(x)\phi_{23}^{\mathrm{ho}}(y,z), \quad \phi_{23}^{\mathrm{ho}}(y,z) = \frac{(\gamma_y\gamma_z)^{1/4}}{\pi^{1/2}} e^{-(\gamma_y y^2 + \gamma_z z^2)/2}. \tag{4.22}$$

Plugging (4.22) into (2.9), multiplying both sides by $\phi_{23}^{\mathrm{ho}}(y,z)$ and integrating over $(y,z) \in \mathbb{R}^2$, we get

$$\mu\ \phi(x) = -\frac{1}{2}\phi_{xx} + V_1(x)\phi + \beta_1|\phi|^2\phi, \qquad -\infty < x < \infty, \tag{4.23}$$

where $V_1(x) = \frac{x^2}{2}$ and $\beta_1 = \frac{\beta\sqrt{\gamma_y\gamma_z}}{2\pi}$. Using the results in the previous chapter for 1D GPE, again we get approximate ground state in three typical regimes:

4.3.1 Weakly interacting regime

When $\beta_1 = o(1)$, i.e. in a weakly interacting regime, the ground state is approximated by the harmonic oscillator ground state:

$$\phi_g(\mathbf{x}) \approx \phi_1^{\mathrm{ho}}(x)\phi_{23}^{\mathrm{ho}}(y,z) = \phi^{\mathrm{ho}}(x,y,z), \quad \mathbf{x} \in \mathbb{R}^3, \quad \gamma_y \gg 1 \& \gamma_z \gg 1 \tag{4.24}$$

$$E_g \approx \frac{\gamma_y + \gamma_z}{2} + \frac{1}{2} + O(\beta_1) = \frac{\gamma_y + \gamma_z}{2} + \frac{1}{2} + O\left(\beta(\gamma_y\gamma_z)^{1/2}\right), \tag{4.25}$$

$$\mu_g \approx \frac{\gamma_y + \gamma_z}{2} + \frac{1}{2} + O(\beta_1) = \frac{\gamma_y + \gamma_z}{2} + \frac{1}{2} + O\left(\beta(\gamma_y\gamma_z)^{1/2}\right). \tag{4.26}$$

4.3.2 Intermediate or strong repulsive interacting regime

When $\beta_1 = O(1)$ or $\beta_1 \gg 1$, i.e. in a intermediate or strong repulsive interacting regime, the ground state can be approximated by

$$\phi_g(\mathbf{x}) \approx \phi_g^{\mathrm{CS}}(\mathbf{x}) := \phi_g^{\mathrm{1D}}(x)\phi_{23}^{\mathrm{ho}}(y,z), \qquad \mathbf{x} \in \mathbb{R}^3, \tag{4.27}$$

$$E_g \approx E_g^{\rm CS} := E(\phi_g^{\rm 1D}(x)\phi_{23}^{\rm ho}(y,z)) = \frac{\gamma_y+\gamma_z}{2} + E_{\rm 1D}(\phi_g^{\rm 1D}) := \frac{\gamma_y+\gamma_z}{2} + E_g^{\rm 1D}, \quad (4.28)$$

$$\mu_g \approx \mu_g^{\rm CS} := \mu(\phi_g^{\rm 1D}(x)\phi_{23}^{\rm ho}(y,z)) = \frac{\gamma_y+\gamma_z}{2} + \mu_{\rm 1D}(\phi_g^{\rm 1D}) := \frac{\gamma_y+\gamma_z}{2} + \mu_g^{\rm 1D}, \quad (4.29)$$

where

$$E_g^{\rm 1D} = \int_{-\infty}^{\infty} \left[\frac{1}{2}\left|\frac{d\phi_g^{\rm 1D}(x)}{dx}\right|^2 + V_1(x)|\phi_g^{\rm 1D}(x)|^2 + \frac{\beta_1}{2}|\phi_g^{\rm 1D}(x)|^4 \right] dx,$$

$$\mu_g^{\rm 1D} = \int_{-\infty}^{\infty} \left[\frac{1}{2}\left|\frac{d\phi_g^{\rm 1D}(x)}{dx}\right|^2 + V_1(x)|\phi_g^{\rm 1D}(x)|^2 + \beta_1|\phi_g^{\rm 1D}(x)|^4 \right] dx.$$

Here $\phi_g^{\rm 1D}$, $E_g^{\rm 1D}$ and $\mu_g^{\rm 1D}$ are the ground state, energy and chemical potential of the 1D problem (4.23). In this case, one needs only to solve a 1D problem numerically and thus computational time, memory and cost are saved significantly.

To verify (4.27), (4.28) and (4.29) numerically, we solve (3.13) for $d = 1, 3$ with BEFD discretization method we reviewed in chapter 2. The computational domain for 3D GPE is chosen as $(r, x) \in [0, R] \times [-a, a]$ in the algorithm (2.21)-(2.22). The computational domain for 1D GPE is chosen as $[-a, a]$. The choice of R and a is listed in Table 3.7 for different β and γ_r. Then we get $\phi_g(x, y, z)$ and $\phi_g^{1D}(x)$. We got $\phi_{23}^{\rm ho}(y, z)$ by (3.9). Finally we compare $\phi_g(x, y, z)$ with $\phi_g^{\rm DS}(\mathbf{x}) := \phi_g^{\rm 2D}(x, y)\phi_3^{\rm ho}(z)$.

Table 4.11 lists the error $\max|\phi_g - \phi_g^{CS}|$, Table 4.12 lists the error $||\phi_g - \phi_g^{CS}||_{L^2}$, Table 4.13 lists the error $\max|(\phi_g)^2 - (\phi_g^{CS})^2|$, Table 4.14 lists the error $||(\phi_g)^2 - (\phi_g^{CS})^2||_{L^1}$, Table 4.15 lists the error $|E_g - E_g^{CS}|$, Table 4.16 lists the error $|\mu_g - \mu_g^{CS}|$. Table 4.17 lists the error $\frac{\max|\phi_g-\phi_g^{CS}|}{\max|\phi_g|}$, Table 4.18 lists the error $\frac{||\phi_g-\phi_g^{CS}||_{L^2}}{||\phi_g||_{L^2}}$, Table 4.19 lists the error $\frac{\max|(\phi_g)^2-(\phi_g^{CS})^2|}{\max|(\phi_g)^2|}$, Table 4.20 lists the error $\frac{||(\phi_g)^2-(\phi_g^{CS})^2||_{L^1}}{||(\phi_g)^2||_{L^1}}$, Table 4.21 lists the error $\frac{|E_g-E_g^{CS}|}{E_g}$ and Table 4.22 lists the error $\frac{|\mu_g-\mu_g^{CS}|}{\mu_g}$ for different β and γ_r.

Furthermore, Figure 4.8 shows the error $||\phi_g - \phi_g^{CS}||_{L^2}$, Figure 4.9 shows the error $||(\phi_g)^2 - (\phi_g^{CS})^2||_{L^1}$, Figure 4.10 shows the error $|E_g - E_g^{CS}|$, Figure 4.11 shows the error $|\mu_g - \mu_g^{CS}|$, Figure 4.12 shows the error $\frac{\max|\phi_g-\phi_g^{CS}|}{\max|\phi_g|}$, Figure 4.13 shows the error $\frac{||\phi_g-\phi_g^{CS}||_{L^2}}{||\phi_g||_{L^2}}$, Figure 4.14 shows the error $\frac{\max|(\phi_g)^2-(\phi_g^{CS})^2|}{\max|(\phi_g)^2|}$, Figure 4.15 shows the error

$\frac{||(\phi_g)^2-(\phi_g^{CS})^2||_{L^1}}{||(\phi_g)^2||_{L^1}}$, Figure 4.16 shows the error $\frac{|E_g-E_g^{CS}|}{E_g}$ and Figure 4.17 shows the error $\frac{|\mu_g-\mu_g^{CS}|}{\mu_g}$ for different β and γ_r.

Table 4.11: Error analysis of $\max|\phi_g - \phi_g^{CS}|$ for the ground state in 3D with a cigar-shaped trap.

γ_r	12.5	25	50	100	200
$\beta_3 = 25$	0.1112	0.1275	0.1536	0.1842	0.2194
rate		0.20	0.27	0.26	0.25
$\beta_3 = 50$	0.1512	0.1862	0.2270	0.2746	0.3290
rate		0.30	0.29	0.27	0.26
$\beta_3 = 100$	0.2037	0.2531	0.3099	0.3750	0.4479
rate		0.31	0.29	0.28	0.26
$\beta_3 = 200$	0.2496	0.3087	0.3760	0.4525	0.5389
rate		0.31	0.28	0.27	0.25
$\beta_3 = 400$	0.2768	0.3408	0.4145	0.5001	0.5975
rate		0.30	0.28	0.27	0.26

Table 4.12: Error analysis of $||\phi_g - \phi_g^{CS}||_{L^2}$ for the ground state in 3D with a cigar-shaped trap.

$\frac{1}{\gamma_r}$	1/12.5	1/25	1/50	1/100	1/200
$\beta_3 = 25$	0.1512	0.1283	0.1076	0.08953	0.07398
rate		0.24	0.25	0.27	0.28
$\beta_3 = 50$	0.2232	0.1914	0.1623	0.1363	0.1136
rate		0.22	0.24	0.25	0.26
$\beta_3 = 100$	0.3150	0.2742	0.2357	0.2006	0.1692
rate		0.20	0.22	0.23	0.25
$\beta_3 = 200$	0.4228	0.3740	0.3269	0.2826	0.2418
rate		0.18	0.19	0.21	0.22
$\beta_3 = 400$	0.5389	0.4851	0.4316	0.3798	0.3309
rate		0.15	0.17	0.18	0.20

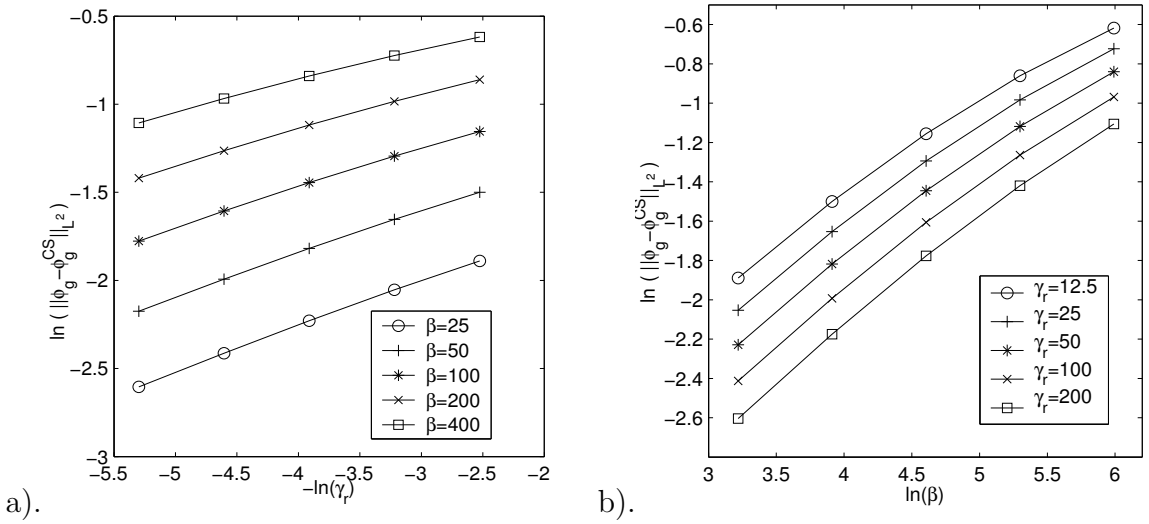

Figure 4.8: Convergence rate of $||\phi_g - \phi_g^{CS}||_{L^2}$ in 3D with a cigar-shaped trap with respect to: (a) γ_r; (b) β.

Table 4.13: Error analysis of $\max|(\phi_g)^2 - (\phi_g^{CS})^2|$ for the ground state in 3D with a cigar-shaped trap.

γ_r	12.5	25	50	100	200
$\beta_3 = 25$	0.1748	0.2346	0.3117	0.4104	0.5359
rate		0.42	0.41	0.40	0.38
$\beta_3 = 50$	0.1871	0.2573	0.3494	0.4692	0.6233
rate		0.46	0.44	0.43	0.41
$\beta_3 = 100$	0.1900	0.2684	0.3741	0.5146	0.6989
rate		0.50	0.48	0.46	0.44
$\beta_3 = 200$	0.1829	0.2653	0.3799	0.5369	0.7483
rate		0.54	0.52	0.50	0.48
$\beta_3 = 400$	0.1681	0.2493	0.3659	0.5309	0.7601
rate		0.57	0.55	0.54	0.52

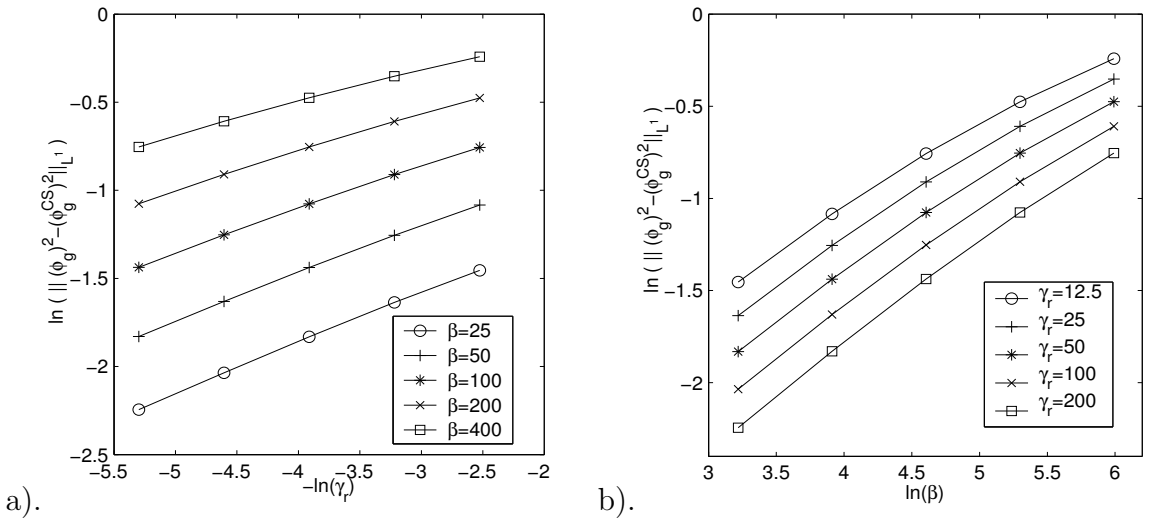

Figure 4.9: Convergence rate of $||(\phi_g)^2 - (\phi_g^{CS})^2||_{L^1}$ in 3D with a cigar-shaped trap with respect to: (a) γ_r; (b) β.

Table 4.14: Error analysis of $||(\phi_g)^2 - (\phi_g^{CS})^2||_{L^1}$ for the ground state in 3D with a cigar-shaped trap.

$\frac{1}{\gamma_r}$	1/12.5	1/25	1/50	1/100	1/200
$\beta_3 = 25$	0.2336	0.1947	0.1601	0.1306	0.1059
rate		0.26	0.28	0.29	0.30
$\beta_3 = 50$	0.3383	0.2850	0.2373	0.1958	0.1604
rate		0.25	0.26	0.28	0.29
$\beta_3 = 100$	0.4691	0.4022	0.3407	0.2857	0.2375
rate		0.22	0.24	0.25	0.27
$\beta_3 = 200$	0.6212	0.5440	0.4706	0.4026	0.3408
rate		0.19	0.21	0.23	0.24
$\beta_3 = 400$	0.7856	0.7031	0.6221	0.5441	0.4706
rate		0.16	0.18	0.19	0.21

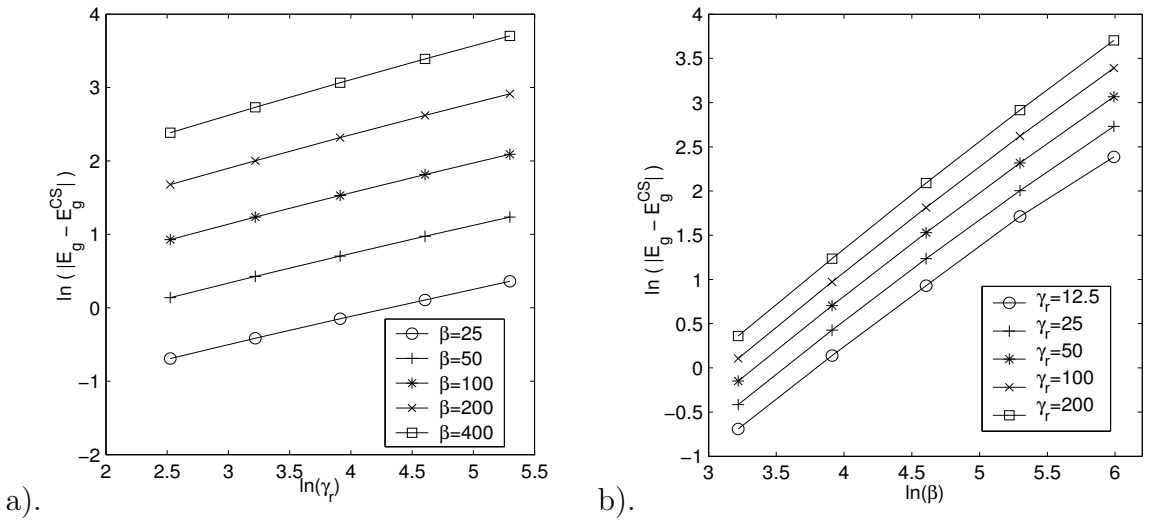

Figure 4.10: Convergence rate of $|E_g - E_g^{CS}|$ in 3D with a cigar-shaped trap with respect to: (a) γ_r; (b) β.

Table 4.15: Error analysis of $|E_g - E_g^{CS}|$ for the ground state in 3D with a cigar-shaped trap.

γ_r	12.5	25	50	100	200
$\beta_3 = 25$	0.5007	0.6600	0.8612	1.112	1.433
rate		0.40	0.38	0.37	0.37
$\beta_3 = 50$	1.148	1.532	2.022	2.646	3.441
rate		0.42	0.40	0.39	0.38
$\beta_3 = 100$	2.533	3.437	4.614	6.132	8.086
rate		0.44	0.42	0.41	0.40
$\beta_3 = 200$	5.358	7.415	10.15	13.75	18.45
rate		0.47	0.45	0.44	0.42
$\beta_3 = 400$	10.86	15.35	21.45	29.66	40.60
rate		0.50	0.48	0.47	0.45

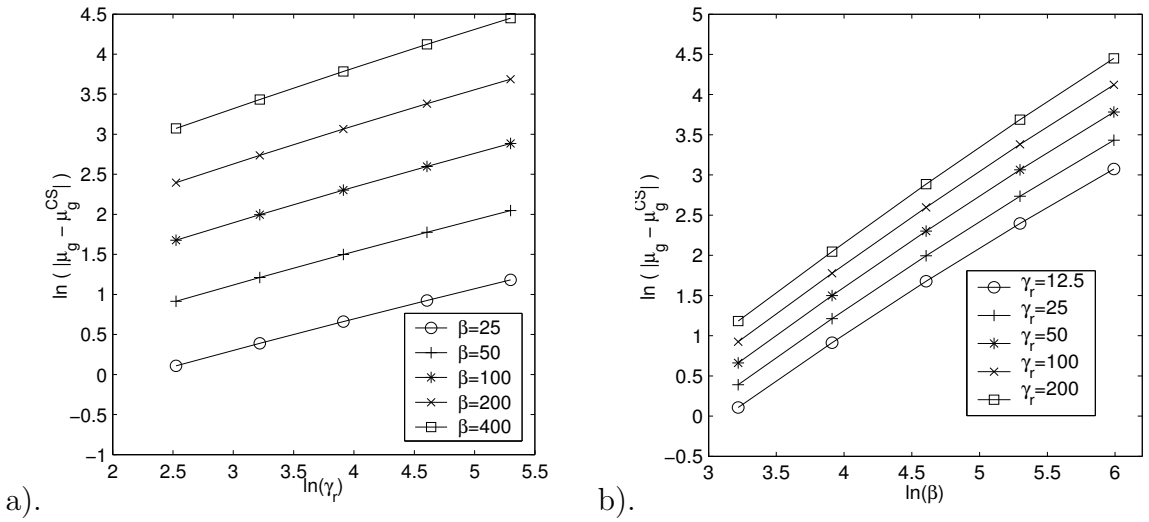

Figure 4.11: Convergence rate of $|\mu_g - \mu_g^{CS}|$ in 3D with a cigar-shaped trap with respect to: (a) γ_r; (b) β.

Table 4.16: Error analysis of $|\mu_g - \mu_g^{CS}|$ for the ground state in 3D with a cigar-shaped trap.

γ_r	12.5	25	50	100	200
$\beta_3 = 25$	1.114	1.476	1.937	2.520	3.262
rate		0.41	0.39	0.38	0.37
$\beta_3 = 50$	2.493	3.358	4.476	5.908	7.743
rate		0.43	0.41	0.40	0.39
$\beta_3 = 100$	5.349	7.351	9.991	13.43	17.90
rate		0.46	0.44	0.43	0.41
$\beta_3 = 200$	10.98	15.42	21.42	29.40	39.95
rate		0.49	0.47	0.46	0.44
$\beta_3 = 400$	21.62	30.98	43.95	61.69	85.65
rate		0.52	0.50	0.49	0.47

Table 4.17: Error analysis of $\frac{\max|\phi_g-\phi_g^{CS}|}{\max|\phi_g|}$ for the ground state in 3D with a cigar-shaped trap.

$\frac{1}{\gamma_r}$	1/12.5	1/25	1/50	1/100	1/200
$\beta_3 = 25$	0.1522	0.1351	0.1265	0.1183	0.1102
rate		0.17	0.09	0.10	0.10
$\beta_3 = 50$	0.2467	0.2335	0.2197	0.2057	0.1916
rate		0.08	0.09	0.10	0.10
$\beta_3 = 100$	0.4022	0.3815	0.3576	0.3325	0.3064
rate		0.08	0.09	0.11	0.12
$\beta_3 = 200$	0.6028	0.5663	0.5250	0.4822	0.4397
rate		0.09	0.11	0.12	0.13
$\beta_3 = 400$	0.8230	0.7674	0.7080	0.6486	0.5898
rate		0.10	0.12	0.13	0.14

From Tables 4.11-4.22 and Figures 4.8-4.17, when $\beta \geq 0$, $\gamma \geq 1$ and $\beta\gamma^{-1} = o(1)$, we can draw the following conclusion:

$$\|\phi_g^2 - (\phi_g^{\mathrm{CS}})^2\|_{L^1} = O\left(\frac{\beta^{1/3}\ \ln\gamma_r}{\gamma_r^{1/3}}\right), \qquad \|\phi_g - \phi_g^{\mathrm{CS}}(x)\|_{L^2} = O\left(\frac{\beta^{1/3}\ \ln\gamma_r}{\gamma_r^{1/3}}\right),$$

$$|E_g - E_g^{\mathrm{CS}}| = O\left(\beta\ \gamma_r^{1/3}\ln\gamma_r\right), \qquad \frac{|E_g - E_g^{\mathrm{CS}}|}{E_g} = O\left(\frac{\beta^{1/3}\ \ln\gamma_r}{\gamma_r^{2/3}}\right),$$

$$|\mu_g - \mu_g^{\mathrm{CS}}| = O\left(\beta\ \gamma_r^{1/3}\ln\gamma_r\right), \qquad \frac{|\mu_g - \mu_g^{\mathrm{CS}}|}{\mu_g} = O\left(\frac{\beta^{1/3}\ \ln\gamma_r}{\gamma_r^{2/3}}\right).$$

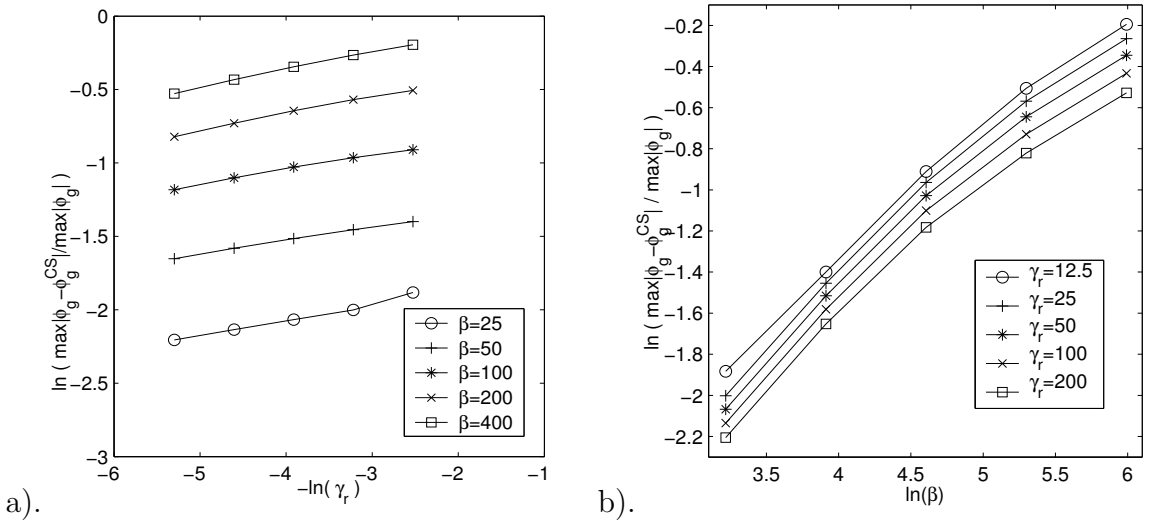

Figure 4.12: Convergence rate of $\frac{\max|\phi_g - \phi_g^{CS}|}{\max|\phi_g|}$ in 3D with a cigar-shaped trap with respect to: (a) γ_r; (b) β.

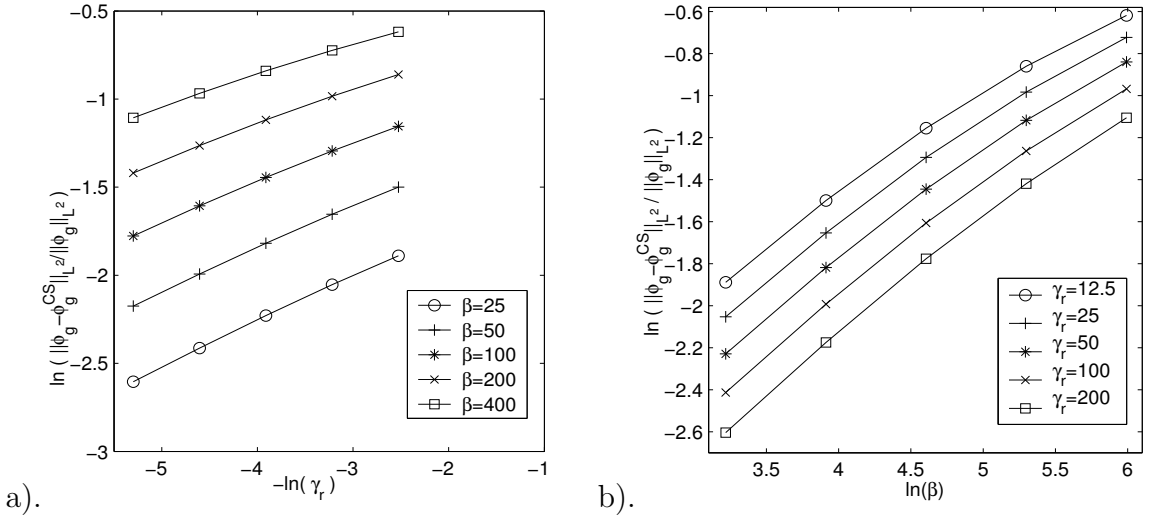

Figure 4.13: Convergence rate of $\frac{||\phi_g - \phi_g^{CS}||_{L^2}}{||\phi_g||_{L^2}}$ in 3D with a cigar-shaped trap with respect to: (a) γ_r; (b) β.

Table 4.18: Error analysis of $\frac{||\phi_g - \phi_g^{CS}||_{L^2}}{||\phi_g||_{L^2}}$ for the ground state in 3D with a cigar-shaped trap.

$\frac{1}{\gamma_r}$	1/12.5	1/25	1/50	1/100	1/200
$\beta_3 = 25$	0.1512	0.1283	0.1076	0.08953	0.07398
rate		0.24	0.25	0.27	0.28
$\beta_3 = 50$	0.2232	0.1914	0.1623	0.1363	0.1136
rate		0.22	0.24	0.25	0.26
$\beta_3 = 100$	0.3150	0.2742	0.2357	0.2006	0.1692
rate		0.20	0.22	0.23	0.25
$\beta_3 = 200$	0.4228	0.3740	0.3269	0.2826	0.2418
rate		0.18	0.19	0.21	0.22
$\beta_3 = 400$	0.5389	0.4851	0.4316	0.3798	0.3309
rate		0.15	0.17	0.18	0.20

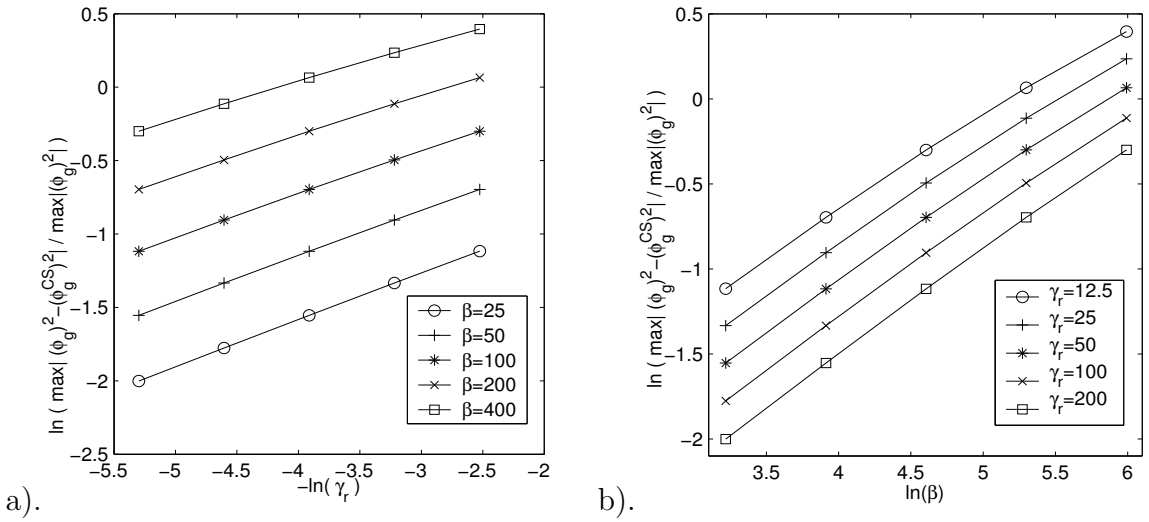

Figure 4.14: Convergence rate of $\frac{\max|(\phi_g)^2 - (\phi_g^{CS})^2|}{\max|(\phi_g)^2|}$ in 3D with a cigar-shaped trap with respect to: (a) γ_r; (b) β.

Table 4.19: Error analysis of $\frac{\max|(\phi_g)^2-(\phi_g^{CS})^2|}{\max|(\phi_g)^2|}$ for the ground state in 3D with a cigar-shaped trap.

$\frac{1}{\gamma_r}$	1/12.5	1/25	1/50	1/100	1/200
$\beta_3 = 25$	0.3275	0.2635	0.2114	0.1692	0.1352
rate		0.31	0.32	0.32	0.32
$\beta_3 = 50$	0.4982	0.4047	0.3271	0.2634	0.2114
rate		0.30	0.31	0.31	0.32
$\beta_3 = 100$	0.7404	0.6095	0.4981	0.4047	0.3271
rate		0.28	0.29	0.30	0.31
$\beta_3 = 200$	1.067	0.8928	0.7406	0.6096	0.4982
rate		0.26	0.27	0.28	0.29
$\beta_3 = 400$	1.485	1.265	1.067	0.8930	0.7407
rate		0.23	0.24	0.26	0.27

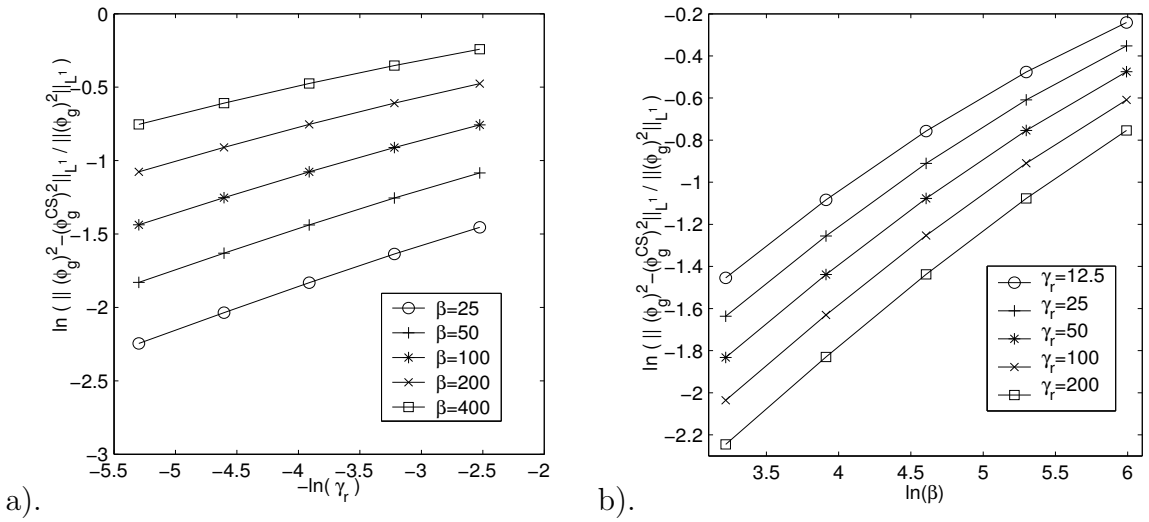

a). b).

Figure 4.15: Convergence rate of $\frac{||(\phi_g)^2-(\phi_g^{CS})^2||_{L^1}}{||\phi_g^2||_{L^1}}$ in 3D with a cigar-shaped trap with respect to: (a) γ_r; (b) β.

Table 4.20: Error analysis of $\frac{||(\phi_g)^2-(\phi_g^{CS})^2||_{L^1}}{||(\phi_g)^2||_{L^1}}$ for the ground state in 3D with a cigar-shaped trap.

$\frac{1}{\gamma_r}$	1/12.5	1/25	1/50	1/100	1/200
$\beta_3 = 25$	0.2336	0.1947	0.1601	0.1306	0.1059
rate		0.26	0.28	0.29	0.30
$\beta_3 = 50$	0.3383	0.2850	0.2373	0.1958	0.1604
rate		0.25	0.26	0.28	0.29
$\beta_3 = 100$	0.4691	0.4022	0.3407	0.2857	0.2375
rate		0.22	0.24	0.25	0.27
$\beta_3 = 200$	0.6212	0.5440	0.4706	0.4026	0.3408
rate		0.19	0.21	0.23	0.24
$\beta_3 = 400$	0.7856	0.7031	0.6221	0.5441	0.4706
rate		0.16	0.18	0.19	0.21

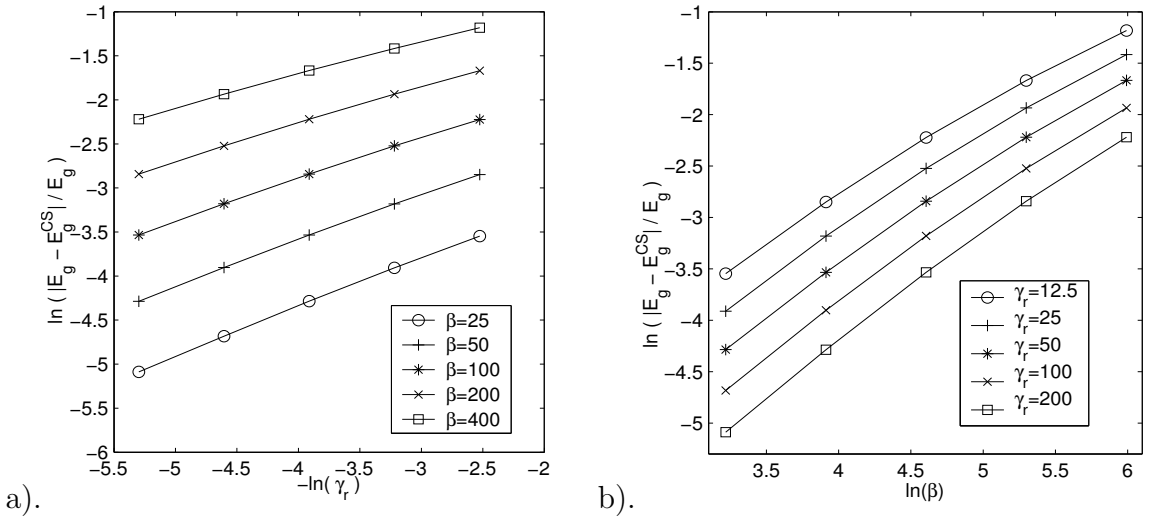

a). b).

Figure 4.16: Convergence rate of $\frac{|E_g-E_g^{CS}|}{E_g}$ in 3D with a cigar-shaped trap with respect to: (a) γ_r; (b) β.

Table 4.21: Error analysis of $\frac{|E_g - E_g^{CS}|}{E_g}$ for the ground state in 3D with a cigar-shaped trap.

$\frac{1}{\gamma_r}$	1/12.5	1/25	1/50	1/100	1/200
$\beta_3 = 25$	2.882e-02	2.011e-2	1.377e-02	9.257e-03	6.168e-03
rate		0.52	0.55	0.57	0.59
$\beta_3 = 50$	5.791e-02	4.152e-02	2.920e-02	2.018e-02	1.376e-02
rate		0.48	0.51	0.53	0.55
$\beta_3 = 100$	0.1083	8.021e-02	5.829e-02	4.158e-02	2.919e-02
rate		0.43	0.46	0.49	0.51
$\beta_3 = 200$	0.1885	0.1444	0.1086	0.08026	0.05828
rate		0.38	0.41	0.44	0.46
$\beta_3 = 400$	0.3068	0.2426	0.1888	0.1444	0.1086
rate		0.34	0.36	0.39	0.41

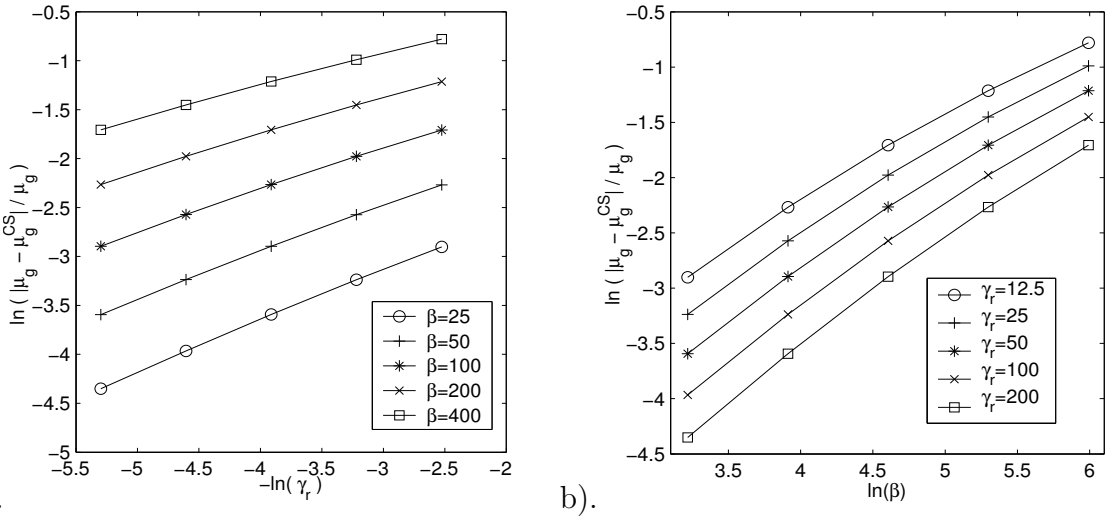

a). b).

Figure 4.17: Convergence rate of $\frac{|\mu_g - \mu_g^{CS}|}{\mu_g}$ in 3D with a cigar-shaped trap with respect to: (a) γ_r; (b) β.

Table 4.22: Error analysis of $\frac{|\mu_g - \mu_g^{CS}|}{\mu_g}$ for the ground state in 3D with a cigar-shaped trap.

$\frac{1}{\gamma_r}$	1/12.5	1/25	1/50	1/100	1/200
$\beta_3 = 25$	5.494e-02	3.925e-02	2.752e-02	1.895e-02	1.289e-02
rate		0.49	0.51	0.54	0.56
$\beta_3 = 50$	0.1035	7.634e-02	5.528e-02	3.929e-02	2.750e-02
rate		0.44	0.47	0.49	0.52
$\beta_3 = 100$	0.1814	0.1384	0.1038	0.07637	0.05525
rate		0.39	0.42	0.44	0.47
$\beta_3 = 200$	0.2971	0.2342	0.1816	0.1384	0.1037
rate		0.34	0.37	0.39	0.42
$\beta_3 = 400$	0.4584	0.3718	0.2973	0.2342	0.1816
rate		0.30	0.32	0.34	0.37

4.3.3 Strong repulsive interacting regime

When $\beta_1 \gg 1$, i.e. in a strong repulsive interacting regime, the ground state is approximated by the multiplication of the TF approximation in x-direction and the harmonic oscillator approximation in yz-plane:

$$\phi_g(\mathbf{x}) \approx \phi_g^{\mathrm{TF2}}(\mathbf{x}) := \phi_{1\mathrm{D}}^{\mathrm{TF}}(x)\phi_{23}^{\mathrm{ho}}(y,z), \qquad \mathbf{x} \in \mathbb{R}^3, \tag{4.30}$$

where

$$\phi_{1\mathrm{D}}^{\mathrm{TF}}(x) = \begin{cases} \sqrt{\left(\mu_{1\mathrm{D}}^{\mathrm{TF}} - x^2/2\right)/\beta_1^{ho}}, & x^2 < 2\mu_{1\mathrm{D}}^{\mathrm{TF}}, \\ 0 & \text{otherwise}, \end{cases} \tag{4.31}$$

$$\mu_{1\mathrm{D}}^{\mathrm{TF}} = \frac{1}{2}\left(\frac{3\beta_1^{ho}}{2}\right)^{2/3} = \frac{(3\beta)^{2/3}(\gamma_y\gamma_z)^{1/3}}{2(4\pi)^{2/3}}. \tag{4.32}$$

Plugging (4.27), (4.23), (3.30) with $d = 1$, (4.32), (3.37) with $d = 1$ and $\beta_1 = \beta_1^{ho}$ into (3.16), we get the approximate energy:

$$\begin{aligned} E_g &= E(\phi_g) = E_g(\phi_g^{1\mathrm{D}}(x)\phi_{23}^{\mathrm{ho}}(y,z)) + O\left(\beta\gamma_y^{1/3}\ln\gamma_y\right) \\ &= \frac{\gamma_y+\gamma_z}{2} + E_{1\mathrm{D}}(\phi_g^{1\mathrm{D}}) + O\left(\beta\gamma_y^{1/3}\ln\gamma_y\right) = \frac{\gamma_y+\gamma_z}{2} + E_g^{1\mathrm{D}} + O\left(\beta\gamma_y^{1/3}\ln\gamma_y\right) \\ &\approx \frac{\gamma_y+\gamma_z}{2} + \frac{3}{5}\frac{1}{2}\left(\frac{3\beta_1^{ho}}{2}\right)^{2/3} + \frac{\tilde{C}_1}{(\beta_1^{ho})^{2/3}}\left(\ln\beta_1^{ho} + G_1\right) + O\left(\beta\gamma^{1/3}\ln\gamma\right) \\ &\approx E_g^{\mathrm{TF2}} + O\left(\beta\gamma_y^{1/3}\ln\gamma_y\right), \end{aligned} \tag{4.33}$$

where

$$E_g^{\mathrm{TF2}} = \frac{\gamma_y+\gamma_z}{2} + \frac{3^{5/3}(\beta^2\gamma_y\gamma_z)^{1/3}}{10(4\pi)^{2/3}}. \tag{4.34}$$

Similarly, we get the approximate chemical potential:

$$\mu_g \approx \mu_g^{\mathrm{TF2}} + O\left(\beta\gamma_y^{1/3}\ln\gamma_y\right), \tag{4.35}$$

where

$$\mu_g^{\mathrm{TF2}} = \frac{\gamma_y+\gamma_z}{2} + \frac{3^{2/3}(\beta^2\gamma_y\gamma_z)^{1/3}}{2(4\pi)^{2/3}}. \tag{4.36}$$

If $\gamma_y = \gamma_z := \gamma_r$, then (4.32), (4.33) and (4.35) collapse to

$$E_g \approx E_g^{\mathrm{TF2}} + O\left(\beta\gamma^{1/3}\ln\gamma\right), \quad \mu_g \approx \mu_g^{\mathrm{TF2}} + O\left(\beta\gamma^{1/3}\ln\gamma\right), \tag{4.37}$$

$$\mu_{1\mathrm{D}}^{\mathrm{TF}} = \frac{(3\beta\gamma)^{2/3}}{2(4\pi)^{2/3}}, \quad E_g^{\mathrm{TF2}} = \gamma + \frac{3^{5/3}(\beta\gamma)^{2/3}}{10(4\pi)^{2/3}}, \quad \mu_g^{\mathrm{TF2}} = \gamma + \frac{3^{2/3}(\beta\gamma)^{2/3}}{2(4\pi)^{2/3}}. \tag{4.38}$$

To verify (4.30), (4.37) and (4.38) numerically, we solve (3.13) for $d = 3$ with BEFD discretization method we reviewed in chapter 2. The computational domains for 3D GPE and 1D GPE are chosen as in the previous subsections. Then we get $\phi_g(x, y, z)$. Finally we compare $\phi_g(x, y, z)$ with $\phi_g^{\mathrm{TF2}}(\mathbf{x}) := \phi_{1D}^{\mathrm{TF}}(x)\phi_{23}^{\mathrm{ho}}(y, z)$.

Table 4.23 lists the error $\max|\phi_g - \phi_g^{TF2}|$, Table 4.24 lists the error $||\phi_g - \phi_g^{TF2}||_{L^2}$, Table 4.25 lists the error $\max|(\phi_g)^2 - (\phi_g^{TF2})^2|$, Table 4.26 lists the error $||(\phi_g)^2 - (\phi_g^{TF2})^2||_{L^1}$, Table 4.27 lists the error $|E_g - E_g^{TF2}|$, Table 4.28 lists the error $|\mu_g - \mu_g^{TF2}|$. Table 4.29 lists the error $\frac{\max|\phi_g - \phi_g^{TF2}|}{\max|\phi_g|}$, Table 4.30 lists the error $\frac{||\phi_g - \phi_g^{TF2}||_{L^2}}{||\phi_g||_{L^2}}$, Table 4.31 lists the error $\frac{\max|(\phi_g)^2 - (\phi_g^{TF2})^2|}{\max|(\phi_g)^2|}$, Table 4.32 lists the error $\frac{||(\phi_g)^2 - (\phi_g^{TF2})^2||_{L^1}}{||(\phi_g)^2||_{L^1}}$, Table 4.33 lists the error $\frac{|E_g - E_g^{TF2}|}{E_g}$ and Table 4.34 lists the error $\frac{|\mu_g - \mu_g^{TF2}|}{\mu_g}$ for different β and γ_r.

Furthermore, Figure 4.18 shows the error $||\phi_g - \phi_g^{TF2}||_{L^2}$, Figure 4.19 shows the error $||(\phi_g)^2 - (\phi_g^{TF2})^2||_{L^1}$, Figure 4.20 shows the error $|E_g - E_g^{TF2}|$, Figure 4.21 shows the error $|\mu_g - \mu_g^{TF2}|$, Figure 4.22 shows the error $\frac{\max|\phi_g - \phi_g^{TF2}|}{\max|\phi_g|}$, Figure 4.23 shows the error $\frac{||\phi_g - \phi_g^{TF2}||_{L^2}}{||\phi_g||_{L^2}}$, Figure 4.24 shows the error $\frac{\max|(\phi_g)^2 - (\phi_g^{TF2})^2|}{\max|(\phi_g)^2|}$, Figure 4.25 shows the error $\frac{||(\phi_g)^2 - (\phi_g^{TF2})^2||_{L^1}}{||(\phi_g)^2||_{L^1}}$, Figure 4.26 shows the error $\frac{|E_g - E_g^{TF2}|}{E_g}$ and Figure 4.27 shows the error $\frac{|\mu_g - \mu_g^{TF2}|}{\mu_g}$ for different β and γ_r.

Table 4.23: Error analysis of $\max|\phi_g - \phi_g^{TF2}|$ for the ground state in 3D with a cigar-shaped trap.

$\frac{1}{\gamma_r}$	1/12.5	1/25	1/50	1/100	1/200
$\beta_3 = 25$	0.1226	0.1447	0.1711	0.2025	0.2390
rate		0.24	0.24	0.24	0.24
$\beta_3 = 50$	0.1633	0.1985	0.2402	0.2880	0.3426
rate		0.28	0.27	0.26	0.25
$\beta_3 = 100$	0.2110	0.2597	0.3158	0.3794	0.4516
rate		0.30	0.28	0.27	0.25
$\beta_3 = 200$	0.2517	0.3100	0.3769	0.4531	0.5393
rate		0.30	0.28	0.27	0.25
$\beta_3 = 400$	0.2772	0.3410	0.4146	0.5001	0.5975
rate		0.30	0.28	0.27	0.25

Table 4.24: Error analysis of $||\phi_g - \phi_g^{TF2}||_{L^2}$ for the ground state in 3D with a cigar-shaped trap.

$\frac{1}{\gamma_r}$	1/12.5	1/25	1/50	1/100	1/200
$\beta_3 = 25$	0.1549	0.1298	0.1079	0.08936	0.07368
rate		0.26	0.27	0.27	0.28
$\beta_3 = 50$	0.2216	0.1900	0.1612	0.1355	0.1130
rate		0.22	0.24	0.25	0.26
$\beta_3 = 100$	0.3139	0.2735	0.2353	0.2004	0.1690
rate		0.20	0.22	0.23	0.25
$\beta_3 = 200$	0.4225	0.3739	0.3268	0.2825	0.2417
rate		0.18	0.19	0.21	0.23
$\beta_3 = 400$	0.5389	0.4850	0.4316	0.3799	0.3309
rate		0.15	0.17	0.18	0.20

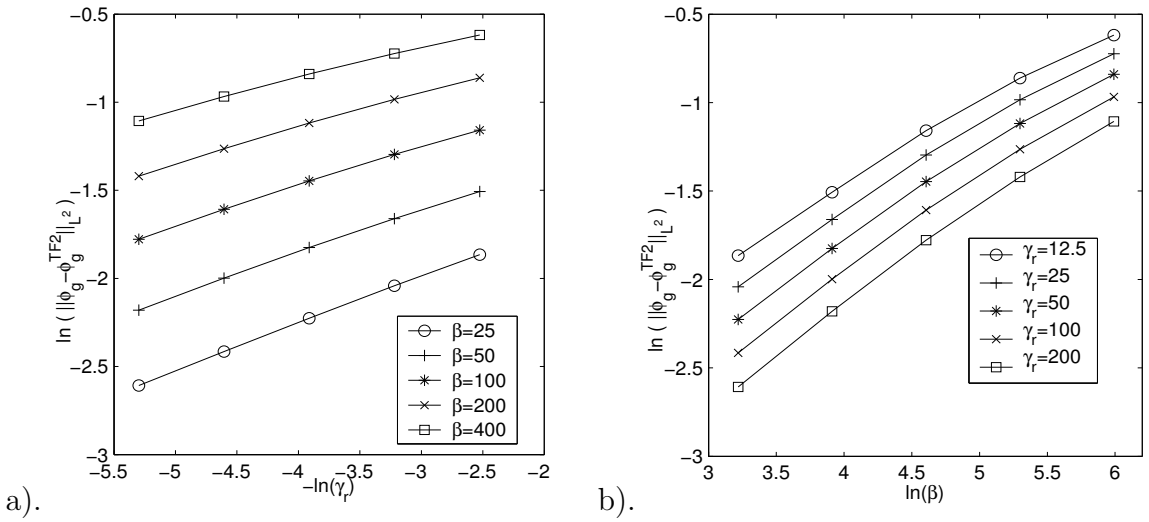

Figure 4.18: Convergence rate of $||\phi_g - \phi_g^{TF2}||_{L^2}$ in 3D with a cigar-shaped trap with respect to: (a) γ_r; (b) β.

Table 4.25: Error analysis of $\max|(\phi_g)^2 - (\phi_g^{TF2})^2|$ for the ground state in 3D with a cigar-shaped trap.

$\frac{1}{\gamma_r}$	1/12.5	1/25	1/50	1/100	1/200
$\beta_3 = 25$	0.1749	0.2346	0.3115	0.4102	0.5358
rate		0.42	0.41	0.40	0.39
$\beta_3 = 50$	0.1870	0.2572	0.3493	0.4691	0.6233
rate		0.46	0.44	0.43	0.41
$\beta_3 = 100$	0.1899	0.2684	0.3741	0.5146	0.6989
rate		0.50	0.48	0.46	0.44
$\beta_3 = 200$	0.1829	0.2653	0.3799	0.5369	0.7483
rate		0.54	0.52	0.50	0.48
$\beta_3 = 400$	0.1681	0.2493	0.3659	0.5308	0.7600
rate		0.57	0.55	0.54	0.52

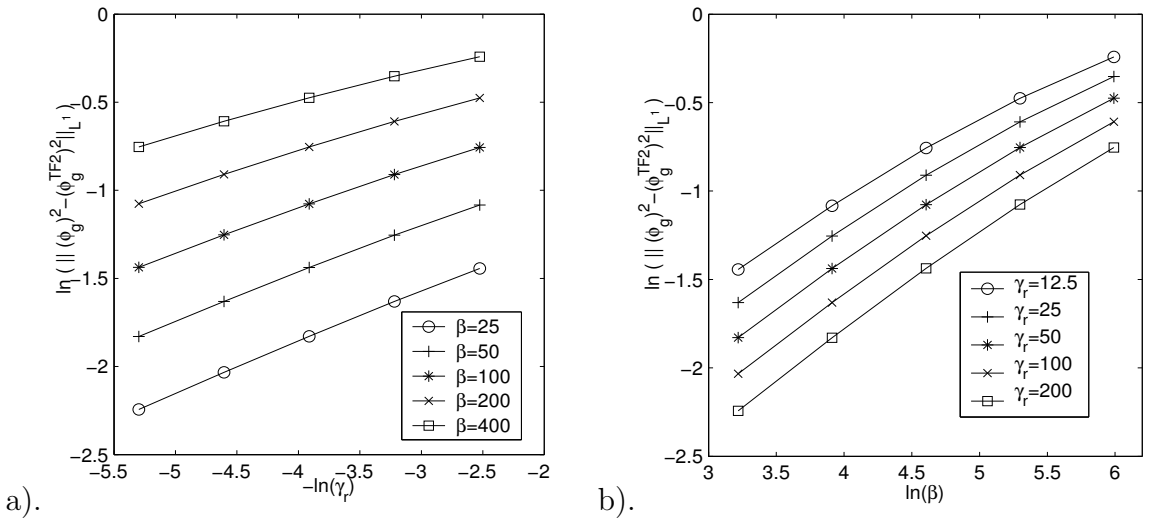

Figure 4.19: Convergence rate of $||(\phi_g)^2 - (\phi_g^{TF2})^2||_{L^1}$ in 3D with a cigar-shaped trap with respect to: (a) γ_r; (b) β.

Table 4.26: Error analysis of $||(\phi_g)^2 - (\phi_g^{TF2})^2||_{L^1}$ for the ground state in 3D with a cigar-shaped trap.

$\frac{1}{\gamma_r}$	1/12.5	1/25	1/50	1/100	1/200
$\beta_3 = 25$	0.2360	0.1958	0.1606	0.1309	0.1061
rate		0.27	0.29	0.30	0.30
$\beta_3 = 50$	0.3385	0.2851	0.2373	0.1958	0.1604
rate		0.25	0.26	0.28	0.29
$\beta_3 = 100$	0.4691	0.4022	0.3407	0.2857	0.2375
rate		0.22	0.24	0.25	0.27
$\beta_3 = 200$	0.6212	0.5440	0.4706	0.4026	0.3408
rate		0.19	0.21	0.23	0.24
$\beta_3 = 400$	0.7856	0.7031	0.6221	0.5442	0.4707
rate		0.16	0.18	0.19	0.21

a).

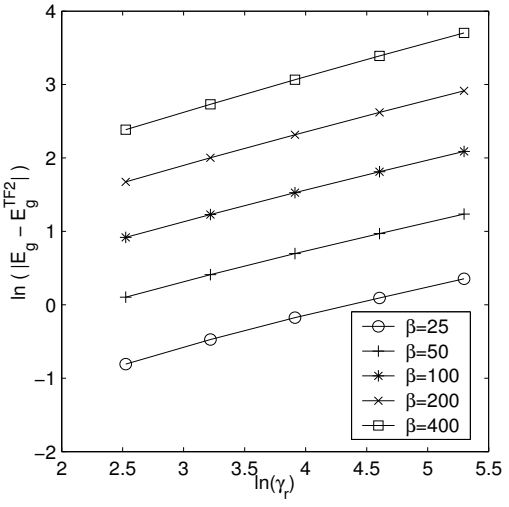

b).

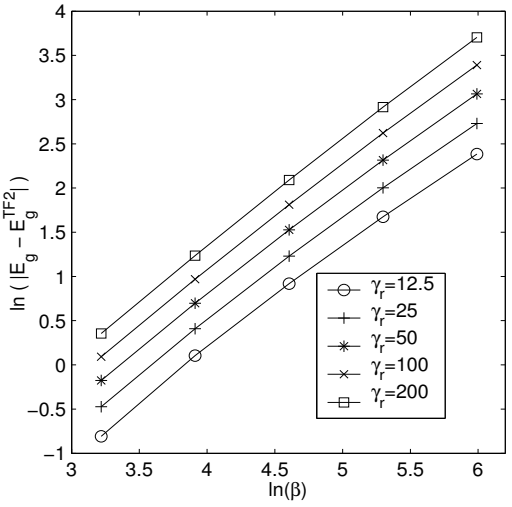

Figure 4.20: Convergence rate of $|E_g - E_g^{TF2}|$ in 3D with a cigar-shaped trap with respect to: (a) γ_r; (b) β.

Table 4.27: Error analysis of $|E_g - E_g^{TF2}|$ for the ground state in 3D with a cigar-shaped trap.

$\frac{1}{\gamma_r}$	1/12.5	1/25	1/50	1/100	1/200
$\beta_3 = 25$	0.4456	0.6229	0.8389	1.096	1.426
rate		0.48	0.43	0.39	0.38
$\beta_3 = 50$	1.110	1.506	2.008	2.635	3.438
rate		0.44	0.41	0.39	0.38
$\beta_3 = 100$	2.506	3.419	4.604	6.125	8.084
rate		0.45	0.43	0.41	0.40
$\beta_3 = 200$	5.338	7.402	10.14	13.75	18.45
rate		0.47	0.45	0.44	0.42
$\beta_3 = 400$	10.85	15.33	21.44	29.66	40.60
rate		0.50	0.48	0.47	0.45

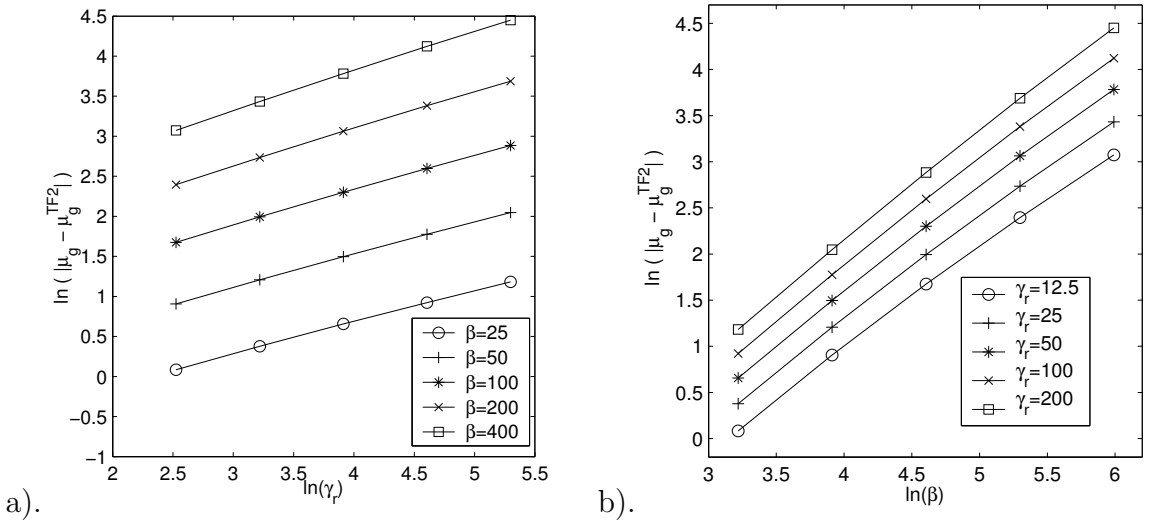

Figure 4.21: Convergence rate of $|\mu_g - \mu_g^{TF2}|$ in 3D with a cigar-shaped trap with respect to: (a) γ_r; (b) β.

Table 4.28: Error analysis of $|\mu_g - \mu_g^{TF2}|$ for the ground state in 3D with a cigar-shaped trap.

$\frac{1}{\gamma_r}$	1/12.5	1/25	1/50	1/100	1/200
$\beta_3 = 25$	1.087	1.459	1.928	2.513	3.261
rate		0.42	0.40	0.38	0.38
$\beta_3 = 50$	2.474	3.345	4.470	5.904	7.743
rate		0.44	0.42	0.40	0.39
$\beta_3 = 100$	5.335	7.342	9.985	13.43	17.89
rate		0.46	0.44	0.43	0.41
$\beta_3 = 200$	10.97	15.41	21.41	29.40	39.95
rate		0.49	0.47	0.46	0.44
$\beta_3 = 400$	21.61	30.97	43.94	61.67	85.63
rate		0.52	0.50	0.49	0.47

Table 4.29: Error analysis of $\frac{\max|\phi_g-\phi_g^{TF2}|}{\max|\phi_g|}$ for the ground state in 3D with a cigar-shaped trap.

$\frac{1}{\gamma_r}$	1/12.5	1/25	1/50	1/100	1/200
$\beta_3 = 25$	0.1678	0.1533	0.1410	0.1300	0.1200
rate		0.13	0.12	0.12	0.12
$\beta_3 = 50$	0.2665	0.2490	0.2324	0.2158	0.1995
rate		0.10	0.10	0.11	0.11
$\beta_3 = 100$	0.4166	0.3914	0.3644	0.3365	0.3090
rate		0.09	0.10	0.11	0.12
$\beta_3 = 200$	0.6080	0.5687	0.5262	0.4828	0.4400
rate		0.10	0.11	0.12	0.13
$\beta_3 = 400$	0.8239	0.7679	0.7082	0.6487	0.5898
rate		0.10	0.12	0.13	0.14

From Tables 4.23-4.34 and figures 4.18-4.27 , when $\beta \geq 0$, $\gamma \geq 1$ and $\beta\gamma^{-1} = o(1)$, we can draw the following conclusion:

$$\|\phi_g - \phi_g^{\mathrm{TF2}}\|_{L^2} = O\left(\frac{\beta^{1/3}\,\ln\gamma}{\gamma^{1/3}}\right), \quad \|(\phi_g)^2 - (\phi_g^{\mathrm{TF2}})^2\|_{L^1} = O\left(\frac{\beta^{1/3}\,\ln\gamma}{\gamma^{1/3}}\right),$$

$$|E_g - E_g^{\mathrm{TF2}}| = O\left(\beta\,\gamma^{1/3}\ln\gamma\right), \qquad \frac{|E_g - E_g^{\mathrm{TF2}}|}{E_g} = O\left(\frac{\beta^{1/3}\,\ln\gamma}{\gamma^{2/3}}\right),$$

$$|\mu_g - \mu_g^{\mathrm{TF2}}| = O\left(\beta\,\gamma^{1/3}\ln\gamma\right), \qquad \frac{|\mu_g - \mu_g^{\mathrm{TF2}}|}{\mu_g} = O\left(\frac{\beta^{1/3}\,\ln\gamma}{\gamma^{2/3}}\right).$$

These results confirm the asymptotic results (4.37), (4.38), (4.33) and (4.35). Furthermore, our numerical results indicate that $(\phi_g^{\mathrm{TF2}}(\mathbf{x}))^2$ doesn't converges pointwisely to the ground state $(\phi_g(\mathbf{x}))^2$ when $\gamma_z \to \infty$ and $\beta > 0$.

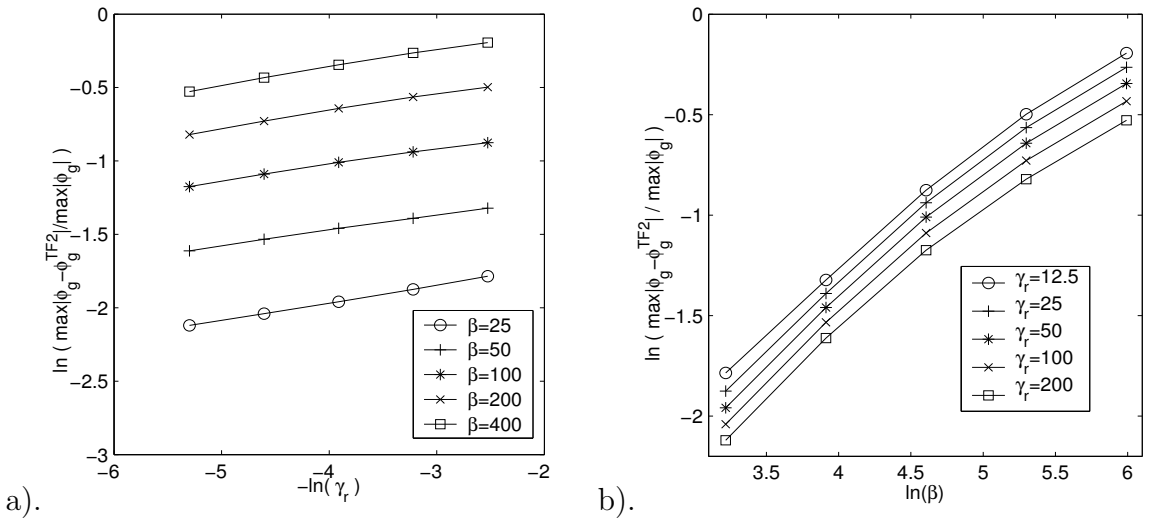

a). b).

Figure 4.22: Convergence rate of $\frac{\max|\phi_g - \phi_g^{TF2}|}{\max|\phi_g|}$ in 3D with a cigar-shaped trap with respect to: (a) γ_r; (b) β.

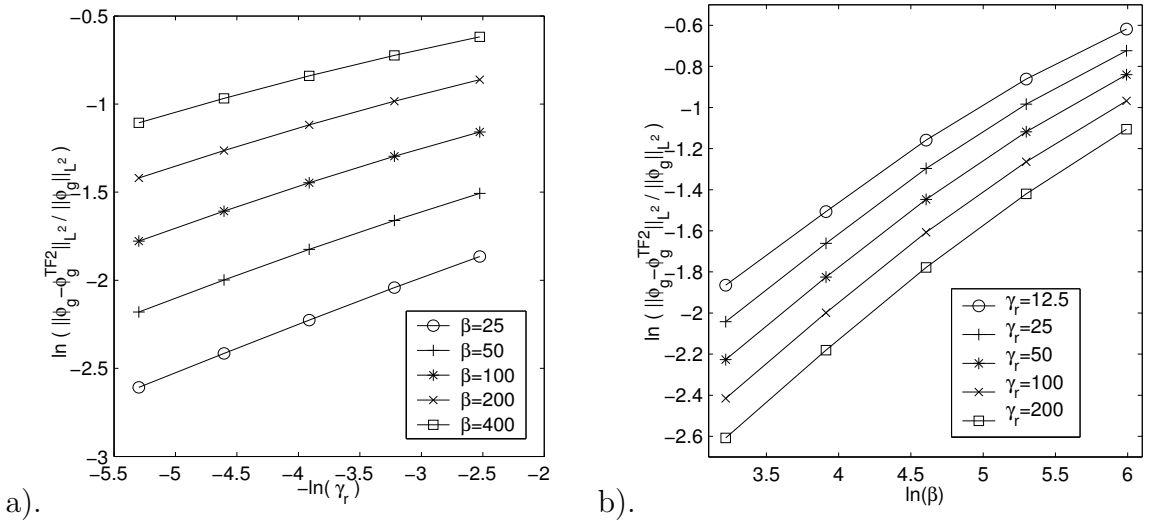

a). b).

Figure 4.23: Convergence rate of $\frac{||\phi_g - \phi_g^{TF2}||_{L^2}}{||\phi_g||_{L^2}}$ in 3D with a cigar-shaped trap with respect to: (a) γ_r; (b) β.

Table 4.30: Error analysis of $\frac{||\phi_g - \phi_g^{TF2}||_{L^2}}{||\phi_g||_{L^2}}$ for the ground state in 3D with a cigar-shaped trap.

$\frac{1}{\gamma_r}$	1/12.5	1/25	1/50	1/100	1/200
$\beta_3 = 25$	0.1549	0.1298	0.1079	0.08936	0.07368
rate		0.26	0.27	0.27	0.28
$\beta_3 = 50$	0.2216	0.1900	0.1612	0.1355	0.1130
rate		0.22	0.24	0.25	0.26
$\beta_3 = 100$	0.3139	0.2735	0.2353	0.2004	0.1690
rate		0.20	0.22	0.23	0.25
$\beta_3 = 200$	0.4225	0.3739	0.3268	0.2825	0.2417
rate		0.18	0.19	0.21	0.23
$\beta_3 = 400$	0.5389	0.4850	0.4316	0.3799	0.3309
rate		0.15	0.17	0.18	0.20

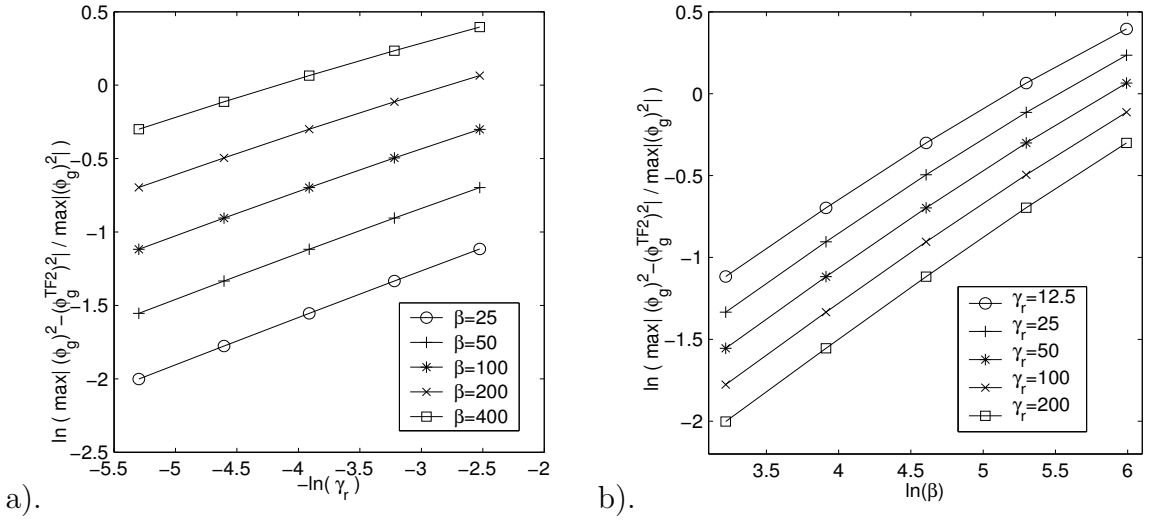

Figure 4.24: Convergence rate of $\frac{\max|(\phi_g)^2 - (\phi_g^{TF2})^2|}{\max|(\phi_g)^2|}$ in 3D with a cigar-shaped trap with respect to: (a) γ_r; (b) β.

Table 4.31: Error analysis of $\frac{\max|(\phi_g)^2-(\phi_g^{TF2})^2|}{\max|(\phi_g)^2|}$ for the ground state in 3D with a cigar-shaped trap.

$\frac{1}{\gamma_r}$	1/12.5	1/25	1/50	1/100	1/200
$\beta_3 = 25$	0.3276	0.2634	0.2113	0.1692	0.1351
rate		0.31	0.32	0.32	0.33
$\beta_3 = 50$	0.4981	0.4046	0.3271	0.2634	0.2113
rate		0.30	0.31	0.31	0.32
$\beta_3 = 100$	0.7403	0.6094	0.4981	0.4047	0.3271
rate		0.28	0.29	0.30	0.31
$\beta_3 = 200$	1.067	0.8927	0.7405	0.6096	0.4982
rate		0.26	0.27	0.28	0.29
$\beta_3 = 400$	1.485	1.265	1.067	0.8929	0.7406
rate		0.23	0.24	0.26	0.27

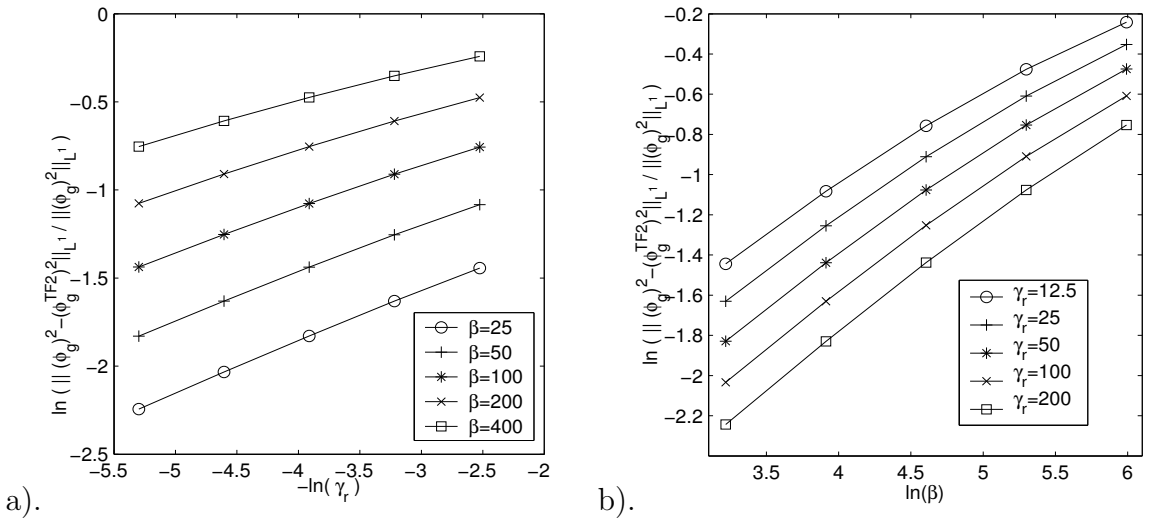

Figure 4.25: Convergence rate of $\frac{||(\phi_g)^2-(\phi_g^{TF2})^2||_{L^1}}{||(\phi_g)^2||_{L^1}}$ in 3D with a cigar-shaped trap with respect to: (a) γ_r; (b) β.

Table 4.32: Error analysis of $\frac{||(\phi_g)^2-(\phi_g^{TF2})^2||_{L^1}}{||(\phi_g)^2||_{L^1}}$ for the ground state in 3D with a cigar-shaped trap.

$\frac{1}{\gamma_r}$	1/12.5	1/25	1/50	1/100	1/200
$\beta_3 = 25$	0.2360	0.1958	0.1606	0.1309	0.1061
rate		0.27	0.29	0.30	0.30
$\beta_3 = 50$	0.3385	0.2851	0.2373	0.1958	0.1604
rate		0.25	0.26	0.28	0.29
$\beta_3 = 100$	0.4691	0.4022	0.3407	0.2857	0.2375
rate		0.22	0.24	0.25	0.27
$\beta_3 = 200$	0.6212	0.5440	0.4706	0.4026	0.3408
rate		0.19	0.21	0.23	0.24
$\beta_3 = 400$	0.7856	0.7031	0.6221	0.5442	0.4707
rate		0.16	0.18	0.19	0.21

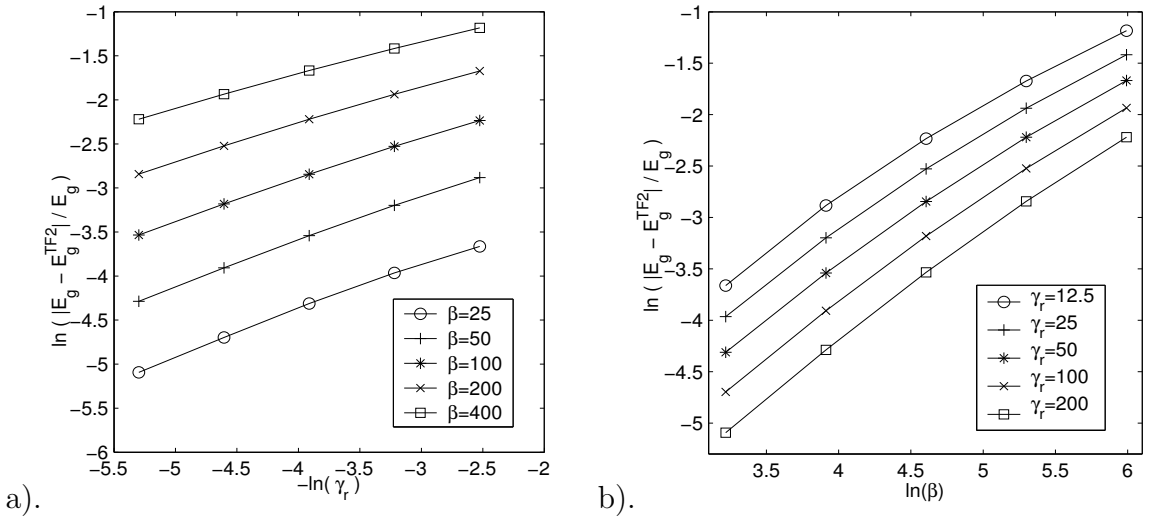

a). b).

Figure 4.26: Convergence rate of $\frac{|E_g-E_g^{TF2}|}{E_g}$ in 3D with a cigar-shaped trap with respect to: (a) γ_r; (b) β.

Table 4.33: Error analysis of $\frac{|E_g - E_g^{TF2}|}{E_g}$ for the ground state in 3D with a cigar-shaped trap.

$\frac{1}{\gamma_r}$	1/12.5	1/25	1/50	1/100	1/200
$\beta_3 = 25$	2.565e-02	1.898e-02	1.341e-02	9.122e-03	6.137e-03
rate		0.43	0.50	0.56	0.57
$\beta_3 = 50$	5.597e-02	4.083e-02	2.900e-02	2.010e-02	1.374e-02
rate		0.46	0.49	0.53	0.55
$\beta_3 = 100$	0.1071	7.980e-02	5.816e-02	4.153e-02	2.919e-02
rate		0.42	0.46	0.49	0.51
$\beta_3 = 200$	0.1878	0.1441	0.1086	0.08024	0.05827
rate		0.38	0.41	0.44	0.46
$\beta_3 = 400$	0.3063	0.2424	0.1887	0.1444	0.1086
rate		0.34	0.36	0.39	0.41

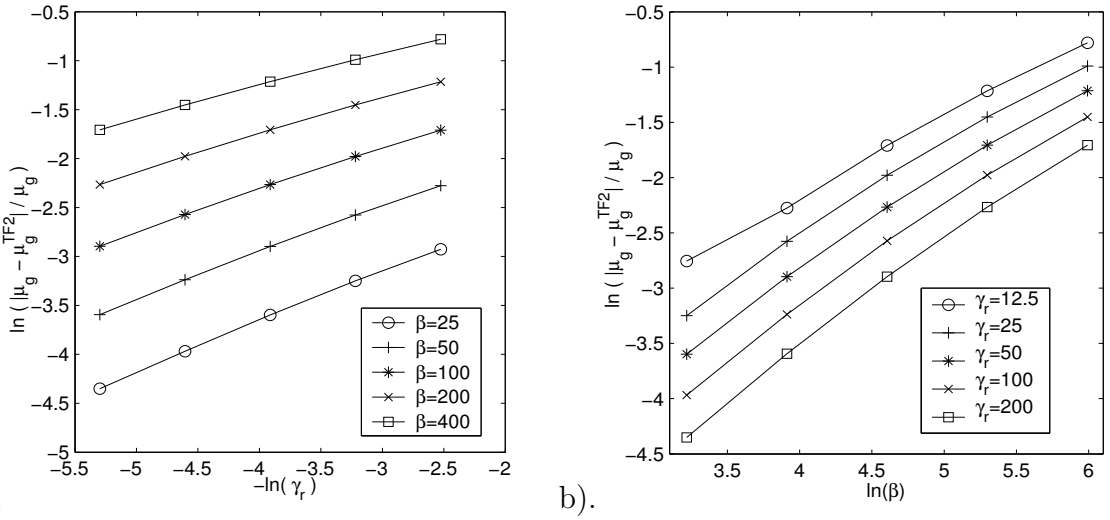

a). b).

Figure 4.27: Convergence rate of $\frac{|\mu_g - \mu_g^{TF2}|}{\mu_g}$ in 3D with a cigar-shaped trap with respect to: (a) γ_r; (b) β.

Table 4.34: Error analysis of $\frac{|\mu_g - \mu_g^{TF2}|}{\mu_g}$ for the ground state in 3D with a cigar-shaped trap.

$\frac{1}{\gamma_r}$	1/12.5	1/25	1/50	1/100	1/200
$\beta_3 = 25$	5.361e-02	3.879e-02	2.739e-02	1.891e-02	1.289e-02
rate		0.47	0.50	0.53	0.55
$\beta_3 = 50$	0.1027	7.606e-02	5.520e-02	3.926e-02	2.750e-02
rate		0.43	0.46	0.49	0.51
$\beta_3 = 100$	0.1809	0.1383	0.1037	0.07635	0.05525
rate		0.39	0.42	0.44	0.47
$\beta_3 = 200$	0.2968	0.2341	0.1816	0.1384	0.1037
rate		0.34	0.37	0.39	0.42
$\beta_3 = 400$	0.4582	0.3716	0.2972	0.2342	0.1816
rate		0.30	0.32	0.34	0.37

Chapter 5

Numerical Results for Dynamics of GPE

In this chapter, we first review the fourth-order time-splitting sine-spectral method [11] for computing dynamics of GPE. Then we use the method to study numerically dimension reduction of time dependent GPE from 3D to 2D.

5.1 Numerical method

In this section, we review the time-splitting sine spectral method, proposed in [11] for computing dynamics of GPE. For simplicity, we use 1D GPE as an example to review this method. For high dimension, the method can be extended straightforward by tensor grid. Now we consider 1D GPE with homogeneous Dirichlet boundary condition.

$$i\frac{\partial\psi}{\partial t} = -\frac{1}{2}\psi_{xx} + \frac{x^2}{2}\psi + \beta_1|\psi|^2\psi, \quad a < x < b, \quad t \geq 0, \tag{5.1}$$

$$\psi(a,t) = \psi(b,t) = 0, \qquad t \geq 0, \tag{5.2}$$

$$\psi(\mathbf{x},0) = \psi_0(\mathbf{x}), \quad a \leqslant x \leqslant b. \tag{5.3}$$

We choose the spatial mesh size $h = \triangle x > 0$ with $h = (b-a)/M$ where M is an even positive integer, the time step $k = \triangle t > 0$ and let the grid points and the time

step be

$$x_j \triangleq a + jh, \qquad t_n \triangleq nk, \qquad j = 0, 1, ..., M, \qquad n = 0, 1, 2, \cdots .$$

Let ψ_j^n be the approximation of $\psi(x_j, t_n)$ and ϕ^n be the solution vector at time $t = t_n = nk$ with components ψ_j^n.

From time $t = t_n$ to time $t = t_{n+1}$, the GPE (5.1) can be written in the form of $i\partial_t\psi = A\psi + B\psi$ with

$$A\psi = V_d(\mathbf{x})\psi(\mathbf{x}, t) + \beta_d|\psi(\mathbf{x}, t)|^2\psi(\mathbf{x}, t), \quad B\psi = -\frac{1}{2}\partial_{xx}\psi(\mathbf{x}, t). \tag{5.4}$$

Thus, the key for an efficient implementation of time-splitting is to solve efficiently the following two subproblems:

$$i\psi_t(\mathbf{x}, t) = B\psi = -\frac{1}{2}\partial_{xx}\psi(\mathbf{x}, t), \tag{5.5}$$

and

$$i\psi_t(\mathbf{x}, t) = A\psi = V_d(\mathbf{x})\psi(\mathbf{x}, t) + \beta_d|\psi(\mathbf{x}, t)|^2\psi(\mathbf{x}, t). \tag{5.6}$$

Equation (5.5) will be discretized in space by the sine-spectral method and integrated in time *exactly*. For $t \in [t_n, t_{n+1}]$, the ODE (5.6) leaves $|\psi|$ invariant in t [14, 17] and therefore becomes:

$$i\psi_t(x, t) = V(x)\psi(x, t) + \beta|\psi(x, t_n)|^2\psi(x, t), \tag{5.7}$$

and thus can be integrated *exactly*.

Fourth-order time-splitting sine-spectral method

From time $t = t_n$ to $t = t_{n+1}$, we combine the splitting steps via the fourth-order split-step method and obtain a fourth-order time-splitting sine-spectral method

(TSSP4) [36, 56, 18] for the GPE (5.1). The detailed method is given by:

$$
\begin{aligned}
\psi_j^{(1)} &= e^{-i2w_1k(V(x_j)+\beta|\psi_j^n|^2)}\psi_j^n \ , \\
\psi_j^{(2)} &= \sum_{l=1}^{M-1} e^{-iw_2k\mu_l^2}\widehat{\psi}_l^{(1)}\sin(\mu_l(x_j-a)) \ , \\
\psi_j^{(3)} &= e^{-i2w_3k(V(x_j)+\beta|\psi_j^{(2)}|^2)}\psi_j^{(2)} \ , \\
\psi_j^{(4)} &= \sum_{l=1}^{M-1} e^{-iw_4k\mu_l^2}\widehat{\psi}_l^{(3)}\sin(\mu_l(x_j-a)), \quad j=1,2,\cdots,M-1 \ , \\
\psi_j^{(5)} &= e^{-i2w_3k(V(x_j)+\beta|\psi_j^{(4)}|^2)}\psi_j^{(4)} \ , \\
\psi_j^{(6)} &= \sum_{l=1}^{M-1} e^{-iw_2k\mu_l^2}\widehat{\psi}_l^{(5)}\sin(\mu_l(x_j-a)) \ , \\
\psi_j^{n+1} &= e^{-i2w_1k(V(x_j)+\beta|\psi_j^{(6)}|^2)}\psi_j^{(6)} \ ,
\end{aligned} \tag{5.8}
$$

where

$$
w_1 = 0.33780\ 17979\ 89914\ 40851, \qquad w_2 = 0.67560\ 35959\ 79828\ 81702,
$$

$$
w_3 = -0.08780\ 17979\ 89914\ 40851, \qquad w_4 = -0.85120\ 71979\ 59657\ 63405.
$$

5.2 Numerical results for reduction of time dependent GPE

In this section, we will present some numerical results to verify the dimension reduction of time-dependent GPE for dynamics of BEC. In order to do so, for any given γ_z, let $\psi^{3D}(x,y,z,t)$ be the numerical solution of the 3D GPE (2.5) with $\gamma_x=\gamma_y=2$, $\beta=100$ and the initial data $\psi_0(x,y,z)$ in (3.14) with $d=3$ is chosen as the ground state of (2.5) with $\gamma_x=\gamma_y=1$, $\beta=100$. This 3D dynamics of BEC corresponds that initially the condensate is assumed to be in its ground state, when at $t=0$, we double the trap frequencies in x- and y-axis and keep the trap frequency in z-axis, i.e. setting $\gamma_x=\gamma_y=2$. Similarly, let $\psi^{2D}(x,y,t)$ be the numerical solution of the 2D GPE (3.5) with $\gamma_x=2$, $\gamma_y=2$, $\beta_2=\beta\sqrt{\frac{\gamma_z}{2\pi}}$ and initial data $\psi_0(x,y)$ in (3.14)

with $d = 2$ is chosen as the ground state of (3.5) with $\gamma_x = \gamma_y = 1$. In fact, ψ^{2D} is the solution of the 2D reduction problem. In order to do the comparison, we introduce

$$\phi_3(z,t) = \left(\int_{\mathbb{R}^2} \left|\psi^{\rm 3D}(x,y,z,t)\right|^2 \, dxdy\right)^{1/2} \approx \phi_3^{\rm ho}(z) = \left(\frac{\gamma_z}{\pi}\right)^{1/4} e^{-\gamma_z z^2/2}, \quad (5.9)$$

$$\phi^{\rm 3D}(\mathbf{x},t) \approx \phi^{\rm DS}(\mathbf{x},t) := \psi^{\rm 2D}(x,y,t)\phi_3^{\rm ho}(z), \qquad \mathbf{x} \in \mathbb{R}^3, \quad (5.10)$$

and the condensate widths

$$\sigma_\alpha(t) = \int_{\mathbb{R}^3} \alpha^2 \left|\psi^{\rm 3D}(\mathbf{x},t)\right|^2 d\mathbf{x}, \quad \sigma_\alpha^a(t) = \int_{\mathbb{R}^3} \alpha^2 \left|\psi^{\rm DS}(\mathbf{x},t)\right|^2 d\mathbf{x}, \qquad \alpha = x,y,z. \quad (5.11)$$

The numerical solution $\psi^{\rm 3D}$ and $\psi^{\rm 2D}$ are obtained by the fourth-order time-splitting sine-spectral method in the previous section. In my computation, we take $k = 0.001$, and choose the computation domain as $[-R_x, R_x] \times [-R_y, R_y] \times [-R_z, R_z]$ with $R_x = R_y$ for 3D GPE and $[-R_x, R_x] \times [-R_x, R_x]$ for 2D GPE. The choice of R_x and R_z is listed in Table 5.1 for different γ_z. The mesh is chosen as 128^3 for 3D GPE and 128^2 for 2D GPE.

Table 5.1: Values of R_x and R_z for different γ_z.

γ_z	8	16	32	64
$\beta = 100$	$R_x = 5.4, R_z = 2.5$	$R_x = 5.6, R_z = 1.8$	$R_x = 6.0, R_z = 1.3$	$R_x = 6.2, R_z = 0.9$

Figure 5.1 shows the errors $\|\psi_3(z,t) - \phi_3^{\rm ho}(z)\|_{L^\infty}$, $|\sigma_x - \sigma_x^a| = |\sigma_y - \sigma_y^a|$, $\sigma_z - \sigma_z^a = \sigma_z - \frac{1}{4}$, $\sigma_x - \sigma_x^a$, $\left||\psi^{\rm 3D}(\mathbf{0},t)|^2 - |\psi^{\rm DS}(\mathbf{0},t)|^2\right|$ and $\max|\phi_3 - \phi_3^{\rm ho}|(t)$ for different γ_z.

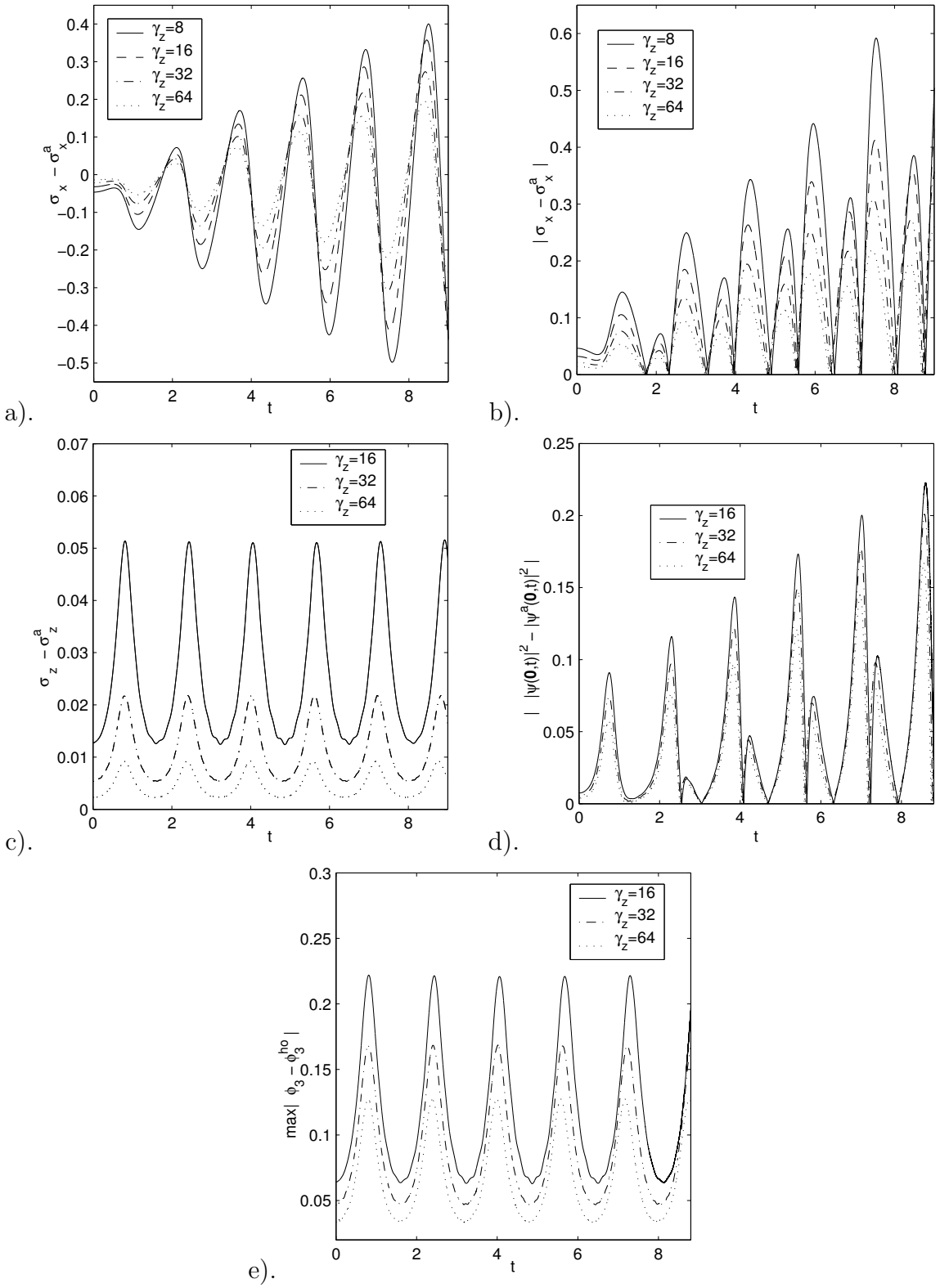

Figure 5.1: Numerical results for comparison of 3D GPE and its 2D reduction

From Figure 5.1 the dimension reduction from 3D time-dependent GPE to 2D GPE when $\gamma_z \gg 1$ is verified numerically. Furthermore, we have the following convergence rate:

$$\|\phi_3(z,t) - \phi_3^{ho}(z)\|_{L^\infty} = O\left(\frac{1}{\gamma_z^{3/4}}\right), \qquad \sigma_x(t) = \sigma_x^a(t) + O\left(\frac{1}{\gamma_z^{3/4}}\right),$$
$$\sigma_z(t) = \frac{1}{4} + O\left(\frac{1}{\gamma_z^{3/4}}\right), \qquad |\psi^e(\mathbf{x},t)|^2 = |\psi^a(\mathbf{x},t)|^2 + O\left(\frac{1}{\gamma_z^{1/2}}\right).$$

Chapter 6

Conclusion

We study numerically and asymptotically dimension reduction of 3D GPE for BEC in certain limiting trapping frequency regimes. First, we take the 3D GPE, scale it to get a three parameters model, and review how to reduce it to 2D GPE in disk-shaped condensation or 1D GPE in cigar-shaped condensation. Then we compute the ground state of 3D GPE numerically by a normalized gradient flow under backward Euler finite difference discretization [9] and verify numerically the formal dimension reduction for ground state. From our numerical results, for relative errors of the interaction parameter, we observe numerically the convergence rate of 3/4 with respect to γ_z for dimension reduction from 3D to 2D, and respectively, of 1/3 with respect to γ_r for reduction from 3D to 1D, when the ratio between trapping frequencies goes to infinity. Furthermore, we obtain Thomas-Fermi and first order approximations for energy and chemical potential of the ground state for d-dimension GPE with $d = 1, 2, 3$. Then we classify approximations of the ground state of 3D GPE in three cases based on the ratios between the trapping frequencies: i). isotropic condensation; ii). disk-shaped condensation; iii). cigar-shaped condensation. Approximate ground states as well as their energy and chemical potential are provided explicitly in weakly, intermediate repulsive and strongly repulsive interaction regimes. These results are fully confirmed by our 3D numerical results. Also, convergence rates in relative error for all interacting quantities are observed and

reported. All the computational domains in solving ground state of GPE are also shown in my thesis. Finally, we study dimension reduction of time-dependent GPE from 3D to 2D numerically by a fourth-order time-splitting sine-spectral method [11]. Our numerical results confirm the formal dimension reduction for time-dependent GPE and also suggest convergence rates in limiting trapping frequency ratios.

Bibliography

[1] J.R. Abo-Shaeer, C. Raman, J.M. Vogels and W. ketterke, *Observation of Vortex Lattices in Bose-Einstein Condensates*, Science, Vol. 292, pp. 476 (2001).

[2] S.K. Adhikari, *Collapse of attractive Bose-Einstein condensed vortex states in a cylindrical trap*, Phys. Rev. E., Vol. 65, pp. 016703 (2002).

[3] S.K. Adhikari and P. Muruganandam, *Bose-Einstein condensation dynamics from the numerical solution of the Gross-Pitaevskii equation*, J. Phys. B., Vol. 35, pp. 2831 (2002).

[4] S.K. Adhikari, *Numerical solution of the two-dimensional Gross-Pitaevskii equation fro trapped interacting atoms*, Phys. Lett. A., Vol. 265, pp. 91 (2000).

[5] S.K. Adhikari, *Numerically study of the spherically symmetric Gross-Pitaevskii equation in two space dimensions*, Phys. Rev. E., Vol. 62, pp. 2937 (2000).

[6] M.H. Anderson, J.R. Ensher, M.R. Matthews, C.E. Wieman and E.A. Cornell, *Observation of Bose-Einstein Condensation in a Dilute Atomic Vapor*, Science, Vol. 269, No. 5221, pp. 198 (1995).

[7] W. Bao and W.J. Tang, *Ground state solution of Bose-Einstein condensate by directly minimizing the energy functional*, J. Comput. Phys., Vol. 187, No. 1, pp. 230 (2003).

[8] W. Bao, D. Jaksch and P.A. Markowich, *Numerical solution of the Gross-Pitaevskii Equation for Bose-Einstein condensation*, J. Comput. Phys., Vol. 187, No. 1, pp. 318 (2003).

[9] W. Bao and Q. Du, *Computing the ground state solution of Bose-Einstein condensates by a normalized gradient flow*, SIAM J. Sci. Comput., Vol. 25, No. 5, pp. 1674 (2004).

[10] W. Bao, Y.Y. Ge, D. Jaksch and P.A. Markowich, *Convergence rate of dimension reduction in Bose-Einstein condensates*, preprint.

[11] W. Bao and Y.Z. Zhang, *Dynamics of the ground state and central vortex states in Bose-Einstein condensation*, preprint.

[12] W. Bao, *Ground states and dynamics of multi-component Bose-Einstein condensates*, SIAM Multiscale Modeling and Simulation, Vol. 2, No. 2, pp. 210 (2004).

[13] W. Bao, *Numerical methods for nonlinear Schrodinger equation with nonzero far-field conditions*, preprint.

[14] W. Bao, S. Jin and P.A. Markowich, *Numerical study of time-splitting spectral discretizations of nonlinear Schrodinger equations in the semi-classical regimes*, SIAM J. Sci. Comput., Vol. 25, No. 1, pp. 27 (2003).

[15] W. Bao and D. Jaksch, *An explicit unconditionally stable numerical method for solving damped nonlinear Schrodinger equations with a focusing nonlinearity*, SIAM J. Numer. Anal., Vol. 41, No. 4, pp. 1406 (2003).

[16] W. Bao, D. Jaksch and P.A. Markowich, *Three Dimensional Simulation of Jet Formation in Collapsing Condensates*, J. Phys. B: At. Mol. Opt. Phys., Vol. 37, No. 2, pp. 329 (2004).

[17] W. Bao, J. Shi and P.A. Markowich, *On time-splitting spectral approximation for the Schrodinger equation in the semiclassical regime*, J. Comput. Phys., Vol. 175 , pp. 487 (2002).

[18] W. Bao and J. Shen, *A Fourth-order time-splitting Laguerre-Hermite pseudo-spectral method for Bose-Einstein condensates*, SIAM J. Sci. Comput., to appear.

[19] G. Baym and C.J. Pethick, *Ground-State Properties of Magnetically Trapped Bose-Condensed Rubidium Gas*, Phys. Rev. Lett., Vol. 76, No. 1, pp. 6 (1996).

[20] S.N. Bose, Z.Phys., Vol. 26, pp. 178 (1924).

[21] C.C. Bradley, C.A. Sackett, J.J. Tollett and R.G. Hulet, *Evidence of Bose-Einstein Condensation in an Atomic Gas with Attractive Interactions*, Phys. Rev. Lett., Vol. 75, pp. 1687 (1995).

[22] M.M. Cerimele, F. Pistella and S. Succi, *Particle-inspired scheme for the Gross-Pitaevskii equation: an application to Bose-Einstein condensation*, Comput. Phys. Comm., Vol. 129, pp. 82 (2000).

[23] M.M. Cerimele, M.L. Chiofalo, F. Pistella, S. Succi and M.P. Tosi, *Numerical solution of the Gross-Pitaevskii equation using an explicit finite-difference shceme: an application to trapped Bose-Einstein condensates*, Phys. Rev. E., Vol. 62, pp. 1382 (2000).

[24] M.L. Chiofalo, S. Succi and M.P. Tosi, *Ground State of trapped interacting Bose-Einstein condensates by an explicit imaginary-time algorithm*, Phys. Rev. E., Vol. 62, pp. 7438 (2000).

[25] F. Dalfovo, L. Pitaevskii and S. Stringari, *Order parameter at the boundary of a trapped Bose gas*, Phys. Rev. A., Vol. 54, No. 5, pp. 4213 (1996).

[26] F. Dalfovo, S. Giorgini, L.P. Pitaevskii and S. Stringari, *Theory of Bose-Einstein condensation in trapped gases*, Rev. of Mod. Phys., Vol. 71, No. 3, pp. 463 (1999).

[27] K.B. Davis, M.O. Mewes, M.R. Andrews, N.J. van Druten, D.S. Durfee, D.M. Kurn and W. Ketterle, *Bose-Einstein Condensation in a Gas of Sodium Atoms*, Phys. Rev. Lett., Vol. 75, pp. 3969 (1995).

[28] R.J. Dodd, *Approximate solutions of the nonlinear Schrodinger equation for ground and excited states of Bose-Einstein condensates*, J. Res. Natl. Inst. Stan., Vol. 101, pp. 545 (1996).

[29] R. Dum, J.I. Cirac, M. Lewenstein and P. Zoller, *Creation of Dark Solitons and Vortices in Bose-Einstein Condensates*, Phys. Rev. Lett., Vol. 80, pp. 2972 (1998).

[30] V. Dunjko, V. Lorent and M. Olshanii, *Bosons in Cigar-Shaped Traps: Thomas-Fermi Regime, Tonks-Girardeau Regime, and In Between*, Phys. Rev. Lett., Vol. 86, pp. 5413 (2001).

[31] M. Edwards and K. Burnett, *Numerical solution of the nonlinear Schrodinger equation for small samples of trapped neutral atoms*, Phys. Rev. A., Vol. 51, No. 2, pp. 1382 (1995).

[32] M. Edwards, P.A. Ruprecht, K. Burnett, R.J. Dodd and C.W. Clark, *Collective Excitations of Atomic Bose-Einstein Condensates*, Phys. Rev. Lett., Vol. 77, pp. 1671 (1996).

[33] A. Einstein, Sitz. Ber. Preuss. Akad. Wiss., Vol. 22, pp. 261 (1924).

[34] J.R. Ensher, D.S. Jin, M.R. Mathews, C.E. Wieman and E.A. Cornell, *Bose-Einstein Condensation in a Dilute Gas: Measurement of Energy and Ground-State Occupation*, Phys. Rev. Lett., Vol. 77, pp. 4984 (1996).

[35] P.O. Fedichev and G.V. Shylyapnikov, *Dissipative dynamics of a vortex state in a trapped Bose-condensed gas*, Phys. Rev. A., Vol. 60, pp. R1779 (1999).

[36] B. Fornberg and T.A. Driscoll, *A fast spectral algorithm for nonlinear wave equations with linear dispersion*, J. Comput. Phys., Vol. 155, pp. 456 (1999).

[37] A. Griffin, D.W. Snoke and S. Stringari, (Eds.), Bose Einstein Condensation, Cambridge University Press, Cambridge, 1995.

[38] E.P. Gross, *Structure of a quantized vortex in boson systems*, Nuovo. Cimento., Vol. 20, pp. 454 (1961).

[39] D.A.W. Hutchinson, E. Zaremba and A. Griffin, *Finite Temperature Excitations of a Trapped Bose Gas*, Phys. Rev. Lett., Vol. 78, pp. 1842 (1997).

[40] A.D. Jackson, G.M. Kavoulakis and C.J. Pethick, *Solitary waves in clouds of Bose-Einstein condensed atoms*, Phys. Rev. A., Vol. 58, pp. 2417 (1998).

[41] D.S. Jin, J.R. Ensher, M.R. Matthews, C.E. Wieman and E.A. Coernell, *Collective Excitations of a Bose-Einstein Condensate in a Dilute Gas*, Phys. Rev. Lett., Vol. 77, pp. 420 (1996).

[42] L. Laudau and E. Lifschitz, Quantum Mechanics: Non-Relativistic Theory, Pergamon Press, New York, 1977.

[43] P. Leboeuf and N. Pavloff, *Bose-Einstein beams: coherent propagation through a guide*, Phys. Rev. A., Vol. 64, pp. 033602 (2001).

[44] E.H. Lieb, R. Seiringer and J. Yugvason, *Bosons in a trap: a rigorous derivation of the Gross-Pitaevskii energy functional*, Phys. Rev. A., Vol. 61, pp. 3602 (2000).

[45] F. London, Nature, Vol. 141, pp. 643 (1938).

[46] C.S. Lin, Numerical Methods for Computing, Beijing: Science Press, 1998.

[47] M.R. Matthews, B.P. Anderson, P.C. Haljan, D.S. Hall, C.E. Wieman and E.A. Cornell, *Vortices in a Bose-Einstein Condensate*, Phys. Rev. Lett., Vol. 83, pp. 2498 (1999).

[48] L.P. Pitaevskii, *Vortex lines in a imperfect Bose gases*, Zh. Eksp. Teor. Fiz., Vol. 40, pp. 646 (1961). (Sov. Phys. JETP., Vol. 13, pp. 451 (1961).)

[49] L.P. Pitaevskii and S. Stringari, Bose-Einstein Condensation, Clarendon press, Oxford, 2003.

[50] C. Raman, J.R. Abo-Shaeer, J.M. Vogels, K. Xu and W. Ketterle, *Vortex Nucleation in a Stirred Bose-Einstein Condensate*, Phys. Rev. Lett., Vol. 87, pp. 210402 (2001).

[51] D.S. Rokhsar, *Vortex Stability and Persistent Currents in Trapped Bose Gases*, Phys. Rev. Lett., Vol. 79, pp. 2164 (1997).

[52] P.A. Ruprecht, M.J. Holland, K. Burrett and M. Edwards, *Time-dependent solution of the nonlinear Schrodinger equation for Bose-condensed trapped neutral atoms*, Phys. Rev. A., Vol. 51, pp. 4704 (1995).

[53] B.I. Schneider and D.L. Feder, *Numerical approach to the ground and excited states of a Bose-Einstein condensated gas confined in a completely anisotropic trap*, Phys. Rev. A., Vol. 59, pp. 2232 (1999).

[54] P. Sokol, Bose Einstein Condensation, edited by A. Griffin, D.W. Snoke and S. Stringari, Cambridge University Press, Cambridge, pp. 51 (1995).

[55] J.P. Wolfe, J.L. Lin and D.W. Snoke, Bose Einstein Condensation, edited by A. Griffin, D.W. Snoke and S. Stringari, Cambridge University Press, Cambridge, pp. 281 (1995).

[56] H. Yoshida, *Construction of higher order symplectic integers*, Phys. Lett. A., Vol. 150, pp. 262 (1990).

Name: Ge Yunyi

Degree: Master of Science

Department: Computational Science

Thesis Title: Dimension Reduction of the Gross-Pitaevskii Equation for Bose-Einstein Condensates

Abstract

We study numerically and asymptotically dimension reduction of 3D GPE for BEC in certain limiting trapping frequency regimes. First, we take the 3D GPE, scale it to get a three parameters model, and review how to reduce it to 2D GPE in disk-shaped condensation or 1D GPE in cigar-shaped condensation. Then we compute the ground state of 3D GPE numerically by a normalized gradient flow under backward Euler finite difference discretization and verify numerically the formal dimension reduction for ground state. Furthermore, we obtain Thomas-Fermi and first order approximations for energy and chemical potential of the ground state for d-dimension GPE with $d = 1, 2, 3$. Then we classify approximations of the ground state of 3D GPE in three cases based on the ratios between the trapping frequencies: i). isotropic condensation; ii). disk-shaped condensation; iii). cigar-shaped condensation. These results are fully confirmed by our 3D numerical results. Also, convergence rates in relative error for all interacting quantities are observed and reported. Finally, we study dimension reduction of time-dependent GPE from 3D to 2D numerically by a fourth-order time-splitting sine-spectral method. Our numerical results confirm the formal dimension reduction for time-dependent GPE and also suggest convergence rates in limiting trapping frequency ratios.

Key words: Gross-Pitaevskii equation, Bose-Einstein condensate, Normalized gradient flow, Ground state solution, Dynamics, Dimension reduction.

DIMENSION REDUCTION OF THE GROSS-PITAEVSKII EQUATION FOR BOSE-EINSTEIN CONDENSATES

GE YUNYI

NATIONAL UNIVERSITY OF SINGAPORE

2004